REPORT DOCUMENTATION PAGE

1. REPORT DATE *(DD-MM-YYYY)*	2. REPORT TYPE	3. DATES COVERED *(From - To)*
04-30-2011	Final Report	From 9/1/2007 to 8/31/2010

4. TITLE AND SUBTITLE	5a. CONTRACT NUMBER
Novel Energetic Materials for Space Propulsion	FA9550-07-1-0582
	5b. GRANT NUMBER
	5c. PROGRAM ELEMENT NUMBER

6. AUTHOR(S)	5d. PROJECT NUMBER
Grant A. Risha, [†] Terrence L. Connell, Jr,[†] Michael Weismiller,[†] Richard A. Yetter,[†] Dilip S. Sundaram,[$] Vigor Yang,[$] Tyler D. Wood,* Mark A. Pfeil,* Timothee L. Pourpoint,* John Tsohas,* and Steven F. Son*	
	5e. TASK NUMBER
	5f. WORK UNIT NUMBER

7. PERFORMING ORGANIZATION NAME(S) AND ADDRESS(ES)	8. PERFORMING ORGANIZATION REPORT NUMBER
[†]Department of Mechanical and Nuclear Engineering The Pennsylvania State University University Park, PA 16802 *Dept. of Mechanical Engineering Purdue University, West Lafayette, IN [$]Dept. of Aerospace Engineering GIT, Atlanta, GA	

12. DISTRIBUTION / AVAILABILITY STATEMENT

Distribution A – Approved for Public Release

13. SUPPLEMENTARY NOTES

14. ABSTRACT

Frozen solid propellants based on nAl and ice mixtures have been studied. In particular, the burning rate was measured for frozen aluminum ice mixtures, a model was developed for the combustion of aluminum water mixtures, small scale motor firing tests were reported to examine chemical efficiency and performance, an internal ballistics analysis of the combusting aluminum and ice motor grain was developed using a lumped-parameter model for motor development, and the results from an initial sounding rocket launch using a non-optimized frozen aluminum-water grain were attained. In addition, various additives to the nAl and ice mixture, such as alane, ammonia borane, and hydrogen peroxide, were surveyed with initial studies to investigate overall combustion behavior and motor performance.

15. SUBJECT TERMS
Novel propellants

16. SECURITY CLASSIFICATION OF: Unclassified			17. LIMITATION OF ABSTRACT	18. NUMBER OF PAGES	19a. NAME OF RESPONSIBLE PERSON Richard A. Yetter
a. REPORT UU	**b. ABSTRACT** UU	**c. THIS PAGE** UU	UU	110	**19b. TELEPHONE NUMBER** *(include area code)* (814) 863-6375

Contents

List of Figures

5

List of Tables

Introduction

The last few decades have witnessed a tremendous increase in space-related activities and many more challenging space missions are currently being planned. So far, most space exploration and utilization activities have primarily employed chemical propulsion technology and the situation will continue in the foreseeable future. The progressively ambitious future space-mission goals have identified an acute need for novel, better performing, cost-effective, and safer ways of space exploration and utilization. Unfortunately, none of the current operational propellants have all the desired properties, and the selection of a particular propellant combination is largely a compromise based on various factors such as physical properties, ignition and combustion characteristics, cost, safety, environmental hazards, processing, material compatibility, and availability [1]. Substantial efforts are thus needed towards the development of new propellants to meet the requirements of the next generation of space exploration and utilization activities. The focus on advancing the existing propellant technologies, at this juncture, will benefit all major space programs for the Air Force, NASA, and industry. A typical space mission requires two different types of propulsion systems, viz., launch vehicle (i.e. primary and upper stages) and spacecraft (i.e. on-board) systems. The combination of solid and liquid rockets is typical of launch systems, wherein solid propellants provide a cost effective and simple way to deliver very high thrust required at lift-off, and liquid propellants fulfill the higher specific-impulse requirement of upper stages. Currently, small launches use solid propellants for the sake of economy, simplicity, and operability. The medium and heavy launches use liquid propellants in the main propulsion system, and are usually assisted by solid rocket boosters in the initial stage to meet the thrust requirements.

The propulsion system (including propellants), which is often the largest and the most massive component of a launch vehicle, provides a powerful leverage that can be gained by using high-density and better-performing propellants. The overall objective for the advancement of such systems is crucially dependent on the density and specific impulse of the propellant. Conventionally, the requirement of higher specific impulse has led to the use of cryogenic bipropellants.

Liquid oxygen (LOX) and liquid hydrogen (LH) have been most widely used for space missions [2], especially in the western world. Some of the advantages in using LOX/LH propellants are:

- low molecular weight of hydrogen which implies higher specific impulse (30% - 40% higher than other existing rocket propellants)
- non-toxic and clean combustion exhaust
- superior chamber cooling capability
- relatively stable combustion

On the other hand, the disadvantages associated with the use of LOX/LH cryogenic bipropellants are:

- low density of hydrogen which necessitates a large storage volume
- bulky tanks leading to increase in the structural mass
- safety issues linked with hydrogen and oxygen
- very low storage temperatures

• propellant compatibility with materials of storage containers

Due to low temperatures of cryogenic propellants, it is difficult to store them for long periods of time. Consequently, such propellants are less desirable for use in rockets that must be kept launch-ready for months together. The tank for storing liquid propellants is typically the highest non-expendable mass in a chemical propulsion system. Since liquid hydrogen has a very low density, the propellant volume required is many times greater than other denser fuels, thus requiring bulky and massive storage tanks. The use of high-density propellants is an excellent way to reduce the structural mass of storage tanks and associated propellant-conditioning and flow-control components. The increase in propellant density thus translates into a lower take-off weight and a larger vehicle payload capacity. Higher-energy propellant delivers better specific impulse, and consequently helps reduce the required propellant weight for a given total impulse. Such propellants can achieve the desired performance of a mission with smaller and lighter launch vehicles.

There exists a need to thoroughly identify, and investigate novel propellants in order to achieve desired combinations with higher density, higher specific impulse, and better thermal properties. Alternatives to such propellant systems as LOX/LH need to be explored in a systematic manner. Additives to hydrogen or the use of hydrocarbons may allow upper stages to deliver a better overall performance with reduced volume and cost [2]. One such fuel with desirable properties which may replace LH is liquid methane. In the past forty years, LOX/methane is the only new propellant combination that has been adopted for flight engines in the United States. Such a lack of innovation highlights the fact that the advancements in propellant technology have been found wanting for a long time. Although LOX/methane provides a reasonable propulsive performance for certain applications, more appropriate and effective propellant combinations must be continuously explored, especially in light of the encouraging advances in the field of energetic materials in the past twenty years. Ammonia borane has already been used with success to produce hydrogen for chemical lasers and fuel cells. The alternatives being considered for the oxidizer LOX are hydroxylammonium nitrate (HAN), ammonium dinitramide (ADN), hydrazinium nitroformate (HNF), and water (H_2O). Gelled propellants are being tested to determine the practicality of letting propellants freeze at low environmental temperatures and thawing them only when required for use. In addition to the above possible combinations, there is a concept to harness powerful chemical bonds between individual atoms of hydrogen, boron, carbon, and aluminum. The atoms could be arrested with a cryogenic solid, and released as they enter the rocket engine. The ongoing progress in nanotechnology can make such propellants a reality. In contrast to the situation with launch vehicles, the on-board propulsion system is usually not the most massive component of a spacecraft. The on-board systems use either mono- or bipropellants.

Among the commonly used bi-propellants are monomethylhydrazine (CH_3NHNH_2, MMH)/nitrogen tetroxide (N_2O_4, NTO) and hydrazine (N_2H_4)/NTO. Due to the toxicity of these propellants, other bi-propellants such as LOX/ethanol and H_2O_2/hydrocarbon are being explored. The catalytic-decomposed N_2H_4 has been used extensively as a monopropellant for the primary propulsion of smaller spacecrafts as well as for gas-generator applications [3]. H_2O_2 has also been used as a monopropellant in the past. With a goal to develop monopropellants with significantly better performance and no hazardous properties, efforts have been focused on aqueous solution of

HAN. The HAN-based monopropellants have higher densities and lower freezing points than the state-of-the-art hydrazine. Furthermore they pose no vapor hazard, and do not require any extraordinary storage, handling, or disposal procedures. For very small and micro spacecrafts, several alternative propulsion technologies can provide performance and system benefits. Examples include (a) a warm gas (mixture of hydrogen, oxygen, and an inert gas) propulsion system that offers a high specific impulse as compared to the conventional cold-gas systems, (b) exothermic decomposition of solid and hybrid systems, which offer the high density and simplicity of solid propellants for low-thrust, and quick-response applications, and (c) bipropellant systems using microelectronic mechanical system (MEMS) fabrication technology. In the past, the stringent system design requirements and the reluctance to change them have obviated the use and application of promising high-energetic materials. But it has become increasingly clear that to meet the needs of future space-propulsion activities, a stage has been reached wherein novel and well-characterized HDEMs may dictate the overall propulsion system design.

In this program, we have studied frozen propellants based on nAl and ice. In particular, the burning rate was measured for frozen aluminum ice mixtures, a model was developed for the combustion of aluminum water mixtures, small scale motor firing tests were reported to examine chemical efficiency and performance, an internal ballistics analysis of the combusting ALICE motor grain was developed using a lumped-parameter model for motor development, and the results from an initial sounding rocket launch using a non-optimized frozen aluminum-water grain were reported. In addition, various additives to the nAl and ice mixture, such as alane, ammonia borane, and hydrogen peroxide, were surveyed with initial studies to investigate overall combustion behavior and motor performance. The detailed results are discussed in the subsequent sections of the report.

Nano Aluminum-Ice (ALICE) based Propellants

Aluminum-water combustion has been studied since the 1960s [4-7,9,10] as a viable propellant for propulsion since the Al-H_2O reaction liberates a large amount of energy during combustion as well as green exhaust products [8,11,18-20]. Currently, propellants used for Earth to orbit and orbit-to-orbit missions are expensive. Thus, there is a need for new-generation propellants which can be used in the booster stage as well as possess characteristics which make them storable in Low Earth Orbit (LEO). Storable propellants in LEO will also be required for lengthy periods of time, which imposes greater constraints on cryogenic hydrogen. Inexpensive Al-H2O propellant systems for space exploration have been the subject of scientists and researchers for several years. The simplicity of Al-H_2O propellants makes them favorable as in-situ propellants for lunar and Mars missions. Retaining the combustion product on board may also be considered if reduction methods are available to regenerate the aluminum fuel during the mission. The idea of designing inexpensive propulsion systems to launch payloads into LEO allows for relaxed requirements for launch such as lower success rates. Aluminum and liquid water research studies have slowly transitioned into aluminum and other fuels combusting with refrigerated or "frozen" oxidizers [12,21].

Lo et al. examined frozen hydrogen peroxide with polyethylene (PE) or hydroxyl-terminated polybutadiene (HTPB) solid propellants for solid rocket booster or lower stages [14]. The composition is referred to as Cryogenic Solid Propellants (CSP). It has been postulated that these "green" propellants could be employed as early as 2010. They studied the burning behavior of CSPs in a 1-kg sandwich (disk stack) configuration in a pressurized environment [15]. Fuel modules were adjacent to H_2O_2 modules and a hydrogen/air diffusion flame was passed over the propellant surface for ignition. Spacing between the fuel modules was also varied. Burning rates as a function of pressure for the different CSP formulations were obtained yielding a pressure exponent of 0.155 to 0.165. This low pressure exponent is desirable for rocket applications. Adirim et al. successfully hot-fired several solid propellant rockets using CSP disk stacks [16,17]. The CSP composition was solid hydrogen peroxide (SH_2O_2) and PE. During the test run, the pressure reached approximately 9 MPa after a few seconds beyond ignition.

Based upon the idea of CSP composed of polymers reacting with SH_2O_2, Franson et al. replaced a portion or all of the polymeric fuel with metals and metal hydrides [22,23]. Franson et al. refer to these propellants as Refrigerated Solid Propellants (RSP). They performed two types of tests on various RSP formulations. In total, five RSP compositions were examined where the water content ranged from 60 to 70% of the mixture. All formulations used aluminum as the fuel component. In some cases, nanometer aluminum (nAl) replaced some of the micron-sized particles. Some formulations consisted only of water as the oxidizer or a combination of water and hydrogen peroxide. The first experiment was a closed bomb configuration to examine the effect of pressure on burning rate. The RSP material was placed in a 1-cm diameter glass pipe and ignited at the top with a hot wire. The second experiment was a center-perforated motor firing. A conventional cylindrical Bates motor was employed. The grain geometry was 80-mm outer diameter, 60-mm inner diameter, and 157-mm in length. The nozzle was designed to have a target pressure of 2-3 MPa. The grain was ignited using a common composite propellant (HTPB/Al/AP). The igniter was designed to burn for a total of 4 seconds. It was found that ignition might not always be homogenous. The grain ignited and burned producing a measured pressure of 2 MPa. It was estimated that approximately 13% residue remained in the chamber after the test run, indicating that 17% of the initial aluminum in the RSP possibly did not burn, and, consequently, a lower pressure was achieved than targeted. Experimental thrust and specific impulse were not reported. However, Franson et al. claim that the expected specific impulse for the current RSPs is between 355 and 375 seconds.

Recent advances in high-energy reactive nano-sized particles have enabled their use as major ingredients in propellants with enhanced properties and performance [24]. In the current investigation, the performance and viability of nAl and ice (ALICE), and various ALICE based propellant formulations were examined. Safety tests such as ESD, mechanical tensile tests, and impact tests have been performed [25]. Both fundamental steady-state strand-burner experiments and applied lab-scale hot-fire motor experiments were employed to ascertain ballistic data. Constant volume combustion experiments were conducted to obtain conversion efficiency. Linear and mass burning rates, combustion efficiency, slag accumulation, effect of motor size, thrust, and pressure were among the experimental data obtained. The effect of motor scaling regarding heat

loss, slag accumulation, and thrust is also examined. Finally, the results from the nAl and ice propellants are compared with those from conventional AP/HTPB/Al composite propellants. In addition to the potential practical applications of nAl and ice based propellants for hydrogen generation and thrust, the baseline nAl – ice system provides a simple two-component composite mixture rich in fundamental combustion science [26]. The thermodynamics of the aluminum water reaction show the flame temperature to be lower than the vaporization temperature of the aluminum. This is in contrast to aluminum combustion in air where the flame temperature is higher than the vaporization temperature of aluminum. Thus in air or oxygen, aluminum will vaporize much like a hydrocarbon fuel droplet and will burn in the vapor phase. This type of combustion can then be controlled typically by mixing rates in the gas. However, when the flame temperature is below the vaporization temperature, the combustion occurs by a heterogeneous reaction at the particle surface (like combustion of a carbon particle). This type of process is either kinetically controlled at the fuel-oxidizer interface or diffusion controlled in the condensed-phase by molecular mixing (i.e., bulk turbulent mixing in the gas has little effect), and consequently if the particles are large the combustion time is long. Thus, small (nano) particles are essential. Because of their smaller dimensions, nano particle based-systems have higher efficiency and can be operated with smaller volume combustors. Also, because of their shorter burning times, nano-particle systems can be combusted easily in overall lean mixtures.

As a consequence of the reaction being dominated by surface processes, very little gas-phase chemistry is expected. In particular, chain branching reactions should not exist in the gas-phase. Furthermore, since the aluminum oxide is formed on the nanoparticle surface, all the heat releasing reactions occur at the particle surface or within the particle and are controlled through the heterogeneous/condensed-phase reactions. This is in contrast to other AP and nitramine based propellants in current usage where most of the heat release occurs through gas-phase reactions and significant chain branching can occur. The chain branching process is very sensitive to temperature and pressure and can significantly impact the combustion behavior as evident in breaks in pressure exponents of burning rates, instability mechanisms of burning propellants in motors, and flame spread mechanisms across propellant grain surfaces. Research on the aluminum water systems allows for the study of a relatively simple system where water reacts at the particle surface of aluminum, forms aluminum oxide, and then hydrogen is desorbed. Since the water reactant may be considered a final product of any species desorbed from the surface of the aluminum particle, no heat releasing gas-phase reactions occur.

Experiments with this system and chemical mechanism should have significant impact on our understanding of what parameters determine pressure exponents, what factors determine flame spread rates into cracks, and what type of instabilities can occur in a reaction system where the mechanisms of heat feedback are significantly different. The simplicity of the system may also enable the development of correlations between initial aluminum particle size and final alumina particle size. For example, it is suspected that the usage of nAl will yield only small sized alumina in the product gas-flow in contrast to the bimodal alumina size distributions commonly found when micron sized aluminum is used in propellants.

Experimental Approach

Several different experimental facilities were used in this investigation to characterize the combustion and propulsion behavior of ALICE, composite solid propellants, and various nAl/ice based formulations. Each test facility offered unique ballistic information for the family of propellants. Specifically, the first experiment was a high-pressure optical strand burner, used to determine the influence of pressure on the propellant burning rate. The results of the strand tests served as guidance for the design, construction, and testing of lab-scale motors having various grain sizes and configurations. Using the various motor chambers, performance quantities such as thrust and total impulse as a function of propellant formulation and grain size were investigated. Constant volume combustion efficiency experiments were also conducted specifically for aluminum/ice compositions.

Baseline Reactants and Materials Characterization

The baseline propellant reactants consisted of nanometer aluminum and de-ionized water only. The aluminum particles were obtained from Nanotechnologies, Inc. and had a nominal diameter of 80-nm. From our previous studies with this material, particle densities, measured using a pycnometer inclusive of the oxide coating, had values near 3 g/cm^3 (compared to bulk Al of 2.7 g/cm^3) [27]. The active aluminum content of the "as received" nanometer aluminum was generally around 77-79%. The de-ionized water was purchased from Electron Microscopy Sciences (Reagent A.C.S. Cat#22800-01). The specifications of the deionized water were a maximum of 0.01 ppm silicate (as SiO_2), a maximum of 0.01 ppm heavy metal (as Pb), and 10 ppm of residue after removal from the packaging container in evaporation.

For the "as received" nAl, it was observed that when the nAl (immediately removed from the shipping container) was mixed with the deionized water, a low temperature slow oxidation reaction occurred where upon ammonia evolved from the aluminum surface. It was suspected that some nitrogen was bound to the particle surface of the nAl, which was displaced by oxygen after being exposed to the water, resulting in ammonia formation. To minimize this low temperature oxidation during mixing and eliminate the generation of ammonia, the nAl was further aged in ambient air for extended periods of time. The process involved placing the nAl in a large surface area aluminum sheet pan, which was placed on a vibration and stirrer plate, and exposed to air at ambient conditions for a specified period of time. Thermogravimetric analysis (TGA) and differential scanning calorimetry (DSC) analyses were performed with a Netzsch STA449F1 TGA/DSC on the "as received" and further passivated nAl. Figure 1 shows some of the TGA/DSC results for the "as received" nAl and further oxidized material.
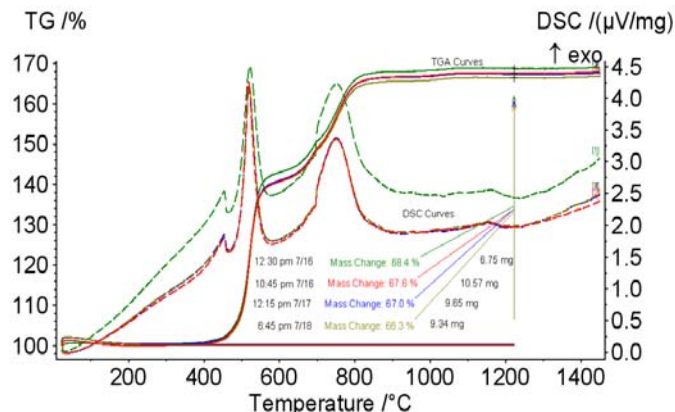
Figure 1: TGA and DSC of 80-nm aluminum with and without additional passivation. The experiment is an example of the "as received" material.

As can be seen from the results, the mass gain and thermal behavior are similar for all the samples. As observed previously in the literature, low temperature exotherms exist below the melting temperature of the aluminum (660.32 °C) prior to higher temperature oxidation processes. The TGA curves show that the material with extended passivation has less active aluminum as indicated by the slightly smaller mass weight gain after all the aluminum has been oxidized. Figure 2 shows the dependence of the active aluminum content on the extended passivation time. The active aluminum content represents the pure aluminum contained in the particle. Transmission electron microscopy (TEM) images of the "as received" and further passivated particles are shown in Figure 3. The oxide layer is clearly visible; however, noticeable differences in the thickness are difficult to determine with the limited samples and magnifications. As can be seen from the images, the particles are generally spherical and the thickness of the oxide layer is nearly uniform.

To analyze the surface composition of nAl particles, Malchi [28] reported X-ray Photoelectron Spectroscopy (XPS) studies on two samples of nAl: 38-nm Al from Technanogy and the 80-nm Al used in this study from Nanotechnologies. A low resolution survey scan was acquired from each specimen to identify the elements present. The relative concentration, chemical states of these elements and organic and alumina oxide overlayer thickness were determined from high resolution scans acquired for O 1s, N 1s, C 1s, and Al 2p photoelectrons. The average sampling depth under these conditions was 40Å (λAl2p). The results of the elemental analysis are summarized in Table 1.
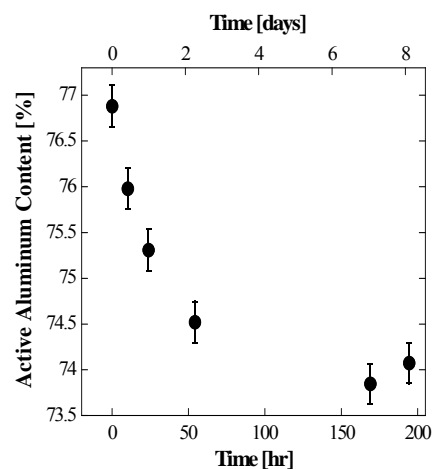
Figure 2: Active aluminum content as a function of time for extended air passivation of 80-nm aluminum.
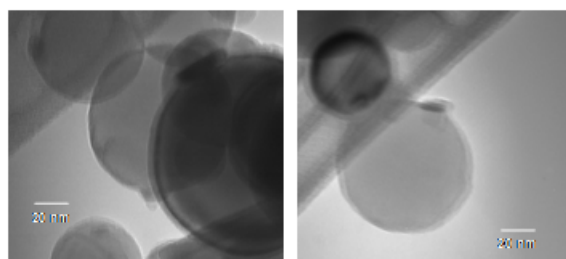
Figure 3: TEM photographs of 80-nm Al without (left) and with (right) additional passivation.

Table 1: Relative concentration of elements on powder surface (atom %) using X-ray photoelectron spectroscopy

Sample	Al	O	C	N	Si
38 nm	37.2	50.5	11.7	0.2	0.4
80 nm	34.6	42.0	21.4	1.2	0.8

From Malchi, J.Y., 2007 [28]

The species observed on all samples included: carbon species: C-C, C-O, and COOR, amine, SiO_2, Al_2O_3 and Al metal. The presence of the nitrogen (in the form of amines) is observed to be greater on the 80-nm Al than on the 38-nm Al, which is consistent with the XPS studies of Sippel [26]. An Energy Dispersive Spectroscopy (EDS) analysis was performed on the "as received" 80-nm Al and nAl that was passivated for 60 hours (**Table 2**). Four different points were analyzed (views) for the "as received" sample whereas three points were analyzed for the nAl with extended passivation. As evident from the table and in agreement with the XPS studies, nitrogen is observed in the samples. However, its presence has disappeared in the extended passivation aluminum sample.

16

Table 2: EDS analysis of 80-nm Al with and without additional air passivation.

Element	As received 80-nm Al (weight %)				Additional air passivation of 80-nm Al (weight %)		
	View 1*	View 2	View 2a	View 3	View 1	View 2	View 3
N	0.11	0.23	0.43	0.42	0	0	0
O	0.12	0.11	0	0.4	0	0	0.39
Al	99.77	99.66	99.57	99.18	100	100	99.61
	As received 80-nm Al (atom %)				Additional air passivation of 80-nm Al (atom %)		
	View 1	View 2	View 2a	View 3	View 1	View 2	View 3
N	0.21	0.43	0.82	0.8	0	0	0
O	0.21	0.28	0	0.67	0	0	0.67
Al	99.6	99.37	99.18	98.53	100	100	99.34

*The different views represent different points of analysis across the powder sample.

Surface areas of the "as received" and passivated 80-nm Al particles were performed by Brunauer Emmett Teller (BET), Micromeritics Gemini series. The results are summarized in Table 3 showing the surface area to decrease with extended passivation. A decrease in surface area would also suggest a decrease in reactivity, consistent with an increase oxide layer thickness and lower active aluminum content of the extended passivated aluminum.

Table 3: Specific surface areas of 80-nm Al with and without extended passivation.

	As received	120 hr	> 200 hr
Specific Surface Area [m²/g]	26.6	23.7	22.8

*The areas reported by the manufacturer were ~ 26.1 m²/g

In the present experiments, a minimum of 48 hour extended passivation was used for all nAl and ice mixtures. Once passivated, the aluminum was re-packaged in argon to eliminate any further particle degradation before use.

Propellant Mixing and Sample Preparation

For all experiments, with the exception of a several repeat experiments (described below), propellant mixing was performed by hand. A hand mix consists of manually mixing the aluminum and water on a glass substrate while agitating the ingredients with a flat mixing spatula. During the mixing process, force is applied to mixture with the spatula to apply shear. Depending on the material batch, the final consistency ranged from "clay-like" to "solder-like." Based upon experimental evidence, whether the initial propellant consistency prior to freezing and testing was clay-like or solder-like, the performance of the propellant was not significantly affected.

The two most important characteristics for mixing of ALICE propellants were to allow the material to properly passivate and to apply high shear force during mixing. For the material presented, these times were varied between 48 and 120 hours. The equivalence ratio, Φ, for most of the mixtures studied was 0.71 and the active aluminum content (for mixing purposes) was measured to be 74.5%. From stoichiometry, the amount of required oxidizer was determined. For each batch, the aluminum (weighed and placed on the plate first) and water were combined on a plate and hand mixed until homogenized. Because of the clay-like or solder-like consistency, manual packing into molds was required. After packing the tube molds, the material was placed in an explosion proof freezer and stored at -35°C. Densities (1.44 ± 0.03 g/cm^3) of the propellants in the filled tube molds were obtained before and after freezing by measuring the fill volume and the propellant mass. It should also be noted that once the material is frozen, no low temperature reactions have been observed. In fact, experiments have been performed on propellant samples that have been frozen for several months and no degradation in the performance has been observed.

A number of experiments were conducted with a machine-mix using the Resodyn LabRAM® mixer to verify mixing techniques. The Resodyn LabRAM® mixes all phases, sizes, or ingredients without the use of any type of impeller. The mixing container is accelerated up to 100 Gs at a frequency of approximately 60 Hz. This process applies a uniform shear force through the mixture without delivering a significant amount of heat to the ingredients. The mixer has the capability of batch sizes of up to 500 grams and can operate under vacuum if one chooses. Using the LabRAM mixer reduces the overall mixing time 10-fold.

For baseline comparisons of the ALICE propellants, two composite propellants were examined consisting primarily of ammonium perchlorate (oxidizer) and hydroxyl-terminated polybutadiene (binder/fuel). The specific compositions are listed in Table 4. Ingredients were procured from Firefox Enterprises and the aluminum was 20 μm obtained from Sigma-Aldridch. Both the aluminized and non-aluminized composite propellants were mixed using conventional mixing methods. The binder/fuel, plasticizer, and bonding agents were combined initially with the catalyst and hand mixed to homogeneity. The oxidizer was slowly introduced into the solution, hand mixing between additions, to prevent air dispersion and maintain homogeneity until the polymer – solids mix became too viscous. At this point, the mixture was agitated by a mechanical mixer at a low speed to finish combining the oxidizer. Subsequent to all ingredients (except the

curing agent) being added to the mixture, the blend was mixed in three 15 minute intervals, scraping the mixing bowl walls between each interval and periodically during mixing. These prolonged mixing cycles aided in reducing heat generation, and minimized air being whisked into and trapped by the mixture. Once the polymer mix was thoroughly mixed, the curing agent was introduced, and a 10 minute post-mix cycle completed the mixing process of the composite propellant.

Table 4: Formulations of the baseline non-aluminized and aluminized composite propellants.

Ingredient Type	Ingredient Name	Non-Aluminized Formulation [wt%] (solids loading 75.25%)	Aluminized Formulation [wt%] (solids loading 82.03%)
Oxidizer	Ammonium Perchlorate [200 μm]	74.00	70.89
Binder/Fuel	R45-M Resin (HTPB)	14.00	10.13
Metal Fuel	Aluminum [20 μm]	0.00	10.13
Plasticizer	2-Ethylhexyl Acrylate (EHA)	6.50	5.06
Catalyst	Ferric Oxide (Fe_2O_3)	1.25	1.01
Bonding Agent	HX-878 (Tepanol)	0.75	0.76
Curing Agent	Isonate 143-L (MDI)	3.50	2.03

Prior to grain casting, the propellant was placed into a vacuum oven at ambient conditions for 15 minutes to undergo degassing to remove entrapped gas. Once the curing agent was added, the working time was controlled by the amount of the curing agent and temperature of the mix. Small deviations in the amount of curative could have drastic effects on the curing time and propellant crosslinking. The consistency of the non-aluminized propellant was pourable and could be flowed under vibration into prepared molds. The simultaneous vibration and pouring process minimized air entrapment during the packing process. The grains were then cured at 50°C for 24 to 36 hours. The fully cured propellant was firm (not tacky or sticky), yet yielded under slight pressure (neither hard nor brittle). The aluminized propellant mixing process was similar to the non-aluminized composite, with the aluminum being introduced to the mix prior to the AP oxidizer. To assist the binding and coating process of the aluminum particles within the mix and prevent any hazardous reaction with the AP oxidizer during mixing, the Al particles were precoated with a thin layer of turpentine before being added to the mix. Due to the higher solids loading, the aluminized composite propellant was more viscous than the non-aluminized polymer and typically required

manual packing into the molds rather than pour filling. The densities of the non-aluminized and aluminized composite propellants were 1.55 ± 0.03 g/cm^3 and 1.65 ± 0.05 g/cm^3, respectively.

Constant Volume Propellant Strand-Burner Experimentation

Steady-state, constant-volume strand burner experiments were performed to study the combustion mechanism and to evaluate potential ALICE candidates prior to testing in the static-fire motor experiments. The chamber, constructed from 316 stainless steel, is equipped with four optical viewing ports each having a 15.2 x 2.54 cm field of view and feedthroughs in the baseplate allowing both electrical signal and gas pathways into the chamber. The 61-cm long chamber has an inner diameter of 22 cm and a total free volume of 23 L to minimize the pressure variation caused by the generation of gaseous combustion products during an experiment. One of the optical viewing ports was backlit through an optical diffuser while the opposite viewing port from the diffuser was used for real-time recording of the burning process by a Sony digital video camera. The operating pressure was varied from 0.8 to 15 MPa. The initial propellant temperature for the composite propellants was 25 °C and the ALICE samples were approximately -12 to -15 °C. Argon was used as the pressurant gas and a Setra 206 pressure transducer was used to measure the instantaneous chamber pressure. Ignition was achieved by igniting a classical double-base propellant (NOSOL 363), by a resistance wire, thereby ignition the ALICE strand. A more detailed description of the experiment can be found in Ref. [10].

Three types of baseline solid propellants were studied: (1) aluminum-ice (ALICE); (2) non-aluminized composite (AP/HTPB); and (3) aluminized composite (AP/HTPB/Al). Each was characterized as a function of pressure culminating in the classical Saint Robert's law correlation. The sample was ignited at a specific pressure, and the steady-state linear burning rate was recorded. Distance versus time curves were constructed from the recorded video and the burning rate for that specific pressure was obtained from the slope of the curves. The aluminum water mixtures were packed in 8 mm quartz tubes prior to freezing. These samples were tested frozen in the quartz tubes. The composite propellants were also packed into the same 8 mm quartz tubes and cured.

Solid Propellant Motors

A series of three lab-scale motors with combustion chamber diameters of 1.91, 3.82, and 7.62-cm (0.75, 1.5, and 3-in) were fabricated to evaluate the performance and scaling characteristics of ALICE propellants. The motors could be operated in both end-grain and center-perforated grain configurations. Nominally in each configuration and motor diameter, a post-combustion chamber with a length of 7.62 cm was used. This subsequently left room for propellant grain lengths up to 25 cm. For center-perforated motors, the grain length was kept constant at 7.62 cm while for end-burning grain motors, 3.82, 7.62 and 15.24-cm lengths were studied. A schematic diagram (center-perforated configuration) and a photograph of three different scale motors are given in Figure 4. The motor chambers are equipped with two Setra pressure transducers to monitor the pressure near both ends of the chamber. A custom-made rupture assembly with a 1.27-cm through port was installed to prevent any overpressurization. Each motor chamber was

hydrostatically pressure tested 1.5 times the working pressures. Specifically, the 7.62-cm motor was tested to 58.7 MPa (8,515 psia) to enable the possibility of higher combustion pressures if warranted.
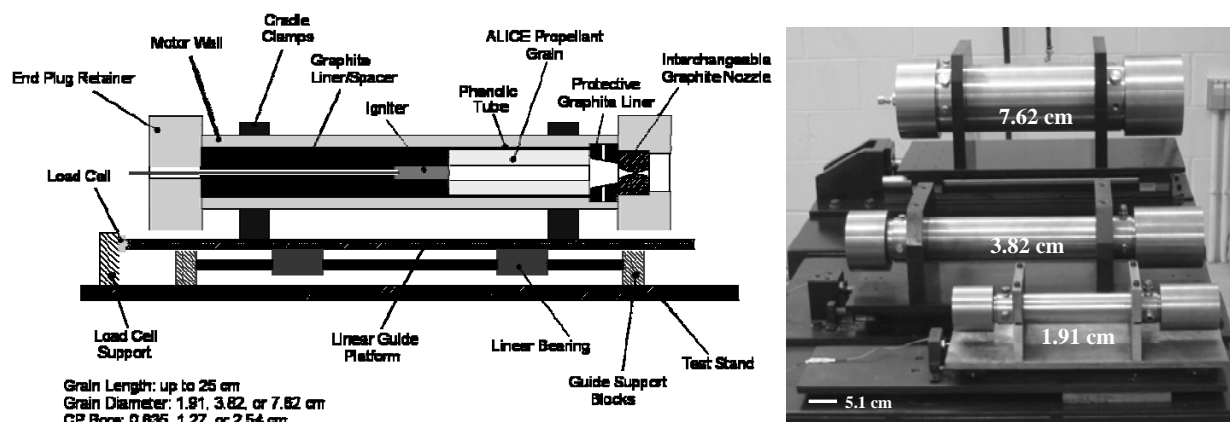
Figure 4: Schematic-diagram and photograph or three motors: 1.91, 3.81, and 7.62 cm. The schematic represents the center-perforated configuration.

Each motor has the capability of housing different pre-cut nozzles to regulate pressure and propellant cast into phenolic tubes. For the entire testing series in all three motors, the graphite nozzles had conical converging and diverging sections with the diverging section employing an expansion ratio of 10 and a divergence half angle of 15 degrees. Depending on the motor size, ignition was achieved using various sizes of commercially-available Estes and Aerotek model rocket engines. These engines are initiated with a small squib that required a 12 VDC input. Depending on the motor scale, the appropriate OMEGA loads cells were used (110, 440, and 1100 N) to determine the instantaneous thrust of the motor. Data were recorded at 5 kHz using a custom LabVIEW data acquisition program. The assembly and disassembly of the motor required virtually no tooling. The grain was cartridge-loaded followed by a nozzle holder plug which used a piston-type seal. An end-retainer cap was then threaded to secure the grain, post combustion chamber, and nozzle in their respective locations.

Results and Discussion

A series of experiments was conducted to characterize the ignition and combustion behavior of aluminum-ice (ALICE) propellants. These experiments included particle characterization using TGA to determine the active aluminum content, BET analysis to determine particle surface area, SEM to ascertain high-resolution particle images and EDS to obtain the elemental map of the particles. In addition to the characterizations tests, combustion performance was investigated using a windowed constant volume strand burner to determine the steady-state burning rate of the propellants and various lab-scale solid propellant motors to obtained pressure and thrust profiles for various solid propellant compositions and grain geometries.

Strand-Burner Results

The results of the strand tests provided input data to a lumped parameter model for determining the peak pressure in the chamber as a function of nozzle throat size. The model results

provided guidance for the design of the motor experiments. Figure 5 shows a series of video images of ALICE burning at a pressure of P = 3.55 MPa and an equivalence ratio of 0.71.
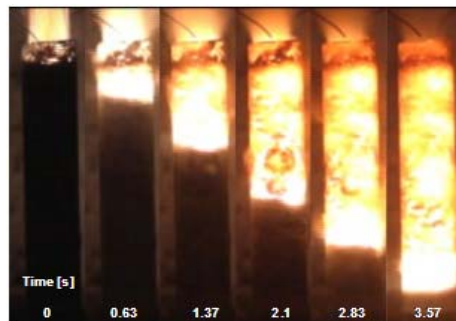
Figure 5: Captured images of an 80-nm Novacentrix ALICE mixture combusting at 3.55 MPa at Φ = 0.71.

In each figure, the frame at time zero corresponds to the instant just before the sample is ignited. From image 2 (0.63 s later), it is evident that the propellant exhibits a nearly 1-D burning front as the flame steadily propagated downward until the reactants were consumed. A visible flame appeared attached to the burning surface indicating ignition at or near the surface. For both ALICE and composite propellants, the luminous flame appears always to be attached to the burning surface of the propellant strand, which is a characteristic of AP-containing propellants. From the position vs. time plots, a burning rate law expression as a function of chamber pressure for ALICE is shown in Figure 6 for ALICE at Φ=0.71 The pressure exponent for the ALICE formulation was 0.67. Also in Fig. 6 are linear burning rates for strands in which mixing was accomplished with the Resodyn mixer. The densities of the Resodyn-mixed strands (1.48 g/cm^3) were very close to those obtained by hand mixing (1.44 g/cm^3). As evident from the figure, the linear burning rates (and hence) mass burning rates are in good agreement. Figure 7 exhibits the linear burning rates for the two composite AP mixtures. The non-aluminized AP composite propellant had a pressure exponent of 0.25 and the metallized AP had a pressure exponent of 0.44 for the ranges of pressures tested. According to Sutton [30], the observed burning rates for both non-aluminized and aluminized composite propellants fall within other data published in the literature.
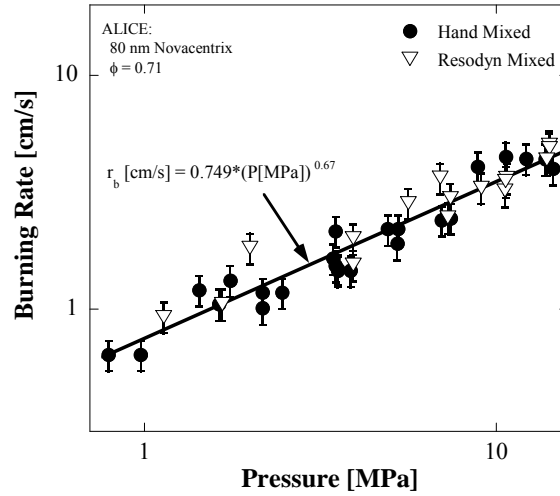
Figure 6: Linear burning rate of ALICE as a function of pressure for an equivalence ratio of 0.71. Both hand-mixed and machine-mixed results are presented.
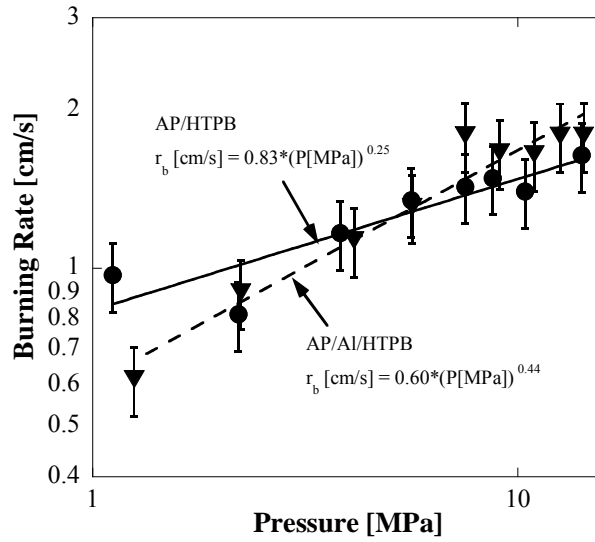
Figure 7: Linear burning rate of non-aluminized and aluminized composite propellants as a function of pressure. The mixture formulations are given in Table 4.

Figure 8 shows a comparison of burning rates of nAl mixtures with liquid versus frozen water as the oxidizer. The equivalence ratio for both was unity. Interestingly, the pressure exponent changes slightly from approximately 0.43 to 0.27 when the phase of the water is changed from a solid to liquid form. Equilibrium calculations indicate that the propellants that are frozen contain solidified alumina in the combustion products.
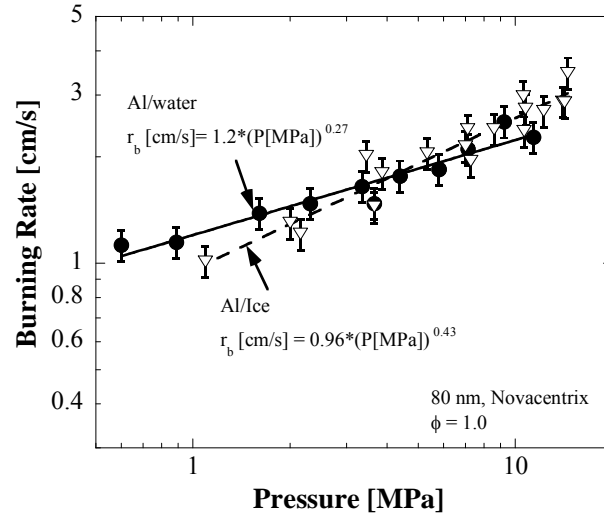
Figure 8: Comparison of nAl-ice and nAl-liquid water burning rates both with Φ = 1 as a function of pressure.

The adiabatic flame temperature is constant (~2327 K) throughout the pressure range and the physical mechanism for this isothermal behavior is the phase change from solid to liquid alumina. The liquid water system is not controlled by the heat of fusion of alumina since there is no solid alumina in the products and the adiabatic flame temperature is higher than the melting temperature of aluminum oxide. As a consequence of the change in slope, there is an inherent temperature sensitivity effect between the Al/water and ALICE mixtures. Classically, the initial propellant temperature affects the pre-power factor and not the pressure exponent. For ALICE, both the pre-power factor and the pressure exponent are affected. Unlike conventional propellants where temperature conditioning does not impose phase change, ALICE propellants posses phase change. According to simple flame theory, the change in the initial state of water from liquid to solid (and hence a decrease in initial temperature), would decrease the burning rate as a result of the increase in sensible enthalpy necessary to raise the grain temperature to the surface temperature and the increase in energy required to overcome the heat of fusion. However, neither of these changes would be expected to have a significant effect on the pressure exponent. The pressure exponent may be affected by a change in the type of reaction or a change in the efficiency of the reaction with pressure. Because the equilibrium temperatures for both ALICE and Al/liquid water mixtures are below the Al vaporization temperature, the nAl will burn heterogeneously at one-limit through a kinetically-controlled first order reaction between the water and aluminum or at another limit through a diffusion-controlled reaction across the oxide layer covering the particle surface. For the ice system with even a lower flame temperature and at low pressures, an increase in temperature (to the liquid system) could change the system from a kinetically-limited system to a diffusion-limited system, which would result in a decrease in pressure exponent. The decrease in temperature at lower pressures may result in a lower conversion efficiency, which would lower the temperature further and consequently indirectly increase the pressure exponent if conversion efficiency increases at higher pressures. For example, Risha et al. [27] have previously reported for fuel lean 38-nm Al-water mixtures (Φ = 0.67), a decrease in conversion efficiency for low pressures.

Lab-Scale Motor Results

In addition to the strand-burner experiments, a series of static motor experiments have been performed using ALICE with an equivalence ratio of $\Phi = 0.71$ and non-aluminized and aluminized composite propellants. More than 100 lab-scale static motor tests were conducted using 1.91, 3.82, and 7.62-cm (0.75, 1.5, and 3-in) motor chambers. ALICE propellant grains in both end-burner and center-perforated (CP) grain configurations were examined to investigate performance parameters such as thrust, stability, total impulse, and chamber pressure.

End Burner Grain Configuration

End burner grain configurations maintain a constant burning surface area throughout the burn which provides a neutral thrust profile and were studied because of their simplicity in casting and longer burn times. The end-burner grains were ignited by attaching a small square piece of high-burning rate composite propellant to the end of the grain. The composite propellant was then ignited using a small resistance coil coupled to a smokeless powder NC/NG lacquer. Grain lengths ranged from 2.54 to 15.24 cm (1 to 6 inches) long and were tested in both the 1.91 and 3.82-cm motors. It was found that ignition was very difficult. Two ignition criteria had to be met: (1) the pressure in the system had to reach above ∼ 40 psig and (2) the duration had to be sufficient to deliver enough energy to the propellant surface. When poor ignition was achieved, the motor virtually changed into a low pressure hydrogen generator, where hydrogen gas exited the nozzle for several minutes as the reaction front slithered through the propellant grain.

Figure 9 is a pressure and thrust profile from a typical end-burner configuration motor firing. Specifically, this test consisted of a 15.24-cm long ALICE grain in the 3.82-cm motor having a 0.325-cm diameter nozzle. Time zero corresponds to the ignition of the main ALICE grain. Once the ALICE grain was fully ignited, the pressure reached 7 MPa (1,015 psia) and quickly equilibrated to a quasi-steady burning process. The thrust profile followed the pressure very well indicating that there was no mechanical influence of the thrust stand on the measurements. The slight variation in pressure during the quasi-steady portion of the burn can be attributed to some transient nozzle blockage due to the large amounts of alumina produced. Once the baseline end-burner was established and repeatability of ignition and combustion was successful, experiments were then conducted using a center-perforated grain (CP). CP grains provide a large burning surface area, thereby requiring a larger nozzle, which in turn reduces the influence of slag accumulation on the nozzle surface. Furthermore, larger thrust levels can be obtained while minimizing the grain mass for each test. However, burn times are governed by the diameter of the ALICE grain rather than the length of the grain, ultimately requiring a larger diameter motor.

The plot shows:
- Title: ALICE-042 (8-27-2008)
- Parameters: $\phi = 0.71$; 80 nm, ICE; $D_{noz} = 0.325$ cm; $D_{grain} = 3.81$ cm; $L_{grain} = 15.24$ cm
- Y-axis (left): Pressure [MPa]
- Y-axis (right): Thrust [N]
- X-axis: Time [s]
- Curves labeled: Pressure, Thrust
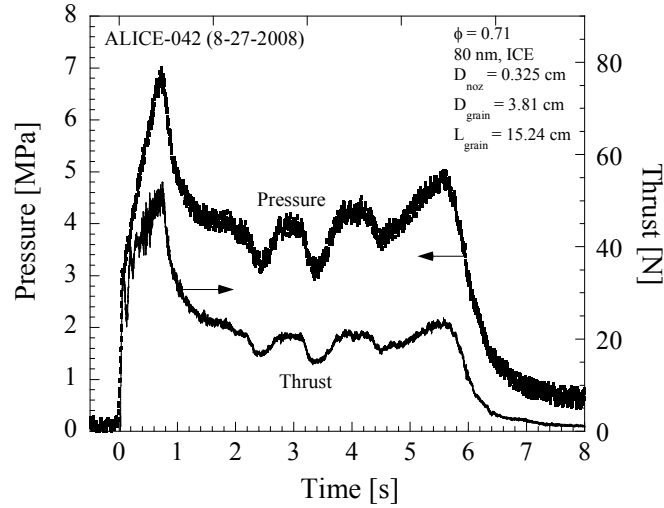
Figure 9: Thrust and pressure profiles for 3.82-cm ALICE end burner propellant grain at Φ = 0.71.

Center-Perforated (CP) Grain Configuration

Subsequent to the end-burner grain testing, a series of CP motor experiments was conducted employing all three ALICE motors having both horizontal and vertical positions. For the CP testing series, three propellant formulations were studied: ALICE, non-aluminized composite, and aluminized composite propellants. Ignition for all motor scales employing center-perforated propellant grains was achieved by using commercially-available hobby rocket motors. These motors are readily available, cost effective, and well-characterized. Because ignition of ALICE propellants is somewhat difficult to ignite and require both high pressure and sufficient heat delivered to the grain surface, reliable and repeatable igniters were required. Initially, igniter characterization tests were conducted to isolate the effect of the ignition source on the entire process. Igniters were carefully selected so that the igniter mass flux did not overdrive the ignition and combustion processes of the ALICE or composite propellant grain. Therefore, each igniter in its respective motor had to be characterized. A summary of the igniter characterization tests is given in Table 5. The igniter size is increased as the motor scale increased due to the free volume of the systems and the internal surface area of the propellant grain. Also in the table are data showing the impact of the igniter on the peak thrust of the propellant grain. For the largest igniter, a maximum of only 8.5% of measured thrust resulted from the igniter. In most cases, this percentage was considerably lower.

Table 5: Experimental results of the igniter characterization tests.

Igniter Type	Motor Scale [cm]	Peak Thrust [N]	Peak Pressure [kPa]	Nozzle Throat [cm]	Ignition Stimulus Effect [%]
Estes, A-10	1.91	< 2.20	356	0.457	~ 2.5
Estes, D-12	3.82	< 2.2	343	0.635	~ 1
Aerotek, G-80	7.62	~ 45	494	0.899	~ 8.5
Aerotek, G-80	7.62	~ 129	915	0.843	

In addition to evaluating the impact of the ignition source on the motor thrust, tests were conducted to evaluate the influence of chamber pressure on ignition delay. These tests were conducted with the same igniter (D-10) in the 3.82-cm motor. The nozzle throat diameter was varied to change the pressurization rate and peak pressure of the igniter. The dependence of the ALICE grain ignition delay on nozzle diameter is shown in Figure 10. Although desirable to have a short ignition delay, the nozzle had to be chosen based upon the peak pressure of the main ALICE grain rather than the ignition pressure. However, larger igniter grains could be chosen to deliver higher pressurization rates if necessary. Although, not shown here, the ignition delay trends were very similar in the 1.91-cm motor.
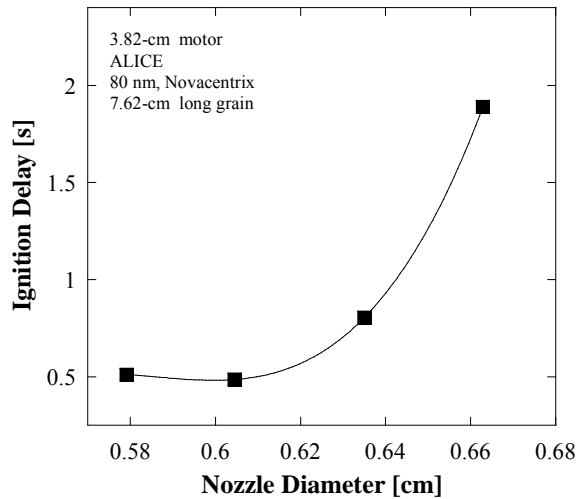
Figure 10: Ignition delay for the 3.82-cm ALICE motor as a function of nozzle diameter.

In the process of scaling to larger motors, repeatability of the CP grains was examined and verified. Figure 11 shows typical repeatability of the experiments in the 1.91-cm motor. Furthermore, the effect of motor orientation was examined to verify that the horizontal static firings were representative of vertical launch position orientation. The results for both orientations

were very similar. Thus, for ease of measurements, the remaining tests were conducted horizontally. As shown in the figure, the maximum chamber pressure reached approximately 9.1 MPa (1,315 psia).
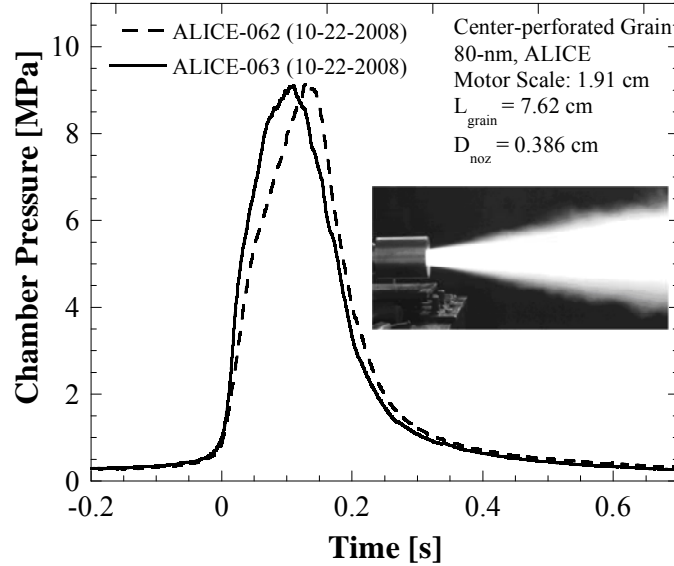
Figure 12 and Figure 13 display the pressure and thrust for three tests using the same ALICE grain composition but different nozzles. As nozzle diameter increases from 0.635 to 0.711 cm (0.250 to 0.280 in), the pressure is reduced from 10.4 to 7.7 MPa (1,515 to 1,115 psia). Although the pressure decreases as the nozzle diameter is increased, the overall thrust remains virtually the same, which indicates, in terms of thrust, that once a critical combustion pressure is achieved the performance is not significantly affected. This can be shown by the definition of thrust, $F = C_f P_c A_{th}$. For 7.62-cm long grains, peak thrusts are approximately 134 and 311 N for the 1.91-cm and 3.82-cm motors, respectively. Burning times are approximately 0.22 and 0.5 s.

Figure 14 shows the results from a 7.62-cm motor firing. As expected, the thrust increased to nearly 890 N at the same chamber pressure of around 8 MPa (1,165 psia) compared to the 3.82-cm motor. The burning time for 7.62-cm grains is slightly longer due to the increased web thickness. It is evident from the data in the figure that the igniter does not overpower the combustion process of the ALICE grain. Also, there is no noticeable ignition delay.
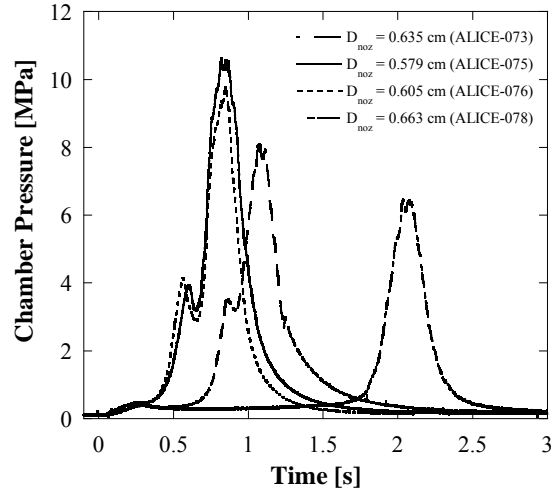
Figure 12: Typical pressure profiles for center-perforated grain configurations in the 3.82-cm motor using ALICE propellant at Φ = 0.71.
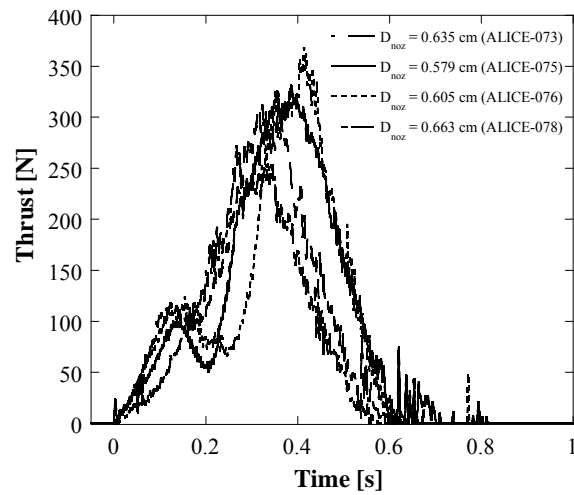
Figure 13: Typical thrust profiles for center-perforated grain configurations in the 3.82-cm motor using ALICE propellant at Φ = 0.71.

29
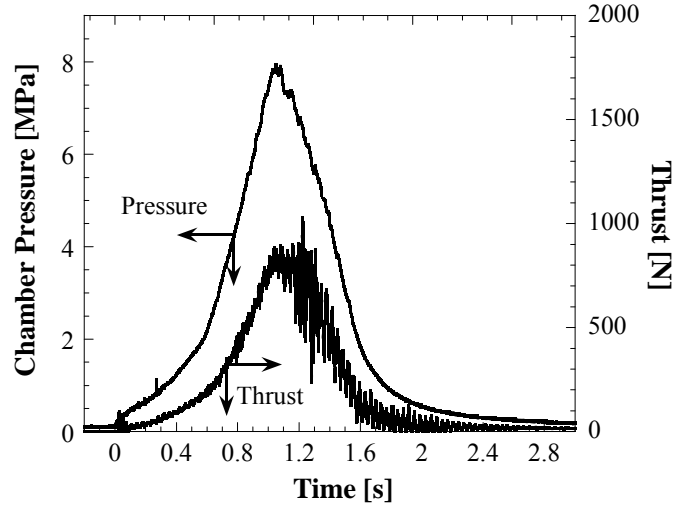
Figure 14: Typical pressure and thrust profiles for center-perforated grain configurations in the 7.62-cm motor using ALICE propellant at Φ = 0.71.

Motor Scaling

Scaling of the motors was performed using geometric similarities and volumetric loading fraction. One simple criterion of designing solid propellant rocket systems is the volumetric loading fraction [30]. The volumetric loading fraction (VLF) is the ratio of the volume occupied by the reactive propellant materials (propellant grain) and the chamber free volume, not including the nozzle. Typical volumetric loads ranged from 0.8-0.95 [30]. For all three of the motor chambers, using 3.82-cm long propellant grains, the loading fraction is 0.8. Figure 15 and Figure 16 exhibit the pressure-time and thrust-time profiles of ALICE propellants for two different motor scales. It was found that the pressure profile of the 7.62-cm motor had a more broad distribution, which is indicative of a longer burn time due to the increased web thickness. Also, because the length of the grain was fixed in these experiments, the initial center-perforated surface area relative to the initial grain-end surface area decreased with increasing motor size. From the similarity in the thrust and pressure profiles between all different motors, a significant change in burning mode (e.g., more end burning than center-perforated burning) is not apparent from the results.

30
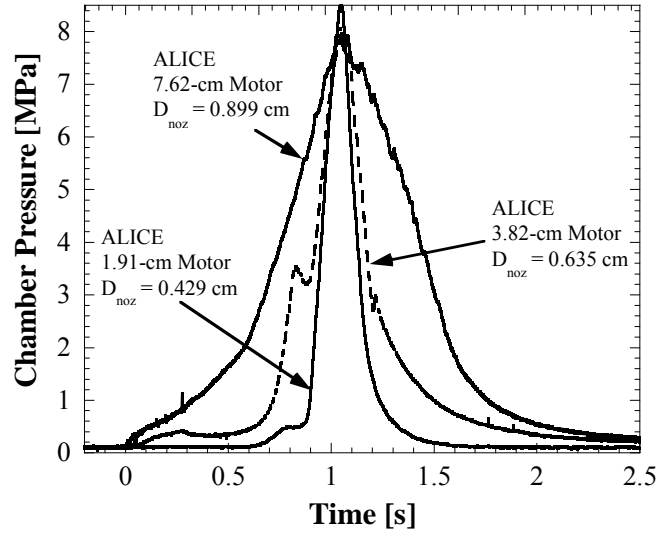
Figure 15: Pressure profiles from ALICE tests conducted in the 3.82 and 7.62-cm motors. Time was adjusted to align peak pressures.
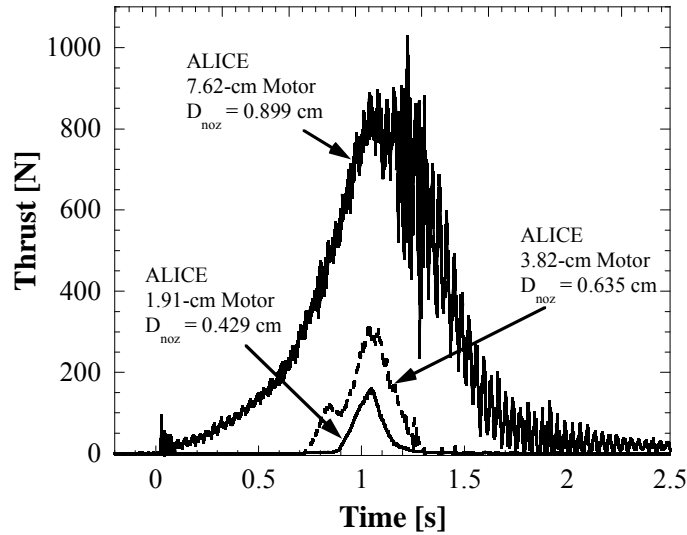
Figure 16: Thrust data from ALICE tests conducted in the 3.82 and 7.62-cm motors. Time was adjusted to align peak thrust.

To achieve comparable pressures using the ALICE composition, the 3.82 and 7.62-cm motor nozzles were 0.635 and 0.899 cm, respectively. The peak thrust for the 7.62-cm motor was nearly 890 N and the thrust for the 3.82-cm motor was ~ 311 N. The peak thrust correlates with the surface area of the propellant at a constant grain length. The peak thrust for each motor is given in Figure 17. Each motor size has several test firings plotted individually and then the average of those points are indicated on the plot. From geometric scaling, the thrust should scale with mass burning

rate of the propellant, which is linearly dependent on surface area. The inner grain surface area is given by $A_s = \pi * D * L$. Ultimately, thrust scales linearly with inner grain diameter. Assuming that the thrust is $F \sim a*(D)^n$, then the ideal scaling would be where $n = 1$ and a is a constant. For the current tests, $n = 1.4$, and thus, it may be anticipated that appreciable losses still exist in the 7.62-cm motor.
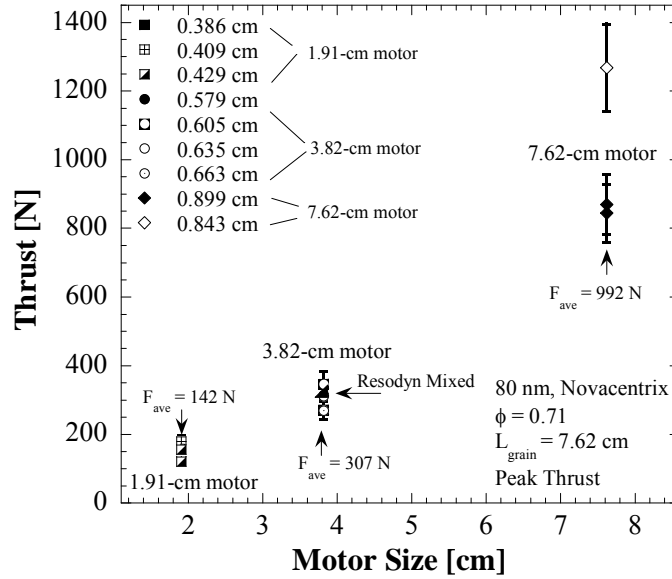
Figure 17: Scaling of 1.91, 3.82, and 7.62-cm ALICE motors with a center-perforated grain configuration.

Total impulse is the product of the thrust and burning time. Effectively, it is the amount of momentum that the reaction of the chemical system can yield using a specified family of ingredients which can be imparted to a vehicle. Figure 18 reveals that the total impulse for the larger scale motors is higher. This is expected since the thrust levels of the large motor are significantly larger without increasing the burning time very much. For the 1.91-cm motor, the totals impulse is approximately 20 N-s. If the grain diameter is increased by a factor of four to 7.62-cm, the total impulse increases by a factor of 30. Depending on the mission of the spacecraft, the figure of merit may be different.

In these systems, specific impulse is a very difficult parameter to quantify. The major problem with the calculation is the determination of the experimental propellant mass flow rate since it varies during the experiment. Consequently, an estimate regarding the instantaneous profiles was performed. The remaining mass left in the chamber was collected after each experiment and weighed to determine the amount of mass ejected from the nozzle (see Table 6). Typical percentages of mass left in the chamber ranged from 20 to 43%. Here, the average mass retained is defined as the ratio of the mass left in the chamber to the initial propellant mass.
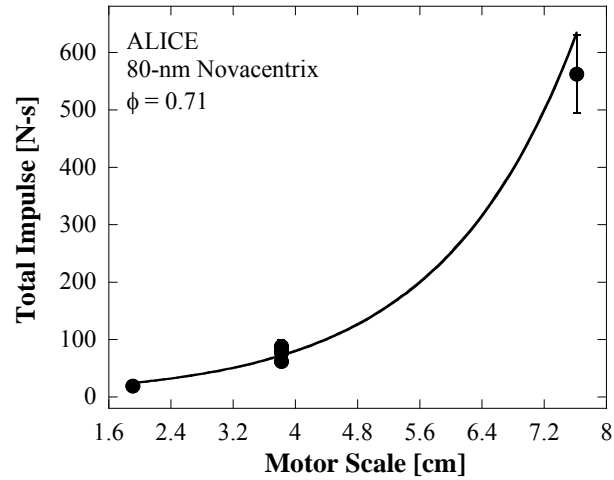
Figure 18: Total impulse of ALICE propellants in various motor sizes.

Table 6: Mass remaining in the motor chamber subsequent to a hot firing.

Motor Scale	Average Mass Retained
[cm]	[%]
1.91	20.28 ± 14.69
3.82	29.44 ± 3.65
7.62	43.15 ± 1.0614

There are several factors which affect the variation of mass accumulated in the chamber during the test. Independent of scale, the post combustion chamber length was kept constant at 7.62 cm. The benefit of this post combustion cavity is to promote further mixing and reaction prior to exiting the nozzles. The drawback to this extra reaction chamber is that it can allow mass to accumulate and be isolated from the high-velocity product gas flow. Removing this chamber may reduce molten combustion products accumulation in the combustion chamber, but it may also sacrifice some combustion efficiency by reducing the residence time of the reactants in the chamber. The examination of these trade-offs is currently under investigation.

A summary of the motor experiments is presented in Table 7. As shown in the table, measured specific impulse increases with motor size, although are low compared to theoretical values. To calculate the combustion and specific impulse efficiencies, the theoretical values were determined using the NASA Chemical Equilibrium Code [31] using the actual experimental test conditions as input. Results indicate for ALICE propellants that the Isp efficiencies increased from 27 to 64%, going from 1.91 to 7.62-cm (0.75 to 3-in) motor size. Also shown in the table are combustion efficiencies which range from 43 to 69%, indicating that a substantial portion of the

low specific impulse is a result of poor combustion efficiency. According to previous Al/water results [27], the combustion efficiency for 80-nm Al/water strands in a closed volume were greater than 80%. If the data at maximum thrust or equivalently maximum pressure is used to obtain and instantaneous Isp assuming its surface area equals 90% of the outer grain diameter surface area, the estimated Isp would be 97, 124, and 203 seconds for the 1.91, 3.82, and 7.62-cm motors, respectively. Because the burning rate data and previous combustion efficiency experiments suggest higher pressures are beneficial for better combustion, these conditions might be those expected if the motor is designed to operate at high pressures for a greater period of time. The decreased combustion efficiency may be a result of the low combustion temperatures for lean equivalence ratios (where solid-phase alumina may inhibit combustion) insufficient residence time for complete aluminum oxidation, and possible agglomeration of nanoaluminum at the particle surface.

Table 7: Summary of performance parameters for ALICE and non-aluminized composite propellants.

Parameter	Motor Size [cm]		
	1.91	3.82	7.62
Peak Thrust (N)	133	331	992
$\overline{C}^*$ (m/s)	528	784	848
$\eta_{\overline{C}^*}$ (%)	43	64	69
$\overline{I}_{sp}$ (s)	56	83	133
$\eta_{\overline{I}_{SP}}$ (%)	27	40	64
Isp @ Peak Pressure (s)	97	124	203
$\overline{I}_{sp}$ with Al_2O_3 retained (s)	63	117	233
$\eta_{\overline{I}_{SP}}$ (%) AP/HTPB (Isp_{theor} = 240 s)	87	92	NA
$\eta_{\overline{C}^*}$ (%) AP/HTPB (C^*_{theor} = 1466 m/s)	57	90	NA

The calculated specific impulse values were based upon all of the mass being ejected out of the nozzle. However, if the alumina remaining in the chamber is considered as not exiting the nozzle, then corrected specific impulse values will be higher as shown in the table. As a comparison, the characteristic velocity and specific impulse efficiencies for the AP/HTPB propellants tested are given in the table. Results from tests in the 1.91-cm motor indicate appreciable losses observed for both efficiencies. However, for the 3.82-cm motor, both efficiencies are greater than 90%, indicating that the performance is nearly independent of system size. In contrast, larger motor sizes may still

be important for characterizing the ALICE propellant. It is interesting to note from a systems standpoint, the composite propellants require a much larger nozzle throat area to achieve the same chamber pressure as ALICE, which is due to the higher gas generation. In a geometrically limited system, ALICE propellants require a 31% smaller nozzle exit diameter for the same expansion ratio. Therefore, the exit area can be increased, yielding a lower exit pressure and larger expansion ratio enabling higher thrust.

Bimodal Aluminum Compositions and Ice

Due to their high surface to volume ratio, nAl particles can have significant amounts of an oxide layer covering the particle surface, passivating the aluminum and preventing pyrophoric reaction. From a performance perspective, specific impulses, which may be evaluated from the total impulse delivered by the motor divided by the mass of the propellant, suffer a significant loss as a consequence of the presence of the thick oxide layers on nAl. Because micron particles have a significantly larger fraction of active aluminum content (generally between 95-99%), the performance of the aluminum and ice propellants may simply be improved by replacing a portion of the nanometer aluminum with micron aluminum provided combustion rates remain fast enough to achieve complete combustion in the short available residence times.

The combustion of aluminum with ice is studied using various mixtures of nano- and micro-meter sized aluminum particles as a means to generate high temperature hydrogen at fast rates for propulsion and power applications. Bimodal distributions are of interest in order to vary mixture packing densities and nascent alumina concentrations in the initial reactant mixture. In addition, the burning rate can be tailored by introducing various particle sizes. The effects of the bimodal distributions and equivalence ratio on ignition, combustion rates, and combustion efficiency are investigated in strand experiments at constant pressure and in small-scale (1.91 cm [0.75 in] diameter) combustion chambers with center-perforated propellant grains. The aluminum particles consisted of nanometer-sized particles with a nominal diameter of 80 nm and micron sized particles with nominal diameters of 2, 5, 10, and 20 microns. The micron particle addition ranged from 0 to 80% by mass in the mixture. Burning rates from near atmospheric pressure to 15 MPa (2175 psia) are determined. From the small scale motor tests, thrust, C*, Isp, and C* and Isp efficiencies are provided. From these results, mechanistic issues of the combustion process are discussed. In particular, overall lean equivalence ratios that produce flame temperatures near the melting point of alumina resulted in considerably lower C* and Isp efficiencies than equivalence ratios closer to stoichiometric. The substitution of micron aluminum for nanometer aluminum had little effect on the linear burning rates of Al/ice mixtures for low mass substitutions. However, as the mass addition of micron aluminum increased (e.g., beyond 40% 2-µm aluminum in place of 80 nm aluminum), the burning rates decreased. The effects of bimodal aluminum compositions on motor performance were minor, although the results suggest longer combustion times are necessary for complete combustion.

Figure 19 illustrates the increase in active content of the aluminum fuel consisting of a bimodal particle distribution as nanometer particles with a nominal diameter of 80 nm are replaced with micron particles with a nominal diameter of 2 μm. Progressing from a pure nanoparticle fuel to one with a 50% nAl and 50% μm Al (by mass) consistency, the active aluminum content increases by ~13%. Figure 20 shows the manner in which this change in active aluminum content affects the flame temperature and Isp of the propellant. The flame temperature increases by ~110 K and the Isp increases by ~11 s by replacing 50% of the mass of 80 nm aluminum with 2 μm aluminum.
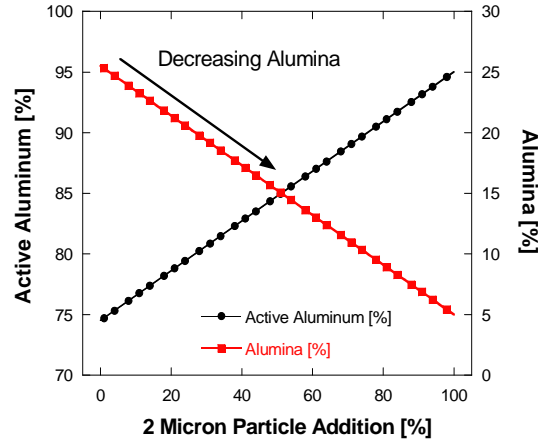
Figure 19: Active aluminum content versus bimodal aluminum distribution. The mixture consisted of various amounts of 80 nm and 2 μm aluminum.

The addition of micron aluminum to a base fuel consisting only of nanometer aluminum is studied to reduce the initial alumina (inert mass) in the composite propellant and to provide control of the burning rate independent of the mixture ratio. The effects of equivalence ratio are also studied because changes in the particle size distribution also affect the mixture consistency (Risha et al. 2007 [10]). Linear burning rate measurements are performed as a function of micron aluminum content in the fuel mixture, equivalence ratio, and pressure. Motor performance studies are performed with a center-perforated grain in a small laboratory scale 1.91 cm (0.75 in) diameter motor.
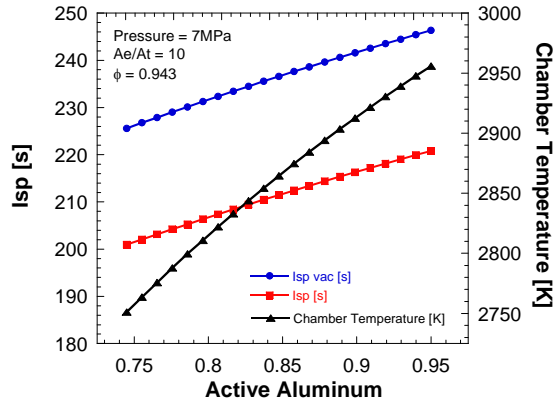
Figure 20: Isp and exhaust product alumina as a function of the active aluminum content in for an equivalence ratio of 0.943. The calculations were performed with CEA (Gordon and McBride, 1996).
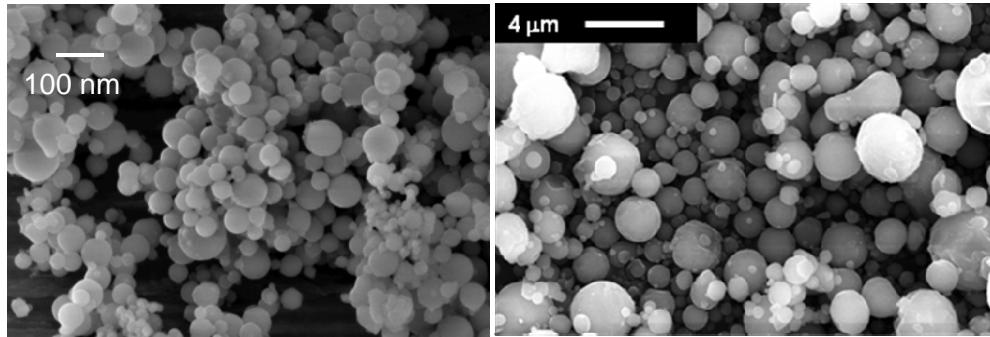
Figure 21: SEMs of 80 nm and 2 μm aluminum particles. The active content of the nAl was 74.5% and 95% for the μAl. The 80 nm SEM image is courtesy of Mr. Ed Roemer and the 2 μm image is courtesy of Mr. Justin Sabourin.

Experimental Procedure

The baseline propellant formulation consisted of nanometer and micron aluminum and de-ionized water. The nanoaluminum particles were obtained from Nanotechnologies, Inc. and had a nominal diameter of 80 nm. The micron aluminum particles were obtained from Valimet and Sigma Aldrich had nominal diameters of 2, 5, 10, and 20 μm. Scanning electron microscopy images of the 80 nm and 2 μm aluminum are shown in Figure 21. Both sizes of particles had spherical shapes. The active aluminum content of the "as received" nanometer aluminum was generally around 77-79%. However, in the present studies, just as in our previous studies, further passivation of the nanometer aluminum was performed to achieve an active content of ~74% (Risha et al. 2009 [13]). The additional passivation was performed to minimize any low temperature oxidation with the liquid water during mixture prior to freezing. Once the mixtures were frozen, no oxidation of the nAl has been observed. The 2 and 5 micron aluminum had an active content of ≥ 95%, while the larger particles had better than 99% active fuel content.

For all mixtures with combined nanometer and micron sized aluminum, a Resodyn LabRAM® mixer was used to premix particles. Figure 22 shows the separated nAl and µAl before mixing and the quasi-homogeneous particle mixture after mixing. De-ionized water was then added to the bimodal powder mixture and the final mixing was performed by hand. As more micron aluminum was added to the mixture for a given overall stoichiometry, the mixture consistency changed from a clay-like to a paste to a slurry mixture. The more fluidic, less viscous, mixture resulted from the significantly lower surface area of the micron versus nanometer aluminum. For an equivalence ratio of 0.71, a micron aluminum content of ~ 20% relative to the total active aluminum content could be achieved prior to significant settling of the micron aluminum in the unfrozen mixture. For an equivalence ratio of 0.943, a micron content of ~80% was achievable prior to significant settling of the micron aluminum. As a consequence, most of the combustion studies considered here was performed with an equivalence ratio of 0.943. After packing the tube molds, either for strand tests or scale motor tests, the material was placed in an explosion proof freezer and stored at -35°C. Phenolic tubes were used for the motor grains while quartz tubes were used for the strand burner tests. Densities varied with the micron aluminum content of the mixture and are illustrated in Figure 23. For mixtures with an overall equivalence ratio of 0.943, a decrease in mixture density from about 1.6 to 1.5 g/cm³ was observed with the substitution of 80% the aluminum mass with micron aluminum.
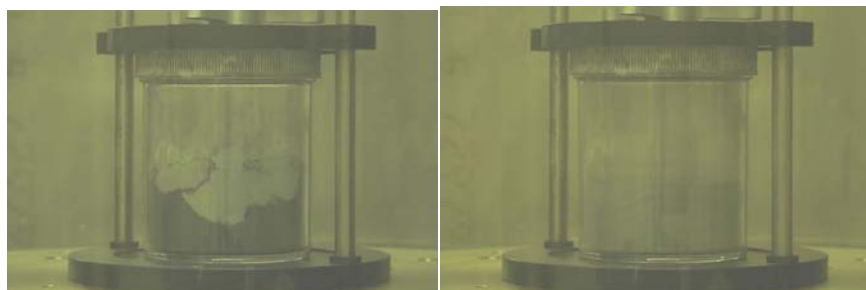
Figure 22: Photographs of the bimodal aluminum powder mixture before and after mixing with the Resodyn mixer.
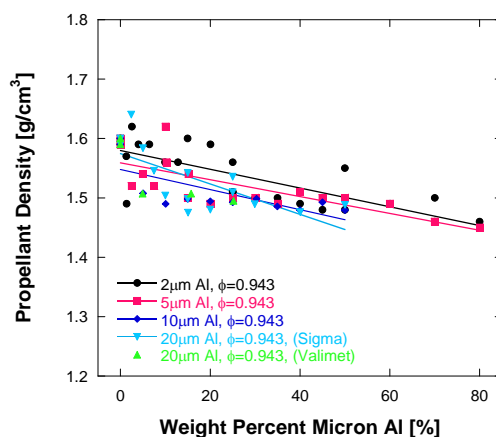
Figure 23: Mixture density as a function of micron Al substitution of nanometer aluminum in aluminum ice mixtures with an equivalence ratio of 0.943.

38

Experimental Analysis

Constant pressure strand tests were conducted for compositions containing 80nAl and micron Al using the same methods as described for the baseline composition, using two equivalence ratios (0.71 and 0.943). Motor tests were conducted using center-perforated grains fired using the 1.91 mm (0.75 in.) system previously described.

Burning Rate Measurements

Figure 24 shows exemplary trajectory plots of the flame position in the 8 mm ID quartz tubes as a function of time for three pressures and a 75% nAl / 25% µAl and ice mixture with an equivalence ratio of 0.943. Steady-state flame propagation was observed for all the reported results.
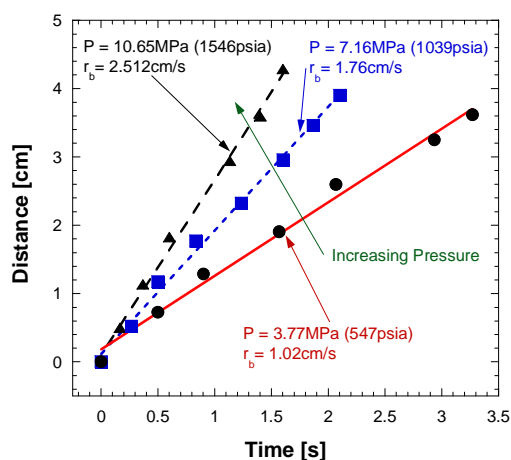
Figure 24: Trajectory plots of strand burning distance versus time.

The burning rates for mixtures of 80 nm aluminum with 2 µm aluminum at 7 MPa (1014.7 psia) are shown in Figure 25a. Burning rates for mixtures of 80 nm and 5 µm aluminum at the same conditions are shown in Figure 25b. For both sizes of micron particles, a slight increase in burning rate is observed with the addition of small amounts of micron aluminum. The addition of large amounts of micron aluminum decreases the burning rate. Figure 26 provides normalized results for 2 through 20 micron Al particle addition. The results are normalized because several batches of nAl (M2671 and M2548) were used during testing which influenced propellant burning rates. The decrease in burning rate is evident at a lower amount of substituted micron aluminum for the 5 µm aluminum (~ 20%) compared to the 2 µm aluminum (~40%). The slight increase in burning rate likely results from a slightly higher reaction temperature due to lesser inert alumina initially present in the mixture. However, as the amount of micron aluminum increases, the propagation rate becomes more rate-limited by the larger particles than any further increase in reaction temperature and the burning rate decreases. The results suggest that in addition to reducing alumina in the initial mixture, bimodal distributions may be used to control burning rates.
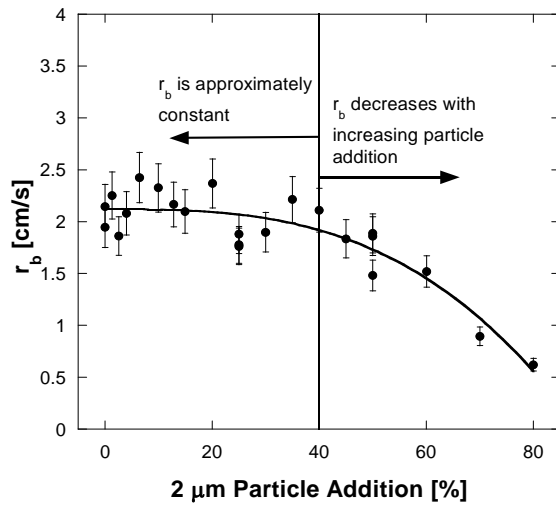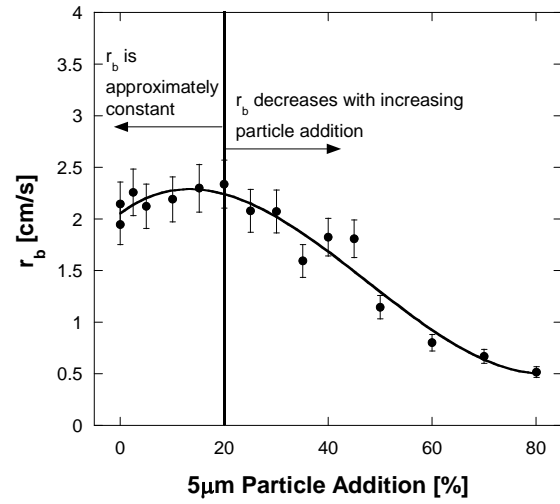
Figure 25: Linear burning rate as a function of 2 micron (a) and 5 micron (b) aluminum content in the fuel mixture for an equivalence ratio of 0.943 and pressure of 1.46 MPa (1014.7 psia).
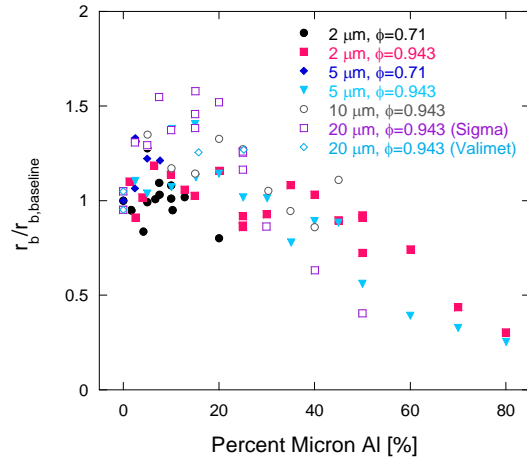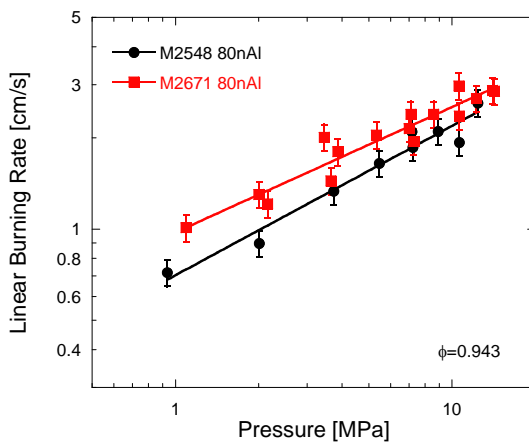
Figure 26: 80nm baseline propellants (a) and normalized propellant burning rates (b) for compositions having varied wt% micron Al at constant pressure.

Figure 27 shows the burning rate as a function of pressure for mixtures with only 80 nm aluminum and mixtures with substitution of 25 and 50 percent by weight of the 80 nm aluminum with 2 micron aluminum. The overall equivalence ratio of the mixtures was 0.943. The mixture with 25% micron has a slightly larger pressure exponent than the mixture with 50% micron aluminum (0.65 vs. 0.57). Both mixtures had a slightly larger pressure exponent than the pure 80 nm ALICE mixture (0.47). The larger pressure exponents of mixtures with micron aluminum may result from lower combustion efficiency of these mixtures at low pressures. Consistent with previous observations on the pressure dependence of aluminum and ice mixtures (Risha et al. 2009 [13]),

the present results suggest that combustion of bimodal mixtures will benefit from high pressure operation.

(a)   (b)
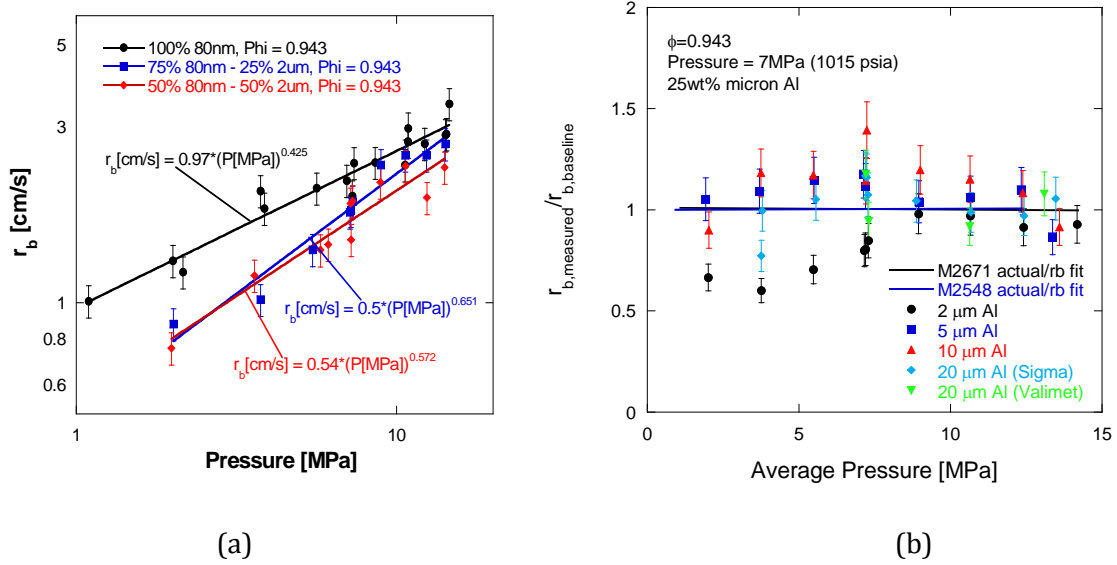
Figure 27: Linear burning rates as a function of pressure for mixtures with 100% 80 nm aluminum and mixtures with 25% and 50% (by weight) 2 micron aluminum (a) and normalized burning rates for compositions containing 25wt% 2, 5, 10, and 20 micron Al.

Bimodal Thrust and Isp Measurements

A comparison of motor experiments with propellant grains of equivalence ratios 0.71 and 0.943 for 100% 80 nm aluminum mixtures is presented in Figure 28 and Figure 29. The times were shifted so the peak pressures and peak thrusts are aligned. Figure 28 presents the chamber pressure and Figure 29 presents the motor thrust. Even though the grain with an equivalence ratio of 0.943 had a slightly larger igniter, ignition delays of the near stoichiometric mixture were longer than those of the fuel-lean mixture with an equivalence ratio of 0.71. The combustion duration is also slightly longer for the mixture with Φ = 0.943, which is consistent with the slightly lower linear burning rates of the Φ = 0.943 mixtures compared to those of the Φ = 0.71 mixtures (Risha et al. 2009 [13]). The peak pressure and peak thrust are lower for the Φ = 0.943 mixture.
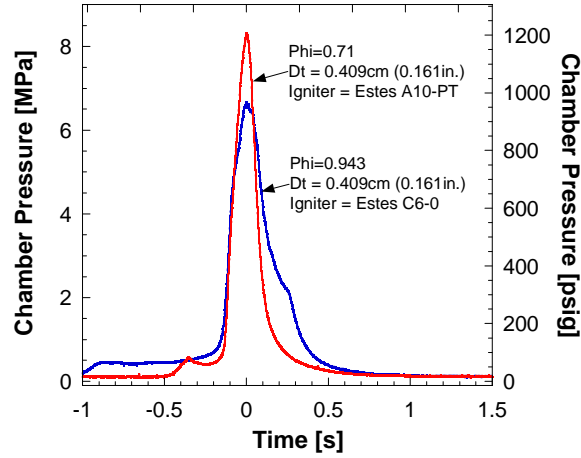
Figure 28: Comparison of chamber pressure in the 1.91 cm center-perforated grain motor for equivalence ratios of 0.71 and 0.943. The aluminum is 80 nm.
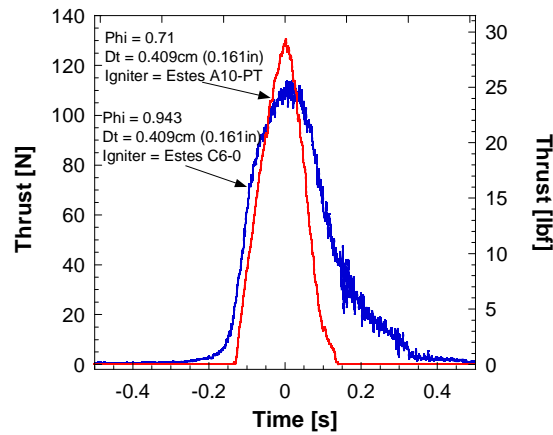
Figure 29: Comparison of thrust from the 1.91 cm center-perforated grain motor for equivalence ratios of 0.71 and 0.943. The aluminum is 80 nm.

Figure 30 reports the chamber pressure measurements from three motor experiments with ALICE grains with no micron aluminum and 25% and 50% 2 μm aluminum, all with equivalence ratios of 0.943 and an Estes C6-0 igniter motor. The times were again shifted so that the peak pressures are nearly aligned. As can be seen from the data, the peak pressures decrease and the burning time duration increases with substitution of μAl for nAl. The corresponding thrusts measurements are shown in Figure 31 indicating a similar trend as the pressure measurements, i.e., with the addition of micron aluminum, the peak thrust decreases and the burning duration increases. These trends are consistent with the slower linear burning rates of formulations with micron aluminum
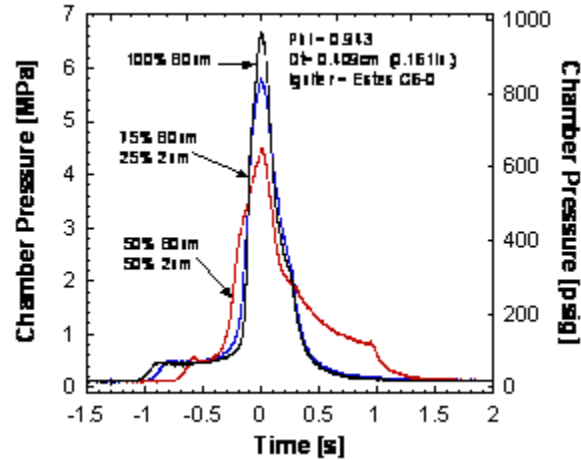
Figure 30: Pressure measurements from the 1.91 cm diameter center-perforated grain motor with nozzle diameter of 0.169" and equivalence ratio of 0.943 for grains with the fuel consisting of no micron aluminum and 25% and 50% (by mass) 2 µm aluminum.
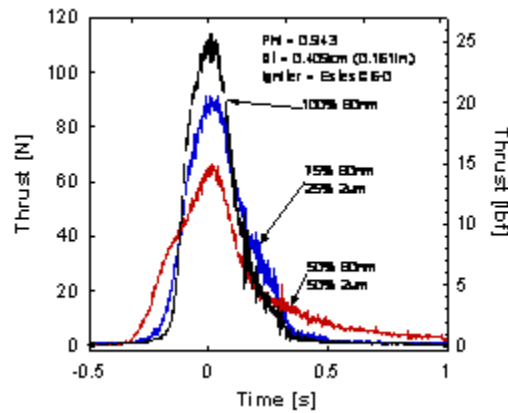
Figure 31: Thrust measurements from the 1.91 cm diameter center-perforated grain motor with nozzle diameter of 0.169" and equivalence ratio of 0.943 for grains with the fuel consisting of no micron aluminum and 25% and 50% (by mass) 2 µm aluminum.

Table 8 shows a summary of the performance characteristics of the ALICE motors with bimodal fuel particles. For the mixtures with µ = 0.943, the active aluminum content increased from 74.5 % to 84.8% as the mixture composition changed from 100% nAl to a mixture with 50% nAl and 50% µAl. The characteristic velocity is observed to increase with micron particle addition, while the C* efficiency initially changes much more slowly and then increases by ∼ 25% with the addition of 50% micron aluminum. Also evident from the table, Isp and Isp efficiency are nearly independent of the replacement of nAl with µAl (a 10% decrease is observed in going from 100% nAl to the 50% nAl / 50% µAl mixture). As one would anticipate a slight increase in Isp with the substitution of micron aluminum for nanometer aluminum, these results suggest incomplete particle combustion of micron aluminum. Visually this has been evident from the motor exhaust plumes, which are much brighter and often contain particle streaks compared to the plumes from grains without any micron particles. Even so, the performance is not hindered by the presence of

43

the micron aluminum. To enhance the micron particles burning within the chamber, longer post combustion chambers can be employed, thereby increasing the residence time of the rocket engine proving more time for the micron particles to react.

Table 8: Performance Characteristics of 0.75" Center-perforated Grain Motor

Parameter	Results			
Equivalence ratio	0.71	0.943	0.943	0.943
80 nm Novacentrix Al (%)	100	100	75	50
2 µm Valimet Al (%)	0	0	25	50
Active Al Content (%)	74.5	74.5	79.6	84.8
Peak Thrust (N)	133	115	91	66
C^*,avg (m/s)	582	670	675	881
$\eta_{C^*,avg}$ (%)	48	56	55	70
I_{tot} (N-s)	17.5	29	26	26
Isp (s)	63	96	90	89
$\eta_{Isp,avg}$ (%)	27	43	39	38
Mass remaining (%)	20.7	34.5	36.2	42
$\eta_{Isp,avg}$ (%) AP/HTPB ($Isp_{,theor}$ = 240 s)	87			
$\eta_{C^*,avg}$ (%) AP/HTPB (C^*_{theor} = 1466 m/s)	57			

Note: C^*,avg is calculated using the average nozzle throat diameter.

In comparison to the previous results of Risha et al. (2009) [13], which were all obtained with an equivalence ratio of 0.71, the present propellant grains with an equivalence ratio of 0.943 all had significantly better performance characteristics than the leaner mixture experiments. The present results have lower peak pressures and peak thrusts; however, the burning durations are longer resulting in larger total impulses. The higher equivalence ratio had a much more dramatic effect on increasing C^* and Isp efficiencies than the substitution of micron aluminum for nanometer aluminum. The increase in Isp efficiencies for all the Φ = 0.943 experiments compared to the Φ = 0.71 experiment ranged from 50-70% while the increase in C^* efficiencies ranged from 20-60%, indicating significant losses still remain in the combustion chamber. The percent mass remaining in the motor was observed to increase for the 100% nm aluminum with increasing equivalence ratio and for the Φ = 0.943 mixtures with increasing micron aluminum content. Equilibrium analysis (Gordon and McBride, 1996 [31]) of the combustion temperatures and product composition indicate that the higher temperatures of the mixtures with an equivalence ratio of 0.943

significantly reduce the amount of solid phase aluminum oxide in the combustion chamber (Table 9). The mixtures with an equivalence ratio of 0.71 have combustion temperatures constrained by the melting temperature of alumina, where the inability to melt the oxide layer on the particle surface would significantly inhibit combustion thus explaining the lower C* efficiencies of the leaner mixtures. For the Φ = 0.943 mixture, the molten alumina is solidified at the exit of the nozzle. Table 2 also indicates that the exit pressure for the Φ = 0.943 mixture is higher than the exit pressure for the Φ = 0.71 mixture, indicating that the mixture can be expanded more thus achieving additional specific impulse so that the Isp of both equivalence ratios would be approximately the same if expansion was to the same ambient pressure.

Table 9: Equilibrium analysis of ALICE with equivalence ratios of 0.71 and 0.943

	Φ = 0.71			Φ =0.943		
	Chamber	Throat	Exit	Chamber	Throat	Exit
Pressure (bar)	68.9	41.8	1.15	68.9	40.4	1.39
Temperature (K)	2327	2327	1769	2746	2628	2327
Isp (s)			208			202
C* (m/s)			1224			1198
Composition						
H	0.00088	0.00113	0.00017	0.00573	0.00477	0.00665
H_2	0.55414	0.55394	0.55467	0.68069	0.68170	0.68026
H_2O	0.22651	0.22647	0.22670	0.04388	0.04384	0.04373
OH	0.00007	0.00009	0.00000	0.00011	0.00008	0.00008
$Al(OH)_3$	0.00004	0.00003	0.00017	0.00001	0.00001	0.00000
$Al_2O_3(l)$	0.19943	0.13099	0.00000	0.26911	0.26935	0.01847
$Al_2O_3(a)$	0.01893	0.08734	0.21846	0.00000	0.00000	0.25069

Alanized Compositions of Aluminum and Ice

The hydrogen yield from a mixture of unpassivated Al and water is approximately 5.6 % on a mass basis. However, all Al particles have a passivating oxide layer, which prevents oxidation of the Al at ambient conditions. A significant portion of nano-sized Al particles is aluminum oxide (e.g., a 50-nm Al particle contains only 68% by mass pure Al [10]). Consequently, the hydrogen yields are much lower than the theoretical value for pure Al particles. Two approaches for minimizing the initial mass of aluminum oxide, and thus increasing the gravimetric yield of

hydrogen, are to replace portions of the nanometer Al with micron Al as described previously or introduce other ingredients rich in hydrogen [21,32].

Aluminum hydride, or alane, has been broadly used in many energetic materials due to its high hydrogen storage capacity (theoretically, 10.1% by weight) [33,40] Alane is a covalently bonded hydride which often appears in a polymeric form (AlH$_3$)n and has at least seven known non-solvated forms. The most stable polymorph is α-AlH$_3$ [35,41,42]. Alane decomposition or dehydrogenation (an endothermic process) has been found to be dependent on particle size [36], doping stimulants, form, structure [36], and heating rates [36,43]. Young et al. [43] found that micron-sized alane ignites in air at temperatures similar to those of nano Al particles. Decomposition temperatures have been observed to be as low as 60 ^{o}C at low heating rates with doping, and as high as 900 ^{o}C at extremely high heating rates [36,43]. In shock tube studies, Bazyn et al. [44] determined that once the hydrogen in alane has been released, the remaining Al burns on time scales equivalent to similarly sized Al particles.

Micron-sized Al particles typically contain less than 1% alumina by mass. Recently, Connell et al. [45] studied the effect of adding micron-sized (2 and 5 μm) Al particles on the burning rate of a baseline mixture containing 80-nm Al particles and water. The equivalence ratio was fixed at 0.943. The loading of micron-sized particles ranged from 0 to 80% of the Al particle mass, increasing the active Al content from ∼ 74.5% to 91%. The linear burning rate was not noticeably affected until the micron particle substitution exceeded 20% of the active fuel mass, at which point the burning rate decreased. The mixture always remained ignitable with sustained flame propagation, regardless of the loading fraction of micron-sized particles.

The present work attempts to study the effect of micron-sized alane and Al particles on the combustion and hydrogen generation of the nano-Al and water based reactive mixture. Both the reaction propagation rate and combustion efficiency were determined. The alane particles were characterized with thermal and microscopy analyses. In addition, a chemical equilibrium analysis was performed and a theoretical model of the flame propagation process was developed.

Chemical Equilibrium Analysis

In order to determine the effects of micron-sized alane and Al as additives to nAl/ice mixtures, and to identify viable reactive mixture compositions, thermo-chemical calculations were performed using the NASA Chemical Equilibrium with Applications (CEA) Program [31]. The pressure was 7 MPa (1,015 psia). The active Al content of the nano-Al was 74.5% by mass with the balance being alumina, while the micron-sized Al and alane were considered to be 100% pure fuel. Figure 32 (a, b, and c) exhibit the results of the equilibrium calculations. The equivalence ratio, Φ, of the mixtures was held constant at 0.943. The baseline case considered contained 80-nm Al particles and frozen water (ice). A small addition of alane exerts a significant impact on the equilibrium flame temperature and product composition. The alanized fuel shows a 10 % increase in the specific impulse (∼ [T$_{prod}$/MW$_{prod}$]$^{0.5}$) and a 5 % reduction in the flame temperature relative to the baseline case. The former can be attributed to the substantial decrease in the overall molecular weight of the product species. Figure 32b shows that the addition of alane increases the mole fraction of hydrogen generated, while simultaneously reducing the mole fraction of alumina. Such a

reduction of alumina also mitigates the two-phase flow losses in the exhaust nozzle of a propulsion device. The fuel containing micron-sized Al exhibits a modest improvement in the specific impulse (~2%), which can be attributed to the reduction of inert alumina, when the nano-sized Al is replaced by the micron-sized Al. Figure 32c shows the flame temperatures and Isp for the baseline nano-Al/ice mixture compared to fuels containing 20% micron-sized Al or alane as a function of the equivalence ratio. Clearly, the alanized formulation leads to the highest performance, while maintaining the lowest flame temperature under most conditions. All three formulations demonstrate a temperature plateau under fuel rich conditions corresponding approximately to the melting temperature of aluminum oxide (~2,300 K). However, the highest temperature and Isp always occur near the stoichiometric condition.

(a)   (b)   (c)
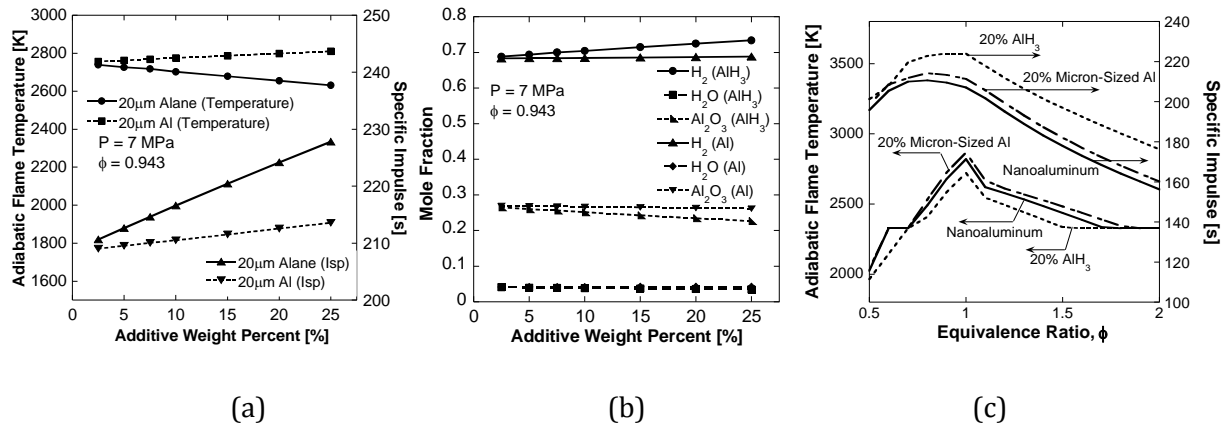
Figure 32: Adiabatic flame temperature, specific impulse, and product mole fraction as a function of fuel additive weight percentage.

Experimental Approach

The experimental study involves measurements of the linear burning rate and hydrogen yield over a range of pressures using a windowed constant-pressure strand burner and a constant-volume cell, respectively.

Sample Preparation

The reactive mixtures under investigation were comprised of 80-nm (procured from Nanotechnologies, Inc.), 20-µm Al particles (Sigma Aldrich), and 20-µm Al hydride particles combined with de-ionized distilled water. The 80-nm "as received" nano particles were passivated for 96 to 120 hours in air, reducing the active Al content from 77 -79% to ~ 74.5%, to prevent the occurrence of low-temperature reactions [13]. Both the alane and micron Al particles were assumed to be 100% active, since the alumina content of the 20-µm Al is small and the alane is believed to be absent of any oxide. De-ionized water was purchased from Electron Microscopy Sciences (Reagent A.C.S Cat#22800-01), reporting a maximum of 0.01 ppm silicate, 0.01 ppm heavy metals, and 10 ppm of residue (after removal from packaging, due to evaporation). Proper amounts of 80-nm Al particles combined with either 20-µm Al or alane particles were premixed using a Resodyne LabRAM® acoustic mixer to break up agglomerates (as discussed previously) and

produce a homogenous fuel composition prior to oxidizer addition. The mixture was filled into quartz sample tubes (10-mm OD, 8-mm ID) and then frozen at -35ºC. Recorded packing densities for the 100% 80-nm composition with Φ = 0.943 were 1.60±0.03 g/cm^3, while increasing the mass fractions of 20-µm Al and alane particles showed decreasing packing densities, ranging from 1.51±0.03 g/cm^3 for 25% 20-µm Al particle addition and 1.44 ± 0.03 g/cm^3 for 25% alane particle addition.

Particle Characterization and Thermal Analysis

High resolution scanning electron microscopy (SEM) images of the fuel particles are shown in Figure 33. The 80-nm Al particles exhibit spherical characteristics in contrast to the rhombohedral-shaped alane. The 20-µm Al particles have a wider particle distribution compared to the other particles. Thermo-gravimetric analysis (TGA) and differential scanning calorimetry (DSC) experiments were performed on separate samples of alane and Al particles, as well as mixtures of the particles, to quantify the low temperature thermal characteristics in an argon atmosphere with trace amounts of oxygen. The TGA/DSC results (Figure 34) indicate that the alane powder begins decomposition at approximately 150 ºC, which is consistent with published data [33,34,36]. Furthermore, the mass lost during the process showed a 9.6% reduction, accounting for the hydrogen lost, which is close to the theoretical hydrogen mass content of 10.1%. Further heating of the alane (or Al) particle exhibited an endotherm in the DSC profile at approximately 660 ºC indicating melting of the Al.

(a) 80-nm aluminum   (b) 20-µm aluminum   (c) 20-µm Alane
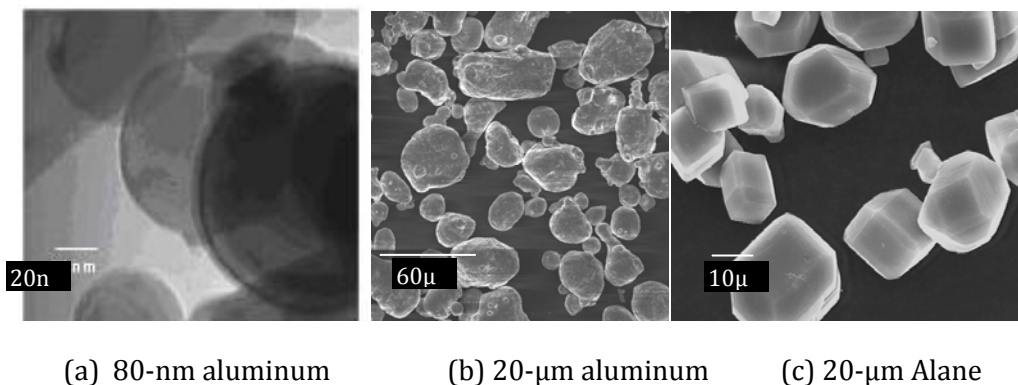
Figure 33: (a) TEM and (b and c) SEM images of particles considered [20].
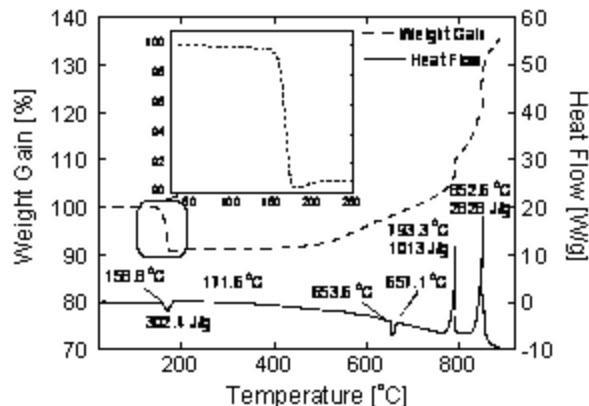
Figure 34: TGA and DSC results of neat alane in an argon (with trace amounts of oxygen) atmosphere.

Combustion Experiments

Strand burner experiments were conducted at nearly constant pressure to obtain linear and mass burning rates of various reactive mixtures, as functions of both pressure and mixture composition. Details of the system specifications and ignition procedures can be found in Refs. [12,13]. Argon gas was used as a pressurant to achieve the desired chamber pressure. Sample ignition was achieved via a 28 gauge nichrome hot-wire and NOSOL 363 (classical double based gun propellant) booster charge. The chamber operating pressures ranged between 0.86 and 15 MPa (125 to 2,175 psia). A Setra pressure transducer provided static monitoring of the chamber pressure, and the pressure data were recorded at 500 Hz. The combustion event was photographically recorded using a Sony digital video camera. The linear burning rate was correlated using a conventional Saint Robert's power law fit, which is given as,

$$r_b \text{ [cm/s]} = A(P[MPa])^n$$

where A is a constant pre-exponential coefficient and n is the pressure exponent [30].

Constant-volume chemical efficiency [27] was measured using a 181 cm^3 constant-volume vessel, to determine the effects of pressure and mixture composition on the hydrogen yield. The operational pressure ranged up to 69 MPa (10,015 psia). Quartz tubes (3.2 cm x 1 cm) containing ~ 2 grams of reactive mixture (Φ = 0.943) were placed onto a carriage and positioned into the center of the vessel. Argon gas was flowed into the chamber, allowing continuous flushing of the gas in the chamber and purging of the entrapped air, until the required initial pressure was achieved. Ignition was achieved via a coiled 28 gauge nichrome filament (without the NOSOL booster) embedded into the reactive mixture surface prior to freezing. The output signals from the dynamic pressure transducer were recorded at 5 kHz during the experiment. After completion of the burning, the trapped gas products in the chamber were sampled using a calibrated gas chromatograph (Agilent 3000 Micro GC) at 153 kPa (22.2 psia) to determine the concentration of molecular hydrogen. The chemical efficiency was obtained by relating the measured hydrogen concentration to the theoretical maximum value based on the stoichiometry and reactant composition.

Results and Discussion

Figure 35 shows the linear burning rate of the reactive mixtures as a function of additive weight percent at a nominal pressure of 7 MPa. Mixtures consisting of nano and micron-sized Al particles have a relatively constant burning rate ($\sim$ 2.8 cm/s) over the range of conditions tested. Connell *et al*. [45] have shown that the linear burning rate (at 7 MPa) held approximately constant for up to 40% addition of 2-μm aluminum particles and 20% for 5-μm particles, beyond which the linear burning rates began to decrease. In contrast, the burning rate of a mixture containing alane particles decreased from 2.6 to 1 cm/s as the amount of alane increased. This phenomenon can be attributed to the lower flame temperature caused by the endothermic decomposition of alane.
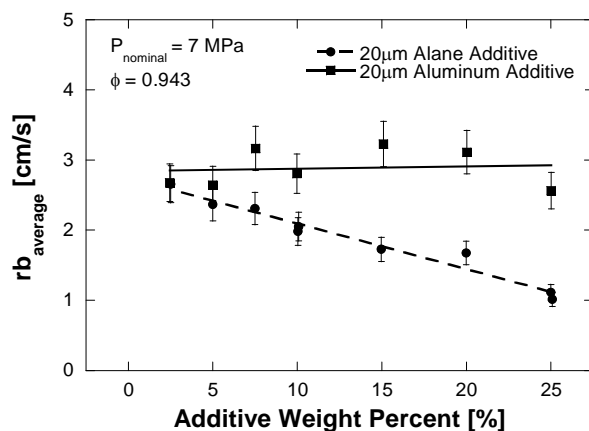
Figure 35: Effect of additive weight percentage on linear burning rate at a nominal pressure of 7 MPa.

The effect of pressure on the burning rate is given in Figure 36 a and b. For all the cases considered here, the burning rate increases with increasing pressure. However, the situation is reversed with alane concentration. The addition of alane particles reduce the burning rate, while 20 μm Al compositions (with the same weight percentages) are similar to the 80-nm baseline, achieving a slightly faster burning rate for the highest pressure. A similar trend was found by Connell *et al*. [45] using 2 μm versus 20 μm Al particles. Although ignition of the mixture with 75% 80-nm Al and 25% alane was achieved at 3.55 MPa (515 psia), the burning rate could not be attained due to the diminished luminosity of the combustion front. The low luminosity is another indication of decreasing reaction temperatures with alane addition. The respective parameters in the Saint Robert's burning law for each formulation are provided in the figures.
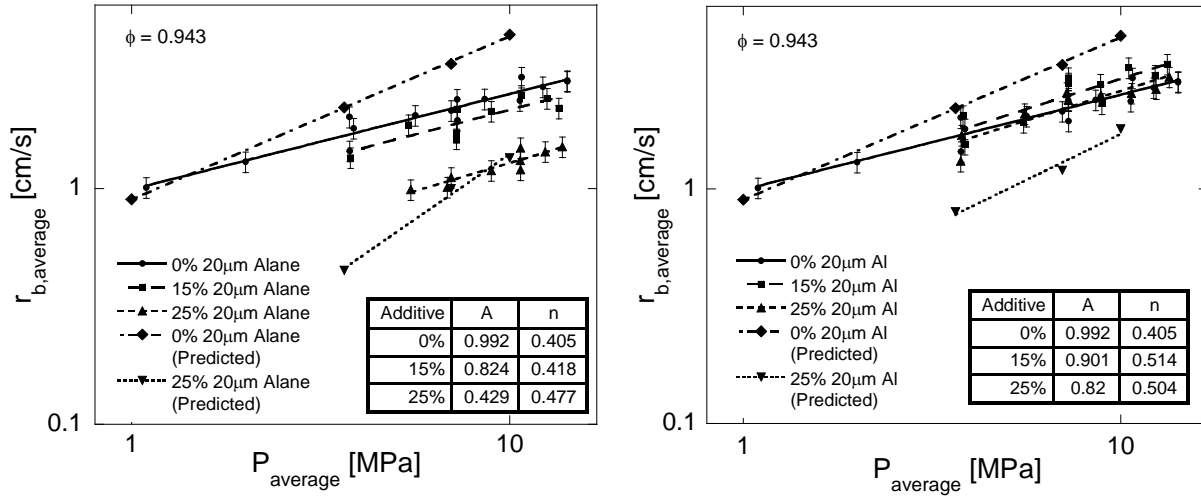
Figure 36: Linear regression rate results for mixtures containing: (a) alane and (b) 20-μm Al.

Constant pressure efficiency tests were conducted by varying the additive weight percentage at a nominal pressure of 7 MPa (Figure 37). The average chemical efficiency for the baseline propellant was ~ 72%. Chemical efficiencies of approximately 80% were presented by Risha et al. [10] for a similar 80-nm aluminum and water composition, over a similar range of pressures. The combustion efficiency for the frozen baseline composition should be slightly lower due to additional loss associated with the phase change from ice to water. The bimodal propellant compositions with either alane or micron-sized Al showed a slight increase in chemical efficiency compared to the baseline results. The results, however, remained approximately constant with increasing additive substitution. Efficiencies for the 80-nm and 20-μm Al cases appear to be slightly higher than those with similar compositions containing alane particles. In the constant volume experiments, the pressure increase (ΔP) during reaction for alane-loaded mixtures decreased from 5.5 to 4 MPa with increasing particle addition, while the pressure generated by the micron-sized Al composition was approximately constant (5.3-5.5 MPa).
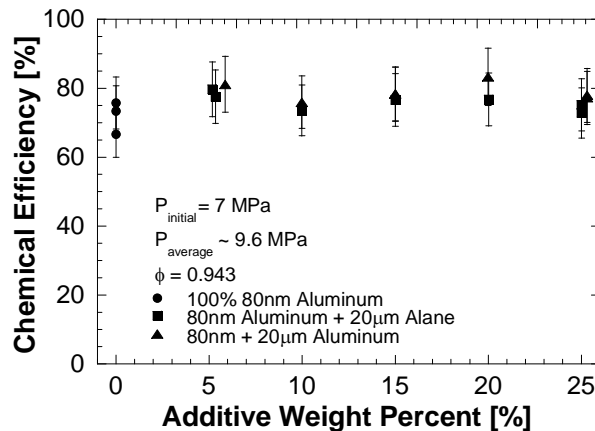
Figure 37: Chemical efficiencies of various mixtures at an initial pressure of 7 MPa.

51

Figure 38 shows the chemical efficiency for various initial pressures using the same mixture formulations as those in the strand burner experiments. The efficiency for the baseline mixture increased from 63% to 80%, when the pressure increased from 3.55 to 10.4 MPa (515 to 1,515 psia). Increases in efficiency for bimodal compositions are also shown, with the most significant being with the 15% and 25% alane compositions, which increase from 60% and 32% respectively to ~ 80% at the highest pressure. The efficiencies for 80-nm and 20-μm Al particles were slightly elevated from the baseline, following a similar, linearly increasing trend. Connell *et al.* [45] indicated that with increasing active Al content, the reaction temperature increases, due to a reduced initial alumina concentration. Both the increased equivalence ratio and reduced alumina concentration resulted in a higher adiabatic combustion temperature, promoting formation of molten alumina and improving the reactivity of the composite fuel. The burning rate and chemical efficiency thus increased accordingly.
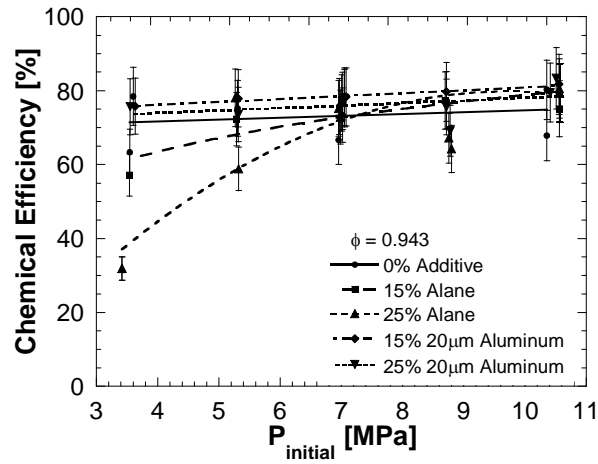
Figure 38: Chemical efficiencies for various mixtures and different initial pressures.

As shown in Figure 36, the burning rates of the bimodal aluminum mixtures are consistent with the baseline, with 15% 20 micron composition increasing from approximately 3% to 16% (0.05 to 0.5 cm/s) above the baseline, and the 25% 20 micron formulation lying directly on the baseline over the range of pressures tested. Burning rates of alane compositions are shown to decrease up to ~ 50% compared to the baseline with increasing alane weight percentage. This is not surprising considering that nano particles burn relatively faster than micron-sized particles and the adiabatic flame temperature decreases with the addition of alane. The higher flame temperatures of aluminum/ice mixtures help explain the observed decrease in the burning rate associated with the alanized formulation. Since the burning rate is dictated by the heat transfer from the flame zone to the condensed phase, such a lower flame temperature of the alanized composition contributes to the reduction in the burning rate. This behavior is consistent with the experimental observation in which the burning rate decreases with increasing alane content, whereas it remains nearly constant or even increases slightly with micron-sized aluminum. The theoretical results show reasonably good agreement with the experimental data. The treatment of multi-phase flow is simplified by employing a mixture model and assuming equilibrium between different phases. In addition, radiation heat transfer is neglected in the present analysis. Furthermore, accurate burning time data are not available for single nAl particles burning in liquid

water environment at high pressures. These assumptions are believed to be reasons for the disparity between experimental measurements and numerical predictions. Further improvement is warranted.

Theoretical Analysis of Combustion of Aluminum, Aluminum Hydride, and Water/Ice Mixtures

Aluminum (Al)-water mixture has been proposed as a propellant for both space and underwater propulsions [46,47]. In addition to its high energy release rate, the propellant combination and its combustion products are non-toxic [46]. The combustion of Al-H_2O system is also of interest to underwater propulsion, since water need not be carried onboard [48]. Recently, Al-H_2O mixtures have been identified as a novel chemical mixture for hydrogen generation [49]. Nano-sized particles have higher reaction rates than micron-sized particles [50], as nano-particles have shorter burning times and lower ignition temperatures [51]. Thus, nAl-H_2O system has been studied with considerable interest in the recent past.

In the recent past, considerable experimental efforts have been made to investigate the combustion of nAl-H_2O mixtures with water in both liquid and frozen phases [52-55]. The burning rates and the conversion efficiencies have been measured for a wide range of equivalence ratios, particle sizes, and pressures. The burning rates of nAl-liquid water mixtures are characterized by a pressure exponent of 0.47 and a d^{-1} law. The observed dependence of burning rates on pressure and particle size has not been well understood. In addition, a significant portion of nAl particles is made of alumina. For example, a 38 nm Al particle contains about 45.7 wt. % of alumina (Al_2O_3). Consequently, novel methods are necessary to increase the hydrogen yield of these mixtures. These include replacing a portion of nAl particles with micron-sized Al particles or by introducing hydrogen rich aluminum hydride (alane) particles. Micron-sized Al particles typically contain less than 1 wt. % Al_2O_3. Alane, is used in many energetic materials due to its high hydrogen storage capacity ($\sim$10.1 wt. %) [56]. Bazyn et al. [57] determined that the alane particles, upon dehydrogenation, burn like Al particles with similar burning times. Recently, Connell et al. [58] studied the effect of replacing a portion of 80 nm Al particles with micron-sized Al particles on the burning rates of the stoichiometric mixtures. The linear burning rate was not noticeably affected, until the micron-sized particle substitution exceeded 20% of the active fuel mass.

In order to explore and understand the combustion characteristics of nAl-H_2O mixtures and also to determine the effect of replacing a portion of nAl particles in the mixture with micron-sized alane and Al particles on the combustion of nAl-H_2O mixtures, theoretical studies would be very useful. In the past, theoretical studies on nAl-H_2O mixtures have not been attempted. The present work extends the previous model [59] to handle the prevalence of oxidizer in the condensed phase. The focus is to establish a multi-zone theoretical framework and to determine the flame temperature, flame speed, and flame thickness of these mixtures.

Theoretical Framework

Steady-state and one-dimensional planar flame propagation is considered. The major assumptions and approximations in the present analysis are: (1) the particles are assumed to be uniformly sized; (2) collisions and interactions between the particles are neglected; (3) gravitational effects and radiation heat transfer are neglected; (4) the particle is assumed to be in equilibrium with the gas. The entire region of interest is divided into six zones: (1) nAl-AlH₃-H₂O$_{(s)}$ preheat zone (I); (2) nAl-AlH₃-H₂O$_{(l)}$ preheat zone (II); (3) nAl-AlH₃-H₂O$_{(g)}$ preheat zone (III); (4) Al-H₂-H₂O$_{(g)}$ preheat zone (IV); (5) nAl reaction zone (V); (6) µAl reaction zone (VI), as shown in Figure 39. Phase transitions of the oxidizer and the dehydrogenation of alane particles are assumed to happen in an infinitesimally thin sheet. The multi-zone framework can be used to study a variety of mixtures by the appropriate modification of the treatment of the preheat zones and the reaction zones. For example, for mono-dispersed nAl-liquid water system, only two preheat zones and a single reaction zone are present.
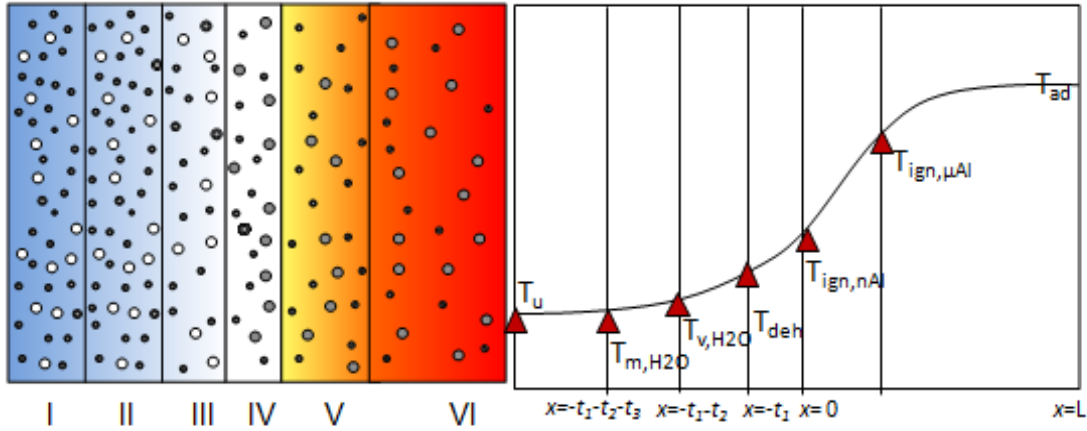
Figure 39: Physical model and multi-zone framework (large white circle – alane, small grey circle – nAl, large grey circle - µAl).

The nAl particles react heterogeneously and heat the mixture to the ignition temperature of micron-sized Al particle. Subsequently, the micron-sized Al particles react and heat the mixture to the adiabatic flame temperature of the mixture. The governing equations and the boundary conditions are given below:

nAl-AlH₃-H₂O$_{(s)}$ preheat zone (I):

The mixture in this zone consists of oxide coated nAl particles, alane particles, and ice. Steady-state energy conservation of the mixture is considered:

$$\rho_0 U_0 C_{p1} \frac{dT}{dx} = \lambda_1 \frac{d^2T}{dx^2};$$

(1)

$$\begin{cases} x \to -\infty : T \to T_u, \\ x = -(t_1 + t_2 + t_3) : T = T_{m,H_2O}. \end{cases}$$

54

The conservation of mass of the mixture ($\rho_0 U_0 = \rho_u S_L$) is used in constructing Eq. (1). The thicknesses of the preheat zones (t_i) and the flame speed are not known *a priori*.

nAl-AlH$_3$-H$_2$O$_{(l)}$ preheat zone (II):

The components of the mixture in this zone are nAl particles, alane particles, and liquid water. Ice is assumed to melt at the interface of zone I and II. The heat-flux balance at the interface incorporates the enthalpy of fusion of ice. The governing equations are given by:

$$\rho_0 U_0 C_{p2} \frac{dT}{dx} = \lambda_2 \frac{d^2T}{dx^2};$$

(2)

$$\begin{cases} x = -(t_1+t_2+t_3): \lambda_2 \frac{dT}{dx} = \lambda_1 \frac{dT}{dx} + \rho_{H_2O_{(s)}} S_L h_{s-l}, \\ x = -(t_1+t_2): T = T_{v,H_2O}. \end{cases}$$

For simplicity, it is assumed that the phase change of ice to liquid water does not affect the volume and the mass fractions of the components of the mixture.

nAl-AlH$_3$-H$_2$O$_{(g)}$ preheat zone (III):

The components of the mixture in this zone are nAl and alane particles and water vapor. Liquid water is assumed to vaporize at the interface of zone II and III. The heat-flux balance at the interface incorporates the enthalpy of vaporization of liquid water. The governing equations are given by:

$$\rho_0 U_0 C_{p3} \frac{dT}{dx} = \lambda_3 \frac{d^2T}{dx^2};$$

(3)

$$\begin{cases} x = -(t_1+t_2): \lambda_3 \frac{dT}{dx} = \lambda_2 \frac{dT}{dx} + \rho_{H_2O_{(l)}} S_L h_{f-g}, \\ x = -t_1: T = T_{deh}. \end{cases}$$

For pressures of interest in this study, the dehydrogenation temperature of alane is taken to be 800 K [60]. The particles are assumed to follow the carrier fluid, in view of the low momentum relaxation time. Hence, a single velocity field is used in the analysis.

Al-H$_2$-H$_2$O$_{(g)}$ preheat zone (IV):

The mixture in this zone is made of of Al particles, water vapor, and hydrogen gas. The governing equations are given by:

$$\rho_0 U_0 C_{p4} \frac{dT}{dx} = \lambda_4 \frac{d^2T}{dx^2};$$

(4)

$$\begin{cases} x = -t_1 : \lambda_4 \dfrac{dT}{dx} = \lambda_3 \dfrac{dT}{dx} + \rho_{AlH_3} U h_{deh}, \\ x = 0 : T = T_{ign,1}. \end{cases}$$

The alane particles are assumed to dehydrogenate to yield Al particles and hydrogen gas following the endothermic reaction, R1. The enthalpy of dehydrogenation of alane is taken as 11.29 kJ/mol [61]. The mass fractions of Al and H_2 resulting from alane are also calculated from R1.

$$AlH_3 \rightarrow Al + 1.5H_2 \tag{R1}$$

Reaction zones (V,VI):

The nano and micron-sized Al particles burn in water vapor environment to yield Al_2O_3 and H_2. The global chemical reaction, R2, is used to compute the mass fractions of Al_2O_3 and H_2:

$$2Al + 3H_2O \rightarrow Al_2O_3 + 3H_2 \tag{R2}$$

The change in the volume fractions of the species are neglected. The mixture energy equation and the particle mass consumption equation are considered:

$$\rho_0 U_0 C_{p5} \frac{dT}{dx} = \lambda_5 \frac{d^2 T}{dx^2} - \frac{B_{u,1} Q}{\tau_{b,1}} - \eta \frac{B_{u,2} Q}{\tau_{b,2}}, \tag{5}$$

$$\frac{DM_{p,i}}{Dt} = -\frac{M_{p0,i}}{\tau_{b0,i}}. \tag{6}$$

In the energy equation, two heat source terms are related to the combustion of nano and micron-sized Al particles, respectively. As a result, two particle mass consumption equations are solved. An average particle mass consumption rate is employed. The mass consumption rate is the initial particle mass divided by the burning time calculated based on its initial particle size and at the local temperature. Here, the subscript i refers to the particle class (i=1,2 for nano-sized and micron-sized particles, respectively). Eq. (6) can further be simplified, since steady-state burning rates are desired. Multiplying Eq. (6) by ρU, and rearranging the result, we obtain:

$$\frac{d\left(d_{p,i}^3\right)}{dx} = -\frac{d_{p0,i}^3}{U.\tau_{b0,i}}. \tag{7}$$

To facilitate the analysis in the reaction zone, the temperature, particle size, and the spatial coordinate are normalized as follows:

$$\theta = \frac{T}{T_u}, \qquad \chi_i = \frac{d_{p,i}}{d_{p0,i}}, \qquad y = \frac{x'}{U_0 \tau_0}, \tag{8}$$

where x′ is a density-weighted coordinate, $x' = \int_0^x (\rho/\rho_0)\, dx$, and τ_0 is a reference burning time. The equations in terms of the normalized variables are given by Eqs. (9,10):

$$\frac{d^2\theta}{dy^2} - \kappa^2 \zeta \frac{d\theta}{dy} = -\mu_1 \kappa^2 \zeta^2 \left(\theta_{ign,1} - 1\right) \frac{\tau_0}{\tau_{b,1}} - \eta \mu_2 \kappa^2 \zeta^2 \left(\theta_{ign,2} - 1\right) \frac{\tau_0}{\tau_{b,2}};$$

$$\begin{cases} y = 0: \theta = \theta_{ign,1},\ \lambda_5 \left.\dfrac{d\theta}{dy}\right|_{0+} = \lambda_4 \left.\dfrac{d\theta}{dy}\right|_{0-}, \\[2mm] y \to L: \dfrac{d\theta}{dy} \to 0. \end{cases} \tag{9}$$

$$\frac{d\chi_1}{dy} = -\frac{1}{3\chi_1^2} \frac{\tau_0}{\tau_{b,1}};$$

$$\frac{d\chi_2}{dy} = -\frac{\eta}{3\chi_2^2} \frac{\tau_0}{\tau_{b,2}};$$

$$\begin{cases} y = 0: \chi_i = 1, \\ y \to L: \chi_i \to 0. \end{cases} \tag{10}$$

The location $y = 0$ is defined as the ignition point of particles. The variable η is unity for temperatures higher than the ignition temperature of micron-sized particles, while it is zero at lower temperatures. The entire solution procedure begins with a guess value of the flame speed. The iteration technique is applied in the preheat zone to determine the thicknesses of the preheat zones and to determine the temperature gradient at the ignition point. With this input, the system of ODE's in reaction zone is solved until the boundary conditions are satisfied. The Rosenbrock method is employed in conjunction with shooting method to solve the system of ODEs. Newton-Raphson method is used for root-finding [62].

Properties of the mixture

The packing density of the mixture is primarily a function of equivalence ratio, particle size, and nano-particle loading. The packing density of stoichiometric bimodal Al-ice mixture is about 1.55 g/cm³, while the packing density of bimodal alane-Al-ice mixture is about 1.45 g/cm³. The volume and the mass fractions of the species in each zone are computed based on the packing density. The thermo-physical properties of the mixture are calculated as:

$$\rho_i = \sum_{\alpha_i} \Phi_{\alpha_i} \rho_{\alpha_i},$$

$$\lambda_i = \sum_{\alpha_i} \Phi_{\alpha_i} \lambda_{\alpha_i},$$

(11)

$$C_i = \sum_{\alpha_i} Y_{\alpha_i} C_{p,\alpha_i}.$$

The property of each species is evaluated at a mean temperature in each zone and at the relevant pressure. The density of solid species (e.g., Al, alane, Al_2O_3, and ice) is assumed constant, while the density of liquid water is assumed to be temperature dependent. The specific heats and the thermal conductivities of all the species (except water vapor) is assumed to be dependent on temperature only, while that of water vapor is assumed to be a function of both pressure and temperature. The vaporization temperature and the enthalpy of vaporization of liquid water are calculated at the relevant pressure.

Particle ignition temperature and burning time

The present model requires particle ignition temperature and burning time as inputs. The ignition temperature of 20 μm Al particle is taken as 1883 K, while the ignition temperature of 80 nm Al particle is taken as 1165 K [63]. The variation of ignition temperatures and burning times of Al particles are shown in Figure 40. The single particle burning time correlations for micron-
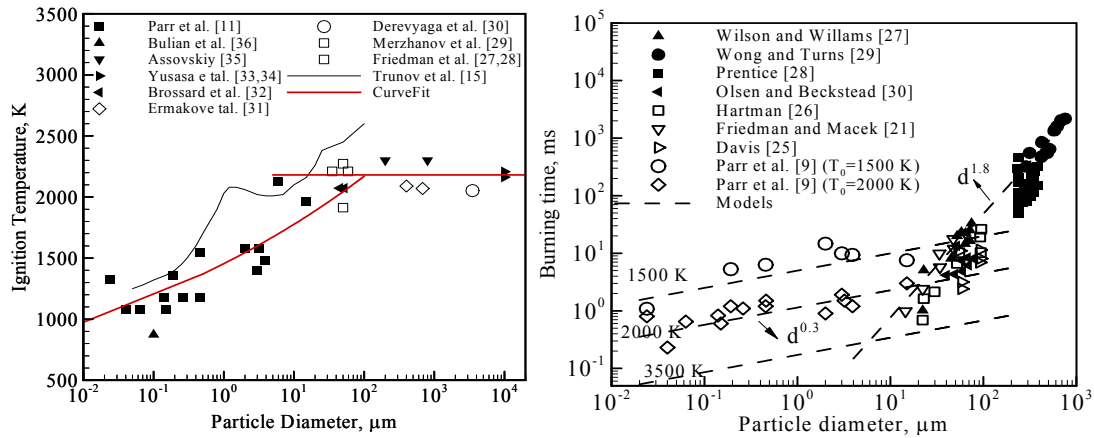
Figure 40: Ignition temperatures and burning times of Al particles.

sized and nano-sized Al particles are taken from Ref. [63], while the pressure exponent is taken as a function of ambient temperature [64]. As the combustion of nAl particles is controlled by the collision of water molecules on the particle surface [52], the burning times of ultra-small nAl particles are dependent on pressure. For micron-sized Al particles, as combustion is diffusion-controlled, a pressure exponent of 0.1 is widely accepted [65].

Results and Discussion

The effect of pressure on the temperature profiles and the normalized particle mass consumption rates of nAl-liquid water mixtures are depicted in Figure 41. The flame temperatures, which are around 2300 K, do not significantly change with pressure. Furthermore, these are
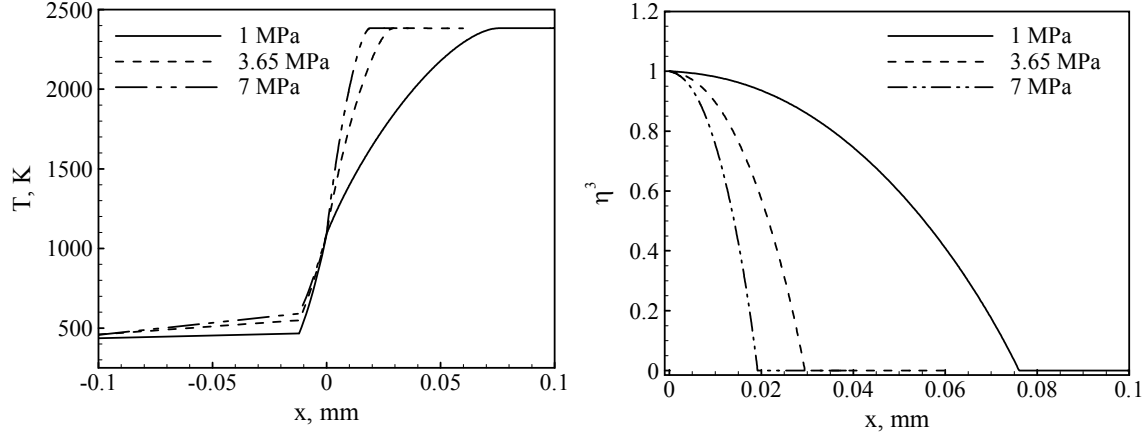
Figure 41: Profiles of temperature and normalized particle mass at $\Phi = 1$ and $d_p = 38$nm.

temperature and hence, the combustion is likely to be controlled by the collisions of water vapor molecules on the particle surface. The particle burn-out time decreases with increase in pressure. As a result, the flame thickness decreases from 0.16 mm to about 0.04 mm, as the pressure
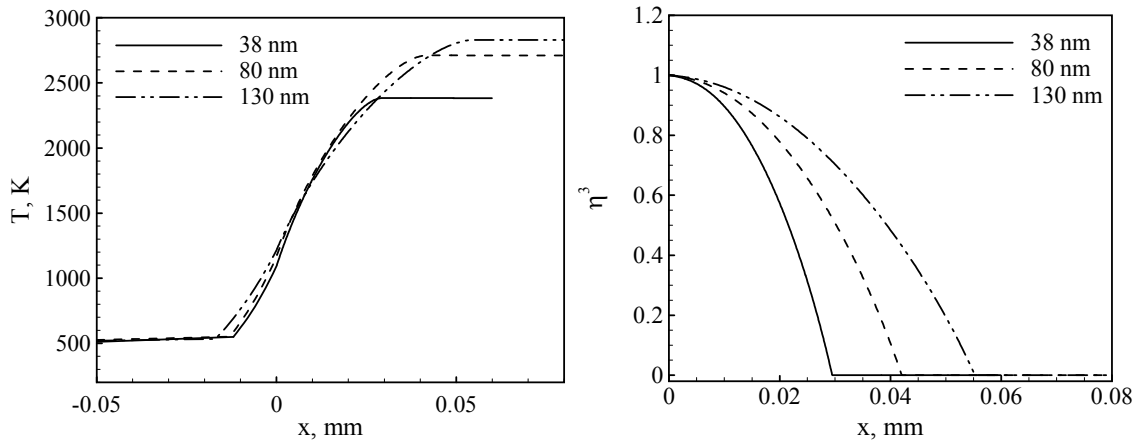
Figure 42: Profiles of temperature and normalized particle mass at $\Phi = 1$ and $p = 3.65$ MPa.

increases from 1 MPa to 7 MPa. A similar study is performed to ascertain the effect of particle size on the flame temperature and the flame thickness. The flame temperature increases by 500 K, as the particle size increases from 38 nm to 130 nm. This is caused by the decrease in the mass fraction of the oxide in the particle. Since, the burning times of nAl particles follow a $d^{0.3}$-law, the flame thickness increases from 0.06 mm to 0.21 mm, as the particle size increases from 38 nm to 130 nm. This is also clearly revealed by the normalized particle mass profiles in Figure 42. The dependence of flame speed on the equivalence ratio of nAl-liquid water mixture is shown in Figure 43. The flame speed increases by a factor of ~ 6, as the equivalence ratio increases from 0.5 to 1. This is due to the increase in the heat-release rate, caused by the availability of Al particles to react heterogeneously with the water vapor molecules. Although the rich mixtures are not as
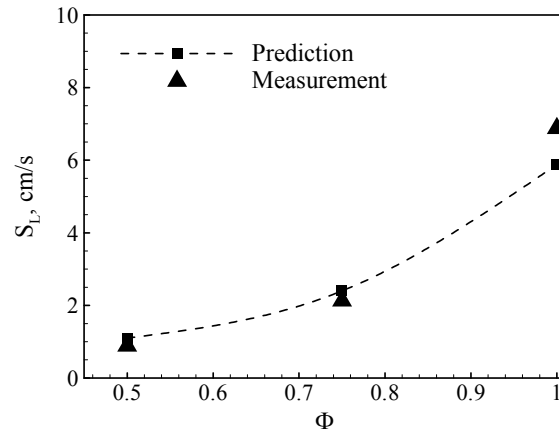
Figure 43: Variation of flame speed with equivalence ratio at p = 3.65 MPa and d p= 38nm.

efficiently packed as the lean mixtures, higher flame speeds are observed. Figure 44 shows the variation of the flame speed with the particle size. As the particle size increases from 38 nm to 80 nm, the flame speed decreases from ~ 6 cm/s to ~ 2.7 cm/s. This approximately corresponds to a d$^{-1.0}$ law. This is also supported by the experimentally measured burning rates. As the flame temperature increases with increase in the particle size, the lower flame speed for a larger
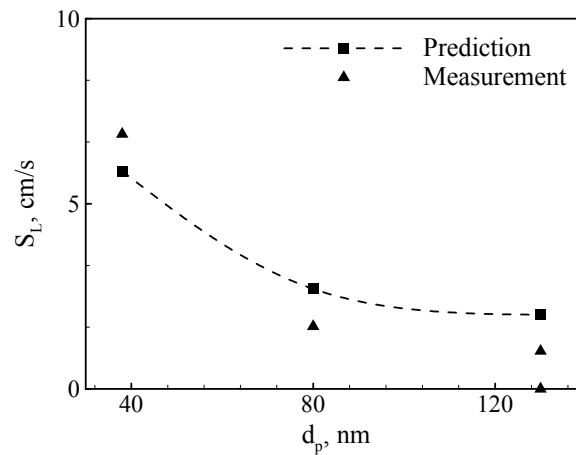
Figure 44: Variation of flame speed with particle size at Φ = 1 and p = 3.65 MPa.

particle is caused by the longer burning time. The variation of flame speed with pressure is shown in Figure 45. The experimental measurements indicate that the pressure exponent in the burning rate law is about 0.5. The pressure exponent predicted by the model is close to 0.7. Thus, the model slightly over predicts the dependence of burning rates on pressure. However, both the predictions and the experimental measurements reveal that the overall chemical reaction process is first order. This can be attributed to the fact that the dominant combustion mechanism

60
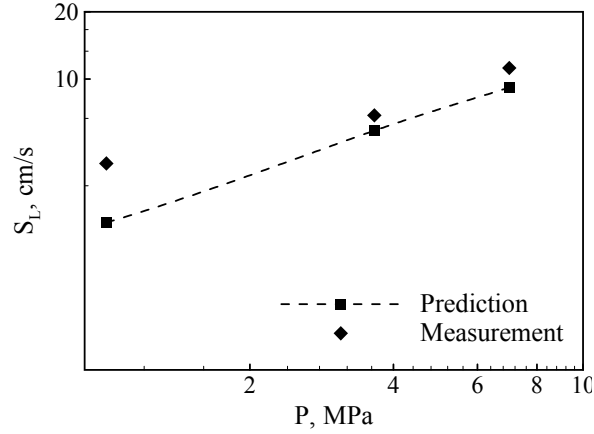
Figure 45: Variation of flame speed with pressure at Φ = 1 and dp = 38 nm.

is the collisions of water vapor molecules on the particle surface. As it has been emphasized earlier, the adiabatic flame temperature for stoichiometric 38 nm Al mixture is well below the Al vaporization temperature.

Hence, such an observation is not surprising. The model is then applied to study the combustion characteristics of bimodal Al/Alane-ice mixtures. The temperature profiles in the reaction zone for Al-ice mixtures at different pressures are shown in Figure 46. The flame temperatures of bi-modal Al-ice mixtures are consistently higher than those of mono-dispersed Al-ice mixtures.
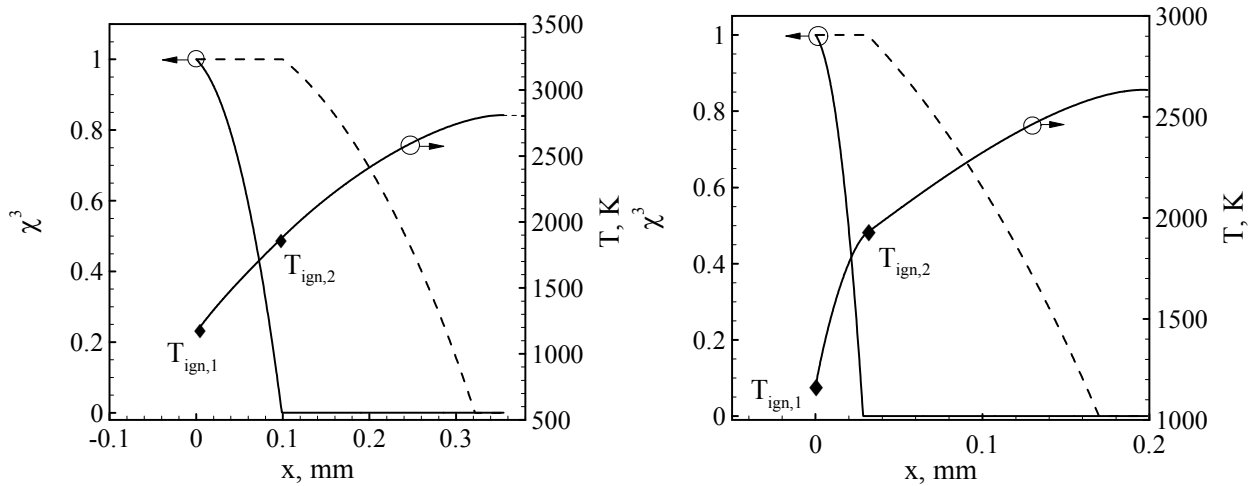
Figure 46: Temperature, particle mass consumption profiles of bimodal Al-ice mixtures at 1 MPa and 7 MPa.

This is due to the decrease in the mass fraction of the oxide in the mixture. The flame temperatures are close to 2700 K. For similar reasons, the estimated value is also higher than the flame temperature of stoichiometric 38 nm Al-ice mixtures at the same pressure. The thickness of the nAl reaction zone, at 1 MPa, is higher than that at 7 MPa. However, the thickness of μAl reaction zone is not significantly affected by the pressure. This is also clearly depicted by the particle mass consumption profiles in Figure 46. At higher pressures, the nAl particles are consumed quickly. This

61

is because the combustion of nAl particles is controlled by the collision of water molecules on the particle surface. However, for micron-sized Al particles, a diffusion-controlled combustion leads to a weak dependence of burning time on pressure. Nevertheless, the flame temperatures are not significantly affected by pressure. The temperature and the particle mass consumption profiles for Alane-Al-ice mixtures are shown in Figure 47.
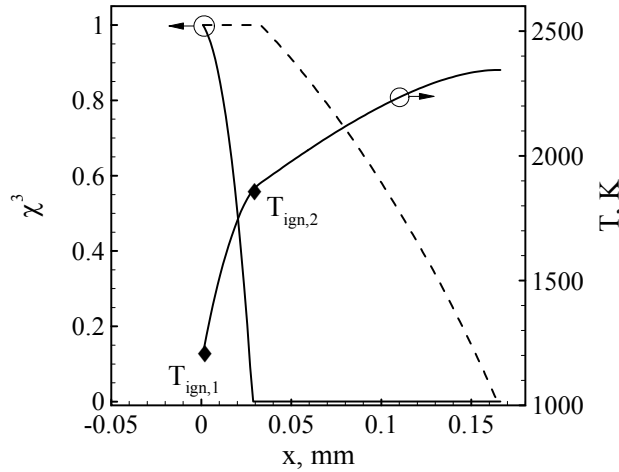
Figure 47: Temperature and particle mass consumption profiles of bimodal Al-Alane-ice mixtures at 7 MPa.

Clearly, the predicted flame temperature, at 7 MPa, is close to 2300 K. This is approximately equal to the flame temperature of stoichiometric 38 nm Al-ice mixtures at the same pressure. The lower flame temperatures of Alane-Al-ice mixtures are attributed to the endothermic dehydrogenation reaction of alane particles prior to their ignition. As it is expected, the thickness of nAl reaction zone is not affected. Since, the time-scales of combustion of alane particles are similar to those of Al particles, the total flame thickness is not significantly affected by the incorporation of micron-sized alane particles instead of micron-sized Al particles. These are also revealed by the particle mass consumption profiles. The flame thicknesses of all the mixtures studied are on the order of 0.1 mm. The model inherently assumes that the the micron-sized Al particles are ignited approximately when the µAl particles are completely burned. This is a reasonable approximation for stoichiometric mixtures with high nano-particle loading. As the nano-particle loading is reduced below 50 %, this approximation would not be valid, as the two reaction zones would be widely separated. This is also true for fuel-lean or fuel- rich mixtures. The variation of linear burning rates of bimodal Alane-Al-ice mixtures and bimodal Al-ice mixtures with pressure is shown in Figure 48. For the sake of comparison, the model is applied to study the flame propagation of mono-dispersed nAl-ice mixtures. The burning rates predicted by the model are reasonably in good agreement with the experimentally measured values. When 25 % of nAl particles is replaced with micron-sized Alane particles, a significant reduction in the burning rates is observed. The decrease in the burning rates is attributed to the lower flame temperatures of Alane-Al-ice mixtures and longer burning time of micron-sized Al particles. However, as it is expected, the pressure exponent in

the burning rate law is not significantly affected by the substitution. These trends are well supported by the experimental measurements. The model also predicts a noticeable reduction in the burning rates, when 25 % of nAl particles is replaced with μAl particles. The flame temperatures of the bi-modal mixtures are mildly higher than the flame temperatures of mono-dispersed mixtures. However, the burning times of micron-sized Al particles are significantly higher than the burning times of nAl particles. As a result, lower burning rates are predicted. However, the experiments indicate that the burning rate is only mildly reduced due to the substitution. A more complete treatment of multi-phase flow including the interaction between the particles and the flow, and accurate input of single particle burning time in liquid water at high pressures is expected to reduce the disparity between experimental and numerical results.
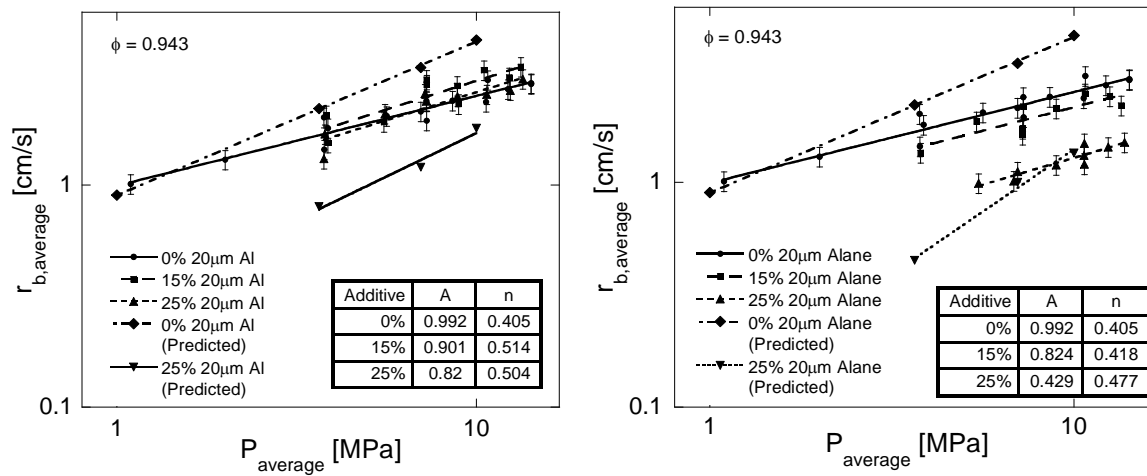
Figure 48: Variation of linear burning rate of bimodal Al-ice mixtues and Alane/Al-ice mixtures with pressure.

Internal Ballistic Model Development and Aluminum Ice Sounding Rocket

Aluminum and water propellants have shown promise in eliminating some of the disadvantages of AP-based propellants, yet present many challenges also. Theoretical calculations with aluminum-water mixtures by Ingenito et al. predict a vacuum specific impulse (Isp_{vac}) of over 300 s [66]. The aluminum and water propellant have an environmental benefit as well. Aluminum oxide (Al_2O_3 or alumina) and hydrogen gas are the major products of the combustion process, resulting in a more environmentally friendly propellant [67,68]. Freezing the aluminum-water propellant has been shown to prolong the life of the propellant, potentially eliminating aging issues [69]. Furthermore, aluminum and water propellants are theorized to be well-suited for deep space exploration because the propellant could potentially be formed in situ. Research has shown that the abundance of aluminum within the lunar crust is similar to that of earth and there is evidence that water exists on

the moon as well [70]. As a result of these findings, the possibility arises for aluminum and water propellants to be produced on the lunar surface, thus decreasing the take-off weight and greatly increasing the effective specific impulse of a mission. For example, calculations by Linne and Meyer show that the effective specific impulse for a mission can be doubled compared to that of an all Earth propellants mission if half of the propellant production is done in situ [71].

In this section we present recent results obtained with the ALICE propellant and derivative mixtures. First, ground test motor pressure and thrust data are evaluated against an internal ballistic model taking into account mass flow contributions from the igniter, combustion efficiencies, and specific impulse efficiencies. Second, we compare the trajectory simulation results for the flight of a sounding rocket with the data recorded by the on-board data acquisition system and derive approximate performance data for the flight.

ALICE Performance Prediction

Internal Ballistic Model Description

A lumped-parameter model was developed following the derivation by Heister [72] to determine the internal ballistics analysis of the combusting ALICE motor grains. The control volume considered in this model takes into account the geometry of the grains tested at the propulsion laboratory. While a simple approach, the assumptions inherent to a lumped-parameter model are quite appropriate in the present application as the grains tested had low aspect ratios L/D ranging from 1.2 for the 3.5" long grains to 2.3 for the 7" long grains and, therefore, the pressure variations along the chamber length can be neglected [72]. The assumed ALICE propellant formulation had an equivalence ratio of 0.75 and a characteristic velocity of 1333 m/s, based on CEA results [73]. Further, based on previous experimental results reported in the literature [74], a specific impulse of 210 s is assumed for the thrust calculations. Table 10 provides all the relevant input data for the following models.

Table 10: ALICE propellant properties used in the model

Property	Value
Isp	210 s
c^*	1333 m/s
γ	1.13
Burning Rate Coefficients	
a	0.57
n	0.70

The purpose of the code is to predict the peak chamber pressure and thrust produced by the ALICE grains and to indicate the history of both parameters based on the measured strand burning rate and the calculated geometry of the grain. While propellant and motor parameters are adjusted in the model, detailed accounting of potentially important two-phase flow losses or nozzle flow losses is not within the scope of the present study.

The results presented below include that of two variants of the model. The first model variant is described in details by Wood *et al.* [75]. In this variant, the ALICE propellant properties are assumed as nominal and the pressure and thrust contributions of the igniter are neglected in developing the profile traces. It is used to predict the maximum thrust and chamber pressure prior to experimental testing of a new grain or chamber geometry. In the second variant, the pressure and thrust contributions of the igniter are added to the performance of the ALICE motor. One of the goals of this model is to determine the burnout time of the igniter. The operating pressure of the ALICE chamber is larger than the nominal pressure of the igniter, so the igniter propellant has a shorter total burn time. The modeling equations are adjusted to account for two different propellants burning at the same time and chambers choking and unchoking at different times. Following an experimental timeline, the igniter burns by itself first while the gaseous products pressurize the main chamber. During this time, only the igniter nozzle is choked. After some time, the ALICE propellant is ignited and begins to burn. Soon after ignition of the ALICE grain, the increase in pressure in the combustion chamber chokes the main nozzle and unchokes the igniter nozzle.

The conservation of mass equation, accounting for the individual burning rates of the ALICE and igniter propellants, is provided by Eq. 12.

$$\dot{m}_{in} - \dot{m}_{out} = 0 = \left((r_b \rho_p A_b)_{Igniter} + (r_b \rho_p A_b)_{ALICE} \right) - P_c \frac{A_t}{c^*_{mix}} \tag{12}$$

The expression c^*_{mix} is equal to a weighted average of the respective values for c^* based on the amount of mass contribution of each propellant during that time step. Since the igniter has four individual grains that are placed together, the number of segments is also taken into account in determining the burning area as given by,

$$A_b = 2\pi R_i L + (\text{\# of Un} - \text{inhibited Sides})(\text{\# of Segments})\left(\frac{\pi}{4}(2R_o)^2 - \frac{\pi}{4}(2R_i)^2 \right), \tag{13}$$

Substituting the respective burning rate equations and rearranging the terms, Eq. **12** becomes,

$$\left((aP_c^n \rho_p A_b)_{Igniter} + (aP_c^n \rho_p A_b)_{ALICE} \right) = P_c \frac{A_t}{c^*_{mix}}. \tag{14}$$

Equation 14 cannot be solved directly for P_c. Instead, an iterative approach is taken to determine the value for chamber pressure, by matching the values of the inlet and outlet mass flow rates.

Output of the Model

The second variant of the prediction code accounts for the performance contributions of the igniter. The igniter geometric parameters are measured with a digital caliper (nozzle dimensions, grain size, etc.) and thrust data is available online [76]. Values for c^* and γ are estimated using typical AP composite values, determined from CEA [73]. Ballistic parameters were obtained from AeroTech and input into the code. However, the burning rate coefficients used did not yield pressure profiles that matched the data obtained from ThrustCurve.org [76]. Therefore, the ballistic parameters of the igniter were adjusted in order to match the ThrustCurve.org pressure profile.

The estimated chamber pressure is backed out using the thrust data, and values for the ballistic parameters are iterated upon until it agrees with the data. Figure 49 shows the agreement between the igniter data found online and the lumped parameter model, as well as a pressure profile using the AeroTech burning rate coefficients. The igniter data shown here corresponds to that of an AeroTech H180 commercial motor as selected for all tests of 7" long ALICE grains.
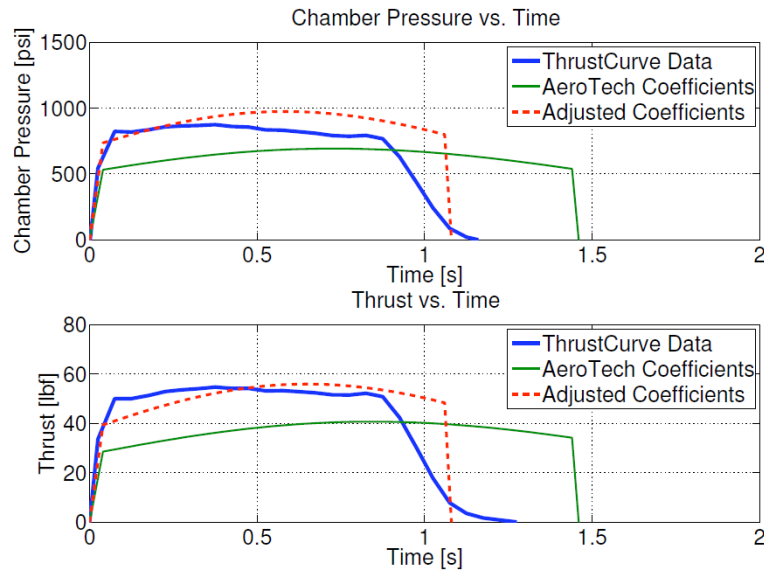
Figure 49: Lumped parameter model for the AeroTech H180 igniter compared to online thrust data and AeroTech coefficients.

Based on the data from the static test fires, it is estimated that the igniter is burning by itself for approximately 0.45 seconds before the ALICE motor ignites. With this empirical data point, the chamber pressure and thrust profiles calculated with both variants of the model can be plotted on a common graph as shown on Figure 50.

66
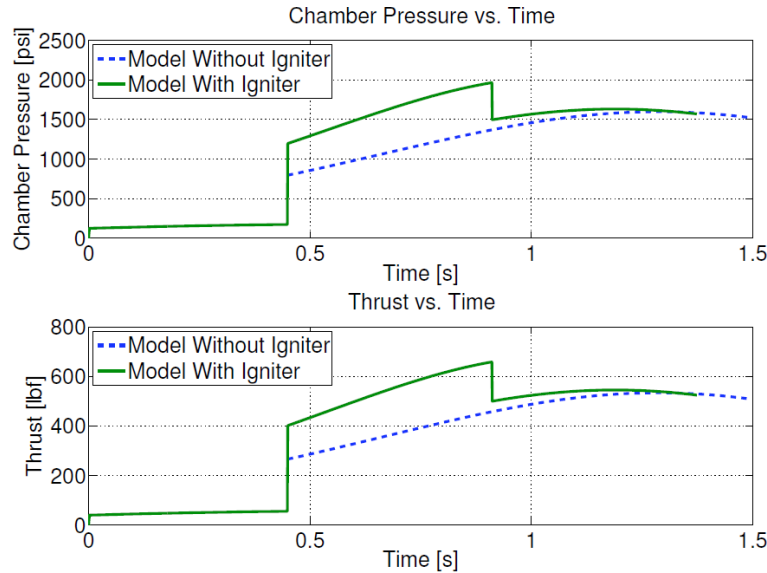
Figure 50: Calculated chamber pressure and thrust for 7" long ALICE grain.

Model Calibration

To increase the accuracy of the second model, two different conditions are employed after the static test is complete. Post-test analysis shows aluminum oxide agglomeration on the throat of the nozzle. The thickness of the agglomeration is measured and assumed to grow linearly with time. This throat deposit is input into the code. Secondly, a performance efficiency is added to the ballistic parameters; a $c*$ efficiency to the pressure trace, and an *Isp* efficiency to the thrust. This is applied by estimating the average $c*$ efficiency for the entire pressure rise. A linear efficiency is applied, using the time at the beginning of the ALICE burn and the time at the peak performance values and the average $c*$ to determine the slope. A different set of efficiencies are used for the pressure fall in order to better match the experimental data. These parameters are adjusted until the model agreed with the experimental results. A similar approach is taken to determine an *Isp* efficiency. Figure 51 shows two adjusted models for the 7" grains; one with a throat deposit included, and one without.

67
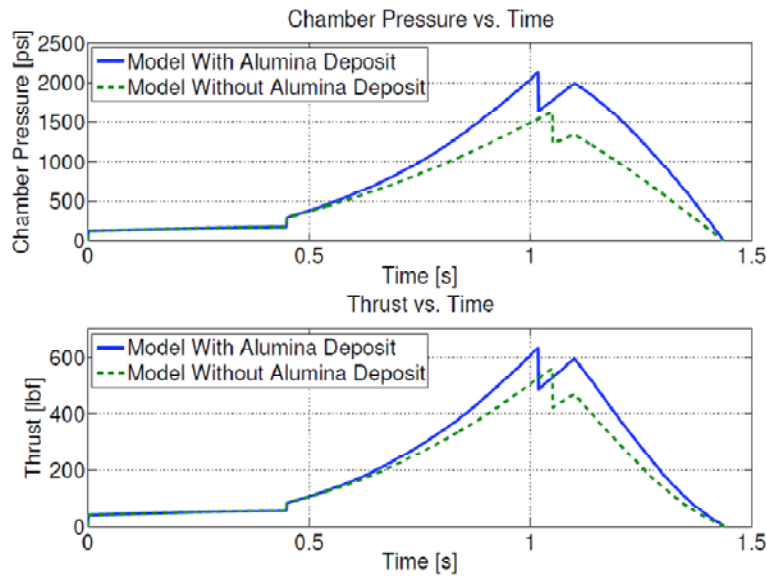
Figure 51: Comparison of models with and without alumina deposit.

Aluminum-Ice Sounding Rocket

Ground Testing

Horizontal Configuration

The first test of the flight-weight motor followed five successful tests with a heavy-wall combustion chamber designed for three inch diameter grains of increasing lengths (3, 5, and 7") [75]. Referred to as "Resodyn-6", the test was in the horizontal configuration. A nozzle throat of 0.52" was selected to provide a predicted chamber pressure of ~1500 psi. The first test used a grain length of 6.75", due to limitations of the grain-casting tool. A modification of the tool has been completed since the casting of the first grain to allow longer grains to be cast. The experimental results obtained with the first flight-weight grain are presented and compared with the modeling results in Figure 52. The test results show an average peak pressure around 1500 psi and a peak thrust of ~500 lb$_f$. The applied efficiencies are shown in Table 11.

68

Table 11: Applied efficiencies for computational model of Resodyn-6 test

Property	Value
Start Time	0.4 s
Peak Time	1.05 s
End Time	1.4 s
Average Rise c* Efficiency	45%
Peak c* Efficiency	65%
Average Fall c* Efficiency	35%
Average Rise *Isp* Efficiency	65%
Peak *Isp* Efficiency	95%
Average Fall *Isp* Efficiency	60%
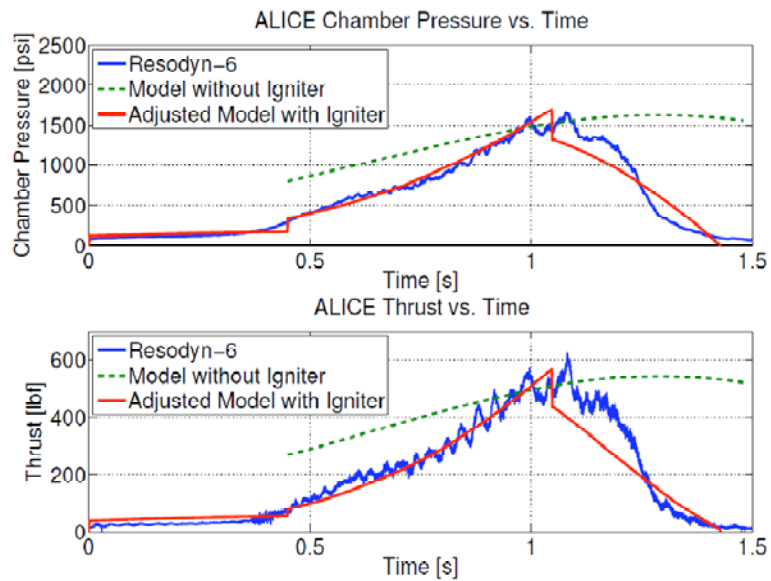
Figure 52: Comparison of 6.75" long ALICE motor test with lumped parameter models in the horizontal configuration.

69

Vertical Configuration

A vertical static fire tests was conducted with flight-weight hardware prior to launch with an ALICE motor. Since all previous tests were performed horizontally, knowledge of how the grain and alumina slag behaved with the effects of gravity was not known. These concerns ranged from questions on whether the grain would become dislodged from the walls of the phenolic tube and slide toward the nozzle, or if the alumina slag would clog the nozzle. This vertical test was conducted using the same AeroTech H180 igniter as in prior tests. The grain was slightly longer, from 6.75" to 7", compared to the previous horizontal test but with a nearly identical packing density (within 2.2%). Figure 53 displays the experimental data of the vertical test and the predictions obtained with the performance prediction model and Table 12 displays the efficiencies applied to the computational model in order to match the vertical flight-weight experimental data.

Table 12: Applied efficiencies for computational model of Resodyn-7 Test

Property	Value
Start Time	0.4 s
Peak Time	1.1 s
End Time	1.4 s
Average Rise c^* Efficiency	50%
Peak c^* Efficiency	75%
Average Fall c^* Efficiency	35%
Average Rise Isp Efficiency	70%
Peak Isp Efficiency	100%
Average Fall Isp Efficiency	60%
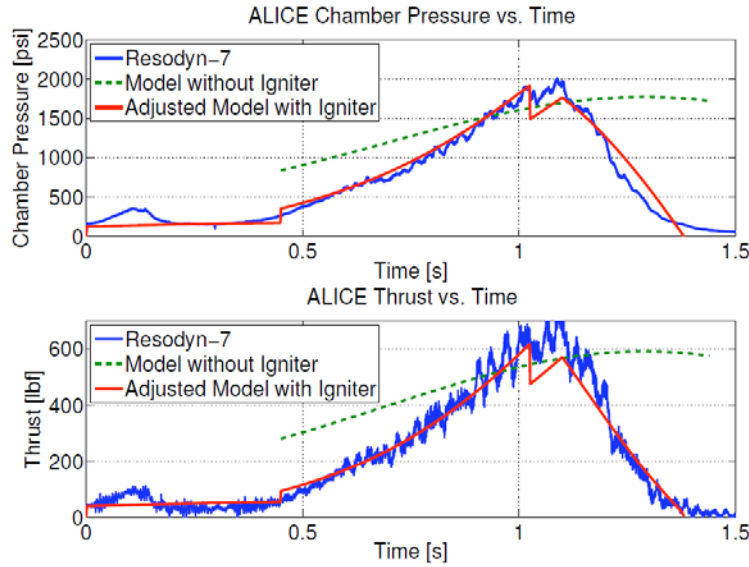
Figure 53; Comparison of 7" long ALICE motor test with lumped parameter model in vertical configuration.

It is encouraging that the lumped parameter models capture the experimental peak values of pressure and thrust for both the 5" and 7" grains. Despite the simplifying assumptions in the model, capturing these performance metrics provides an indication of an attainable *Isp* of ~214 s and a *c** of ~1330 m/s. Table 13 shows the average rise and peak efficiencies used in order to match the pressure and thrust profiles obtained with the flight weight motor tests. Improved propellant formulations with higher equivalence ratio (closer to stoichiometric) and appropriate additives should increase the experimental specific impulse to values well above 200 s.

Table 13: Applied Efficiencies to Match Experimental Data

Test	Average c*	Peak c*	Average Isp	Peak Isp
Resodyn–6	45%	65%	65%	95%
Resodyn–7	50%	75%	70%	100%

ALICE Launch

The demonstration flight of the ALICE propellant with an unguided experimental rocket was a proof of concept for more advanced rockets using similar nano-energetic material based propellants. The flight followed a rigorous design process and extensive ground testing of the ALICE rocket motor thus minimizing the likelihood of ignition issues or motor structural failure.

The experimental rocket chosen for the flight is an all-carbon-fiber, minimum diameter, 98 mm high power rocketry kit known as a Mongoose 98. Two launches were performed with this rocket; the first flight used a K-780 commercially available rocket motor to test the avionics bay and deployment of the parachutes and the second used the flight-weight motor casing with an ALICE

propellant grain. All launch operations were carried out at a remote area located approximately 12 miles south-west of West Lafayette. Known as Scholer Farm, this land is owned by Purdue and managed by the Animal Sciences Research and Education Center (ASREC). The first flight, with the K780 commercial motor, took place on June 14th, 2009. This flight is described in details by Wood et al. [75] along with a description of the flight weight motor casing design and implementation in the Mongoose 98. The demonstration flight of the ALICE propellant took place approximately two months later on August 7th, 2009.

For both test flights, we used a commercial ballistic trajectory simulation code (Rocsim-PRO) to calculate flight-vehicle performance (altitude, range, velocity, acceleration). This code simulates flight with the addition of wind speed and direction, atmospheric thermal gradients, pressure, location latitude/longitude, launch rail azimuth/elevation, and more. In addition it incorporates the NASA SPLASH code in order to perform 6-DOF Monte-Carlo simulations based on the uncertainty values in physical parameters such as mass properties (moment of inertia, center-of-gravity), aerodynamics (drag coefficient, center-of-pressure, fin cant angle), propulsion (total impulse, propellant mass, thrust axis), wind direction/velocity, and launch guide angle uncertainties.

Based on the thrust profile from the hot-fire test performed with the 7" long ALICE grain, as well as the new flight-weight motor design, the Rocsim-PRO simulations predicted that the 30 lb flight vehicle would depart the launch rail in 0.9 seconds, achieving a velocity of 67 ft/s at rail exit. The simulations also predicted a maximum acceleration of 16 G's, maximum velocity of 187 mph (Mach 0.24), and a nominal altitude of 1,200 ft under no wind conditions.

Several constraints limited the achievable altitude with the current ALICE powered rocket. First, the combustion and flow losses observed during the last six static test firings lead to total impulse values of about 60% that of the predicted values. These losses are being addressed in on-going work with improved propellant formulations including additives and alternative formulations to achieve higher specific impulse and lower the alumina content of the products. Second, the flight-weight casing for the ALICE propellant had to sustain pressures up to 2000 psi requiring thicker walls, thus increasing vehicle weight compared to a traditional SRM. In addition, the energy required for igniting the current ALICE propellant formulation is significantly higher than that required for a standard solid propellant. This leads to added weight for an igniter casing and an interface with the ALICE casing capable of sustaining high pressures and designed in such a way that the combustion gases do not impact the aluminum walls. Weights were also added just below the nose cone to yield a higher stability margin. While designed for flight with safety factors around 1.5, the heavier casing reduced the maximum altitude achievable with the rocket. Finally, the burning rate of the current ALICE formulation is on the order of 1 inch per second at the nominal operating pressure of 1500 psi. This high burning rate means that a larger web thickness is required to sustain the ALICE combustion over sufficiently long durations. In turn, larger grains require heavier casings. The current design is a trade-off between the aforementioned constraints. Further improvements of the propellant formulation should address these constraints, thus reducing the weight of the flight-weight casing in an effort to achieve better flight performance.

The ALICE demonstration flight took place of a fairly cool (~70°F ambient temperature) and calm (~2 mph wind at launch site) day. Figure 54 shows the ALICE vehicle on the stand ready for

takeoff (left), soon after ignition (middle), and flying under ALICE soon after it cleared the launch tower (right).

Figure 54: Images from the ALICE flight test: Rocket on launch platform (left), ignition of the ALICE propellant (middle), and rocket in flight (right).

The rocket coasted after the grain was depleted and reached a peak altitude of 1292 ft. This altitude is very close the estimate of 1200 ft obtained from Rocsim-PRO assuming no wind. The data recorded from the R-DAS is shown in Figure 55.
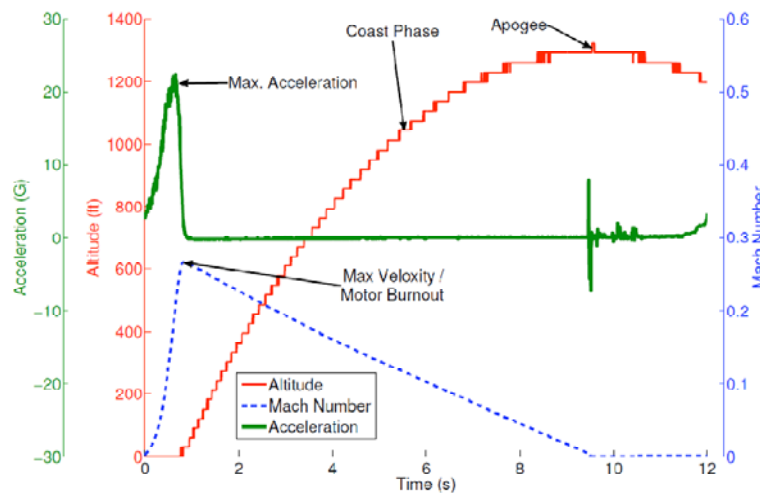
Figure 55: R-DAS Flight-data from test launch of the flight vehicle powered by the ALICE motor.

This close agreement between recorded flight data and predictions indicates that the thrust profile and thrust magnitude experienced during flight were very similar to those recorded on the ground with the flight hardware. Similarly, it is observed that the peak *Isp* of 210 s calculated from the ground test data is a good estimate for the flight *Isp*.

Hydrogen Peroxide and Aluminum Mixtures

This work has shown that a "green" propellant made exclusively from aluminum and water is possible. Aluminum and ice propellants can serve as a stepping stone to the development of similar, high-performance formulations such as aluminum + hydrogen peroxide and aluminum hydride + hydrogen peroxide. The theoretical *Isp* performance of these propellants as compared to several ALICE varieties is shown in Table 14 and Figure 56. Assuming larger aluminum particles could be used, the amount of aluminum oxide present in the aluminum particles would be reduced to less than 1%, boosting the theoretical performance of the mixtures. As shown in Table 14, mixtures containing peroxide as the oxidizer exhibit much higher flame temperatures than both aluminum-water and alane-water. This should result in improved combustion efficiency and *Isp* values for mixtures containing hydrogen peroxide.

Table 14: Calculated results for Pc = 1000 psia, and Isp optimized for expansion to 14.7 psia and Isp vac uses an expansion ratio of 40

	Al - H_2O	Al - H_2O_2	AlH_3 - H_2O	AlH_3 - H_2O_2	AP/Al/HTPB[#]
Peak Isp (s) (P_e = 14.7 psia)	232.8	258.7	279.6	314.7	249.8
Peak Isp vac (s) (ER=40)	284.7	313.1	332.4	379.7	293.2
Chamber Temperature (K)	3084	3901	2421	3730	2832
C* (ft/s)	4466	4979	5422	6082	5003
O/F	1.0	2.5	0.9	0.9	3.8
Equivalence Ratio	1.00	0.75	1.00	3.85	-
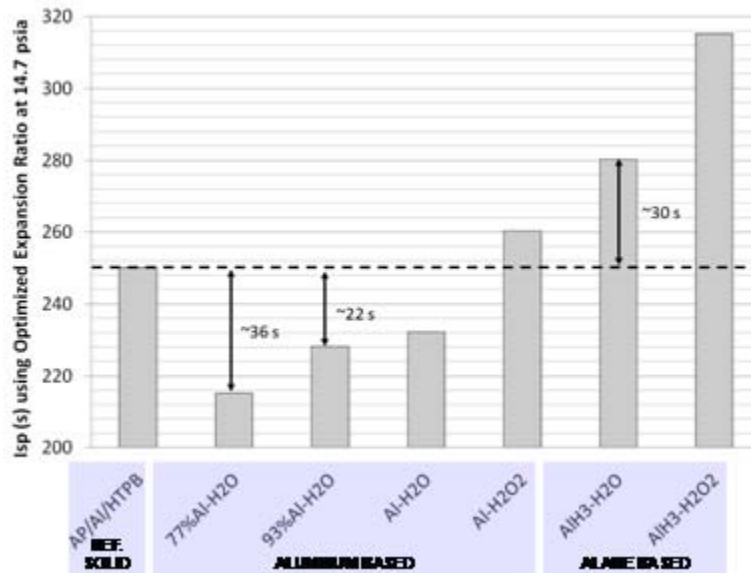
Figure 56: Optimal *Isp* expanded to 14.7 psia from a chamber pressure of 1000 psia for aluminum-water, aluminum-hydrogen peroxide (100%), alane-water, and alane-hydrogen peroxide (100%). Peak *Isp* values compared with the value of 249.8 s obtained from a solid propellant formulation AP/Al/HTPB/Fe$_2$O$_3$, with the respective ratios of 70.1/10.9/18/1 using the same code and conditions [76].

74

Motivated by the increase in theoretical performance and the higher temperatures, testing has begun to characterize the burning rate of mixtures containing micron aluminum, 4.5% fumed silica by mass, and hydrogen peroxide. The fumed silica is added to the mixtures to help with gelling. Images of 30% hydrogen peroxide ALICE quartz tubes burned in the constant volume combustion bomb are shown in Figure 57: Initial strand burning experiments using low concentrations of hydrogen peroxide suggest that the higher flame temperatures have the potential to improve motor combustion efficiency and could reduce the formation of solidified aluminum/aluminum oxide inside the combustion chamber. Strands that have been burned containing 60% hydrogen peroxide show very little post combustion deposits at all.
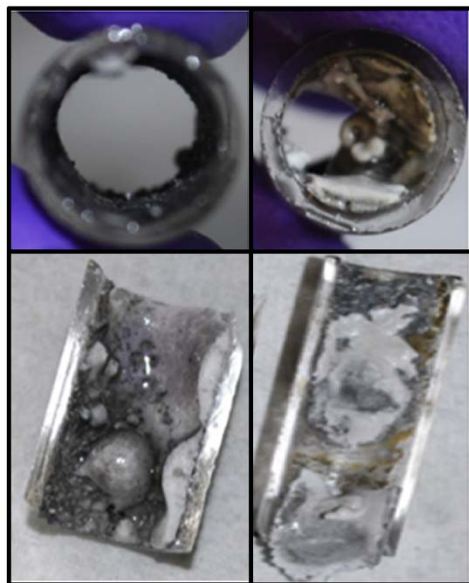
Figure 57: Comparison of the combustion products of both 30% peroxide containing ALICE using H2 (3 µm) aluminum (left) and ALICE containing 80 nm aluminum and water (right).

Preliminary burning rate data shown in Figure 58 shows that burning rates with hydrogen peroxide + water and micron scale aluminum lie above and below of the burning rate of ALICE depending on particle size and hydrogen peroxide concentration. Three micron aluminum sizes are shown on Figure 58, all defined by the supplier Valimet, the sizes include: 3 µm (H2), 12 µm (H10), and 20 µm (H15). Increasing the aluminum particle size appears to have a dramatic effect on the burning rate for aluminum sizes below H10. For sizes larger than H10, there appears to be less of an effect. This behavior suggests that for these particle sizes and propellant compositions, there is a transition between diffusionally limited and kinetically limited combustion. Mixtures containing the largest aluminum tested (H10 and H15) with only 30% hydrogen peroxide exhibit less stable burning, suggesting a lower deflagration limit for those mixtures. Safety testing is concurrently being done prior to conducting burning rates. The eventual goal of these exercises is to converge upon a high performance formulation containing 90%+ hydrogen peroxide.
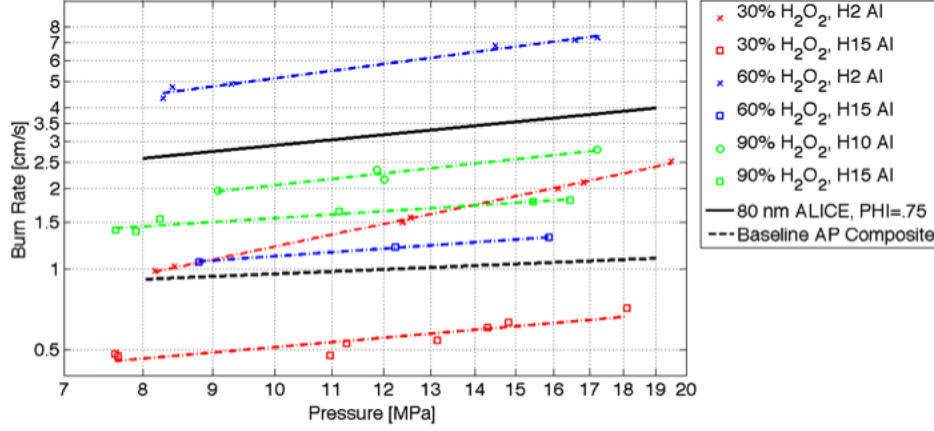
Figure 58: Burning rate data for hydrogen peroxide containing ALICE mixtures burned at O/F = 1.1.

By solving a linear regression model several variables can be ranked in importance through relative effects variance: (1) the aluminum particle diameter (D), (2) the H_2O_2 concentration (H), and (3), the oxidizer and fuel ratio (O). The model starts with the burning rate equation (15). This equation is modified using Eq. (16) and (17) to lead Eq. (18).

$$r_b = aP^n \tag{15}$$

Defining:

$$a = D^{\beta_4} H^{\beta_5} O^{\beta_6} \tag{16}$$

And:

$$n = \beta_0 + \beta_1 D + \beta_2 H + \beta_3 O \tag{17}$$

Leading to:

$$r_b = D^{\beta_4} H^{\beta_5} O^{\beta_6} P^{\beta_0 + \beta_1 D + \beta_2 H + \beta_3 O} \tag{18}$$

The β_i coefficients are then determined via linearization and regression analyses according to Eq. (19)

$$log_P(r_b) = \beta_0 + \beta_1 D + \beta_2 H + \beta_3 O + \beta_4 \, log_P(D) + \beta_5 \, log_P(H) + \beta_6 \, log_P(O) \tag{19}$$

Thermal Property Measurements

The TPS method is a single-step heating technique applied to characterize both thermal conductivity (k) and thermal diffusivity (α). The centerpiece of this method is a sensing element composed of nickel wire wound into a double spiral formation, surrounded in thin-film Kapton insulation (Figure 59). Available in multiple sizes, the appropriate sensor radius depends on the thermal characteristic of the test material. The nickel wire serves as an electrical resistor with the

wire leads of the sensor connected to one quarter of a Wheatstone bridge. A fixed resistance and a potentiometer complete remaining sections of the bridge. The potentiometer enables balance across the bridge prior to an experiment, measured with a digital multimeter. This assembly is integrated into a TPS 2500 apparatus from the Hot Disk Company [77]. The experimental uncertainty associated with the conductivity and diffusivity measurements are reported to be 2 and 5 % respectively [77]. Detailed descriptions of the TPS operation and analysis procedures have been reported elsewhere [78].

In the present application, the sensor is inserted between two identical samples of test material clamped together, as shown in Figure 59. The user defines the input power and duration for the experiment; appropriate values are usually determined through trial and error. Current is then supplied to the circuit to generate electrical heat in the sensor. A portion of this heat diffuses from the sensor into the surrounding samples, while the residual heat generates a temperature increase in the sensor. The temperature increase is inversely proportional to the thermal storage and diffusive properties of the sample material.
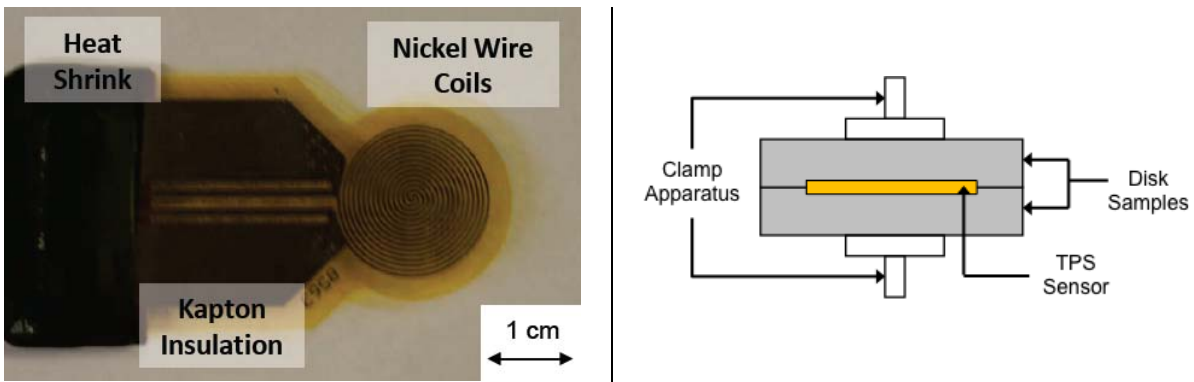
Figure 59: Left: Sensing element, Right: Generic experimental assembly.

Arrangements have to be made for measuring the thermal properties of ALICE and its derivatives. First, the material must kept frozen both to avoid decomposition reactions and to reproduce the experimental conditions in which it is first reacted in a rocket motor. Second, for additional safety, the experiments are performed under a fume hood or a well-ventilated area. Third, since the TPS sensor must be in close contact with the sample, a support was machined to hold it precisely in place while an ALICE freezes around it. Fourth, the TPS sensor support and the ALICE sample is placed in constant temperature bath that can be regulated down to approximately -30°C. The experimental setup developed to measure the thermal properties of ALICE is shown on Figure 60.
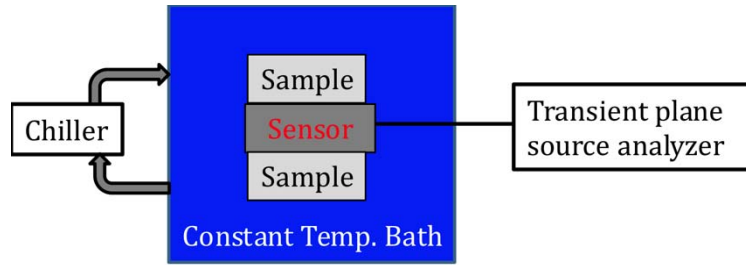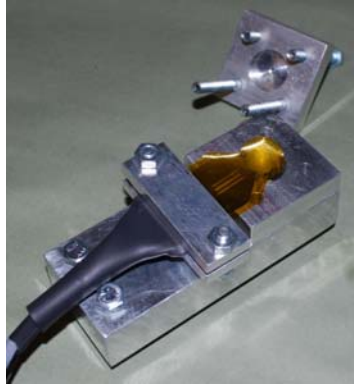
Figure 60: Left: Sensing element support for ALICE, Right: Generic experimental assembly.

Thermal diffusivity measurements using the TPS method show the thermal diffusivity of ALICE varies from 2 mm²/s at -30 °C to 1.25 mm²/s at -2 °C (Figure 61). These values compare favorably with the mass averaged thermal diffusivity value of 2 mm²/s. However, the mass averaged thermal conductivity of ALICE (Φ=0.75) is 100 W/mK, while measurements using the TPS method suggest a thermal conductivity of around 4 W/m-K (Figure 62). A study will be performed to understand the effect of these different values on the burning behavior of ALICE such as the steady state thermal profile and the ignition process.
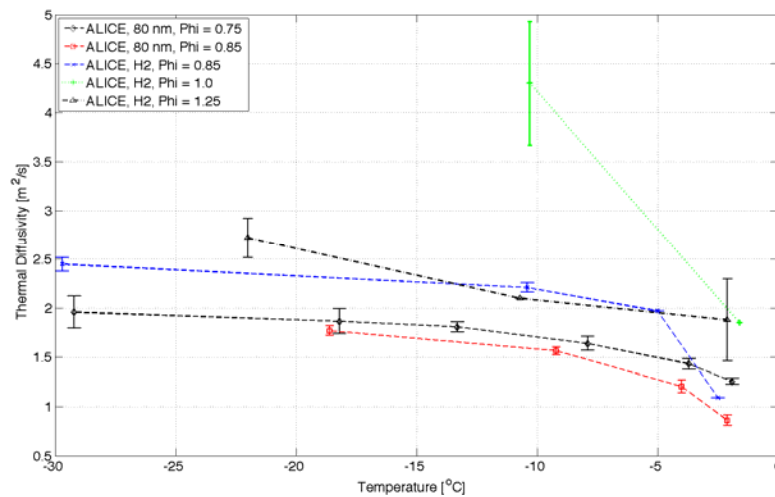
Figure 61: Thermal diffusivity of aluminum and ice propellants as a function of temperature.
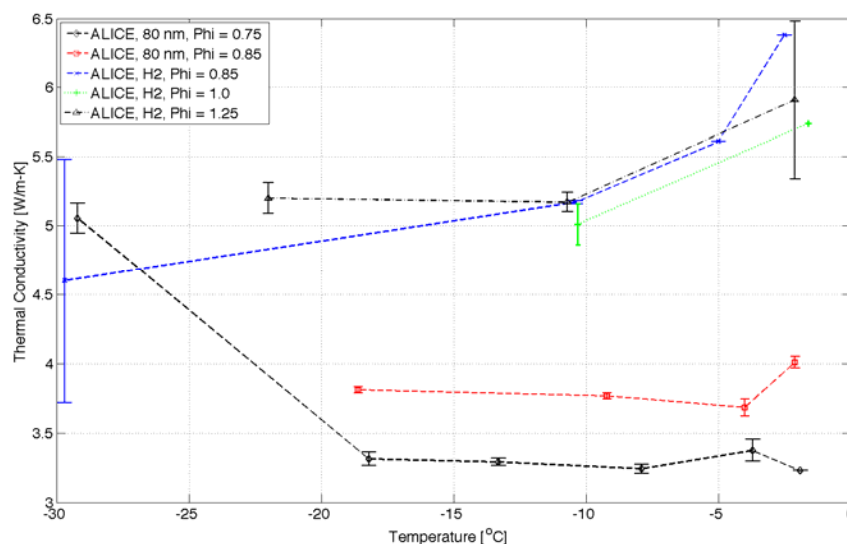
Figure 62: Thermal conductivity of aluminum and ice propellants as a function of temperature.

Metal Hydride Slurry Mixing and Reactivity

Metal hydrides have been considered by many as a candidate rocket propellant additive (79-82). However, many metal hydrides are either pyrophoric or appreciably degrade (dehydrogenate) in the presence of oxygen gas, excessive heat, or water vapor. One means of increasing metal hydride shelf life is to use a combination of surfactants and a hydrophobic carrier fluid to coat the particles. Like stabilization, surfactants could be used to form a protective, physisorbed or chemisorbed monomolecular barrier on the surface of the metal hydride particle. This approach has been developed recently by hydrogen storage researchers (83). Briefly, in 2008, McClaine and coworkers developed metal hydride slurries consisting of 75 wt.% lithium hydride (LiH) or magnesium hydride (MgH$_2$) dispersed within a mineral oil solution (83). The dispersions, stabilized using a small quantity of undisclosed surfactant, showed negligible signs of degradation after one month of storage in air. As some details of McClaine's slurry mixing procedure have been omitted from his final report, slurries, the purpose of this work is to qualitatively describe the mixing, settling, and reactivity of metal hydride slurries.

Procedure

Metal hydrides investigated in this study include MgH$_2$ (~50 µm), AlH$_3$ (~50 µm), and NaBH$_4$ (~200 µm). Prior to mixing, 2 wt.% Tergitol TMN-3 surfactant was added to the RP-1 and mineral oil. The liquid mixture was stirred vigorously for several minutes and then 60 wt.% metal hydride was added to the mixtures. Slurries were again mixed vigorously and tested for reactivity via exposure to flame (in air), water, and hydrogen peroxide.

Mixing and Settling Observations

The sodium borohydride slurry containing RP-1 completely separated after one day of storage, while the NaBH$_4$ slurry containing mineral oil showed moderate signs of settling.

79

Aluminum hydride or MgH_2 dispersed in mineral oil showed no signs of settling, but when dispersed in RP-1, settled slightly after 24 hours of storage.

Reactivity

Slurries were mixed with reacted in air (with flame) or with water or hydrogen peroxide in a variety of configurations. Key observations from these tests are shown in Table 15. In general, the reactivity of AlH_3 and MgH_2 are similar, while $NaBH_4$ appears much more reactive. Slurries containing mineral oil all were less reactive than their RP-1 containing counterparts.

Table 15: Summary of metal hydride reactivity

Test \ Material	MgH₂		AlH₃		NaBH₄	
	w/ RP-1	w/ mineral oil	w/ RP-1	w/ mineral oil	w/ RP-1	w/ mineral oil
Flame (in air) held to slurry	Lights but easily extinguishes	Extinguishes upon removal of flame, requires long delay	Lights but easily extinguishes	Extinguishes upon removal of flame, requires long delay	Lights but easily extinguishes	Ignites and burns slowly
Flame (in air) held to slurry + 90% H₂O₂	Bubbles moderately during mixing. Application of flame results in bright flash and combustion	Bubbles slowly during mixing. Application of flame results in bright flash and combustion	Bubbles slowly during mixing. Application of flame results in bright flash	Bubbles slowly during mixing. Application of flame results in bright flash	Hypergolic ignition	Hypergolic ignition (observably longer ignition delay)
Slurry mixed with water (room temperature)	Does not bubble; lights with flame application	Does not bubble; does not light with flame application	Does not bubble; does not light with flame application	Does not bubble; does not light with flame application	Bubbles slowly	Bubbles slowly
Slurry mixed w/ water (hot plate at ~100 °C)	Bubbles slowly	Bubbles slowly	No observable reaction	No observable reaction	Bubbles vigorously	Bubbles vigorously

Ammonia Borane as a Propellant Ingredient (in collaboration with Professors Stefan Thynell and Adri van Duin, The Pennsylvania State University)

The reaction of $H_2 + 1/2\ O_2 \rightarrow H_2O$ has a combustion enthalpy of 141.9 kJ/g, which gives it the highest heating value per unit mass of any naturally occurring molecule [84]. For this reason, hydrogen is the ideal fuel for space propulsion, since the weight of propellant is critical to an effective rocket propelled spacecraft. However, since it is an extremely low-density gas at standard temperature and pressure (0.08988 g L^{-1}), practical applications require storage at very high pressures or cryogenic temperatures. Boron also boasts a very high combustion enthalpy per unit mass (59 kJ/g) and the highest combustion enthalpy per unit volume (137 kJ/cm) for the reaction $B + 3/2 O_2 \rightarrow B_2O_3$. However, due to difficulties with ignition and reaction pathways that lead to the relatively stable HOBO molecule, the use of boron to improve performance in propulsion applications has been less than successful [85]. Boranes are compounds consisting of boron and hydrogen. Some borane fuels, such as diborane (B_2H_6) and pentaborane (B_5H_9), were studied as rocket propellants during the late 1940's and early 1950's. However, problems with safety and performance led to the discontinuation of this program [86].

Ammonia borane (NH_3BH_3, AB) is a compound of considerable interest due to its high hydrogen content (19.6% by mass). Unlike the borane fuels that were previously considered for propulsion, AB is relatively safe to store and handle [87]. Although isoelectronic with ethane, AB is a solid at ambient pressure and temperature due to a greater polarity and stronger intermolecular interactions than its organic analogue. As a result, AB does not require any special storage conditions. However, from Shore and Parry's initial works on AB [87,88], it was evident that the molecule was slightly unstable and would very slowly decompose to release hydrogen.

AB has received significant study of late, the majority of which is focused on the storage of hydrogen for use with proton exchange membrane fuel cells. Since AB releases a substantial amount of H_2 when it thermally decomposes, it has the potential to significantly lower the molecular weight of combustion products in a rocket motor. Since both specific impulse (I_{sp}) and characteristic velocity (C*) are inversely related to the molecular weight of the products, the use of AB as a fuel or fuel additive has the potential to greatly increase these parameters.

Equilibrium Calculations

Figure 63 shows the equilibrium products as a function of temperature for a stoichiometric reaction of AB and molecular oxygen at a pressure of 1 atm. . Equilibrium calculations were performed using CHEETAH 4.0 [89] with the JCZS product library developed by Hobbs and Baer [90]. Over the range of temperatures shown, the main equilibrium products always consist of gaseous H_2O, N_2, and to a lesser extent, H_2. However, the species containing boron atoms changes significantly over this range. Below 650 K, the majority of boron exists as BO_2H in the solid phase. Between 650 and 900 K, boron exists mostly as gaseous $B_3H_3O_6$ (boric acid) combined with gaseous $B_3H_3O_3$ and liquid phase B_2O_3. Liquid B_2O_3 is the primary boron containing species from 900 K, until gaseous HOBO overtakes it around 1700 K.
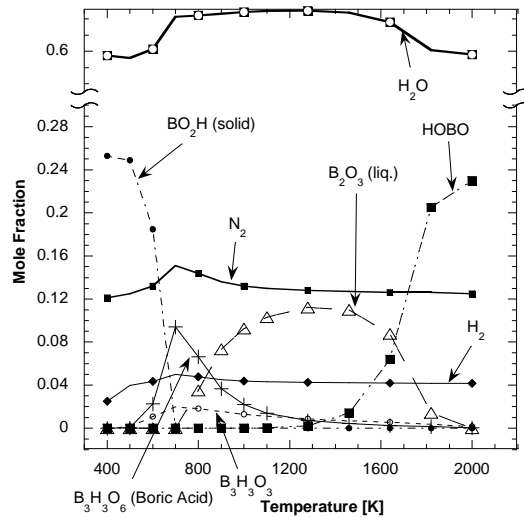
Figure 63: Mole fractions of equilibrium products of a stoichiometric reaction of AB and molecular oxygen at a pressure of 1 atm.

Figure 64 shows the mixture molecular weight for the products of stoichiometric reaction between AB and molecular oxygen compared with other common fuels for rocket propulsion. Pure water vapor has the lowest molecular weight at 18 g/mol. The products of stoichiometric combustion of AB yield a mixture molecular weight of 25.7 g/mol, regardless of whether the boron ends up as B_2O_3 or HOBO. Although greater than H_2O, the molecular weight of AB combustion products is still significantly lower than other common solid fuels, as shown in Figure 64. This suggests that the use of ammonia borane as a fuel may be an attractive alternative to cryogenic hydrogen in applications that require high I_{sp} and storable fuel.
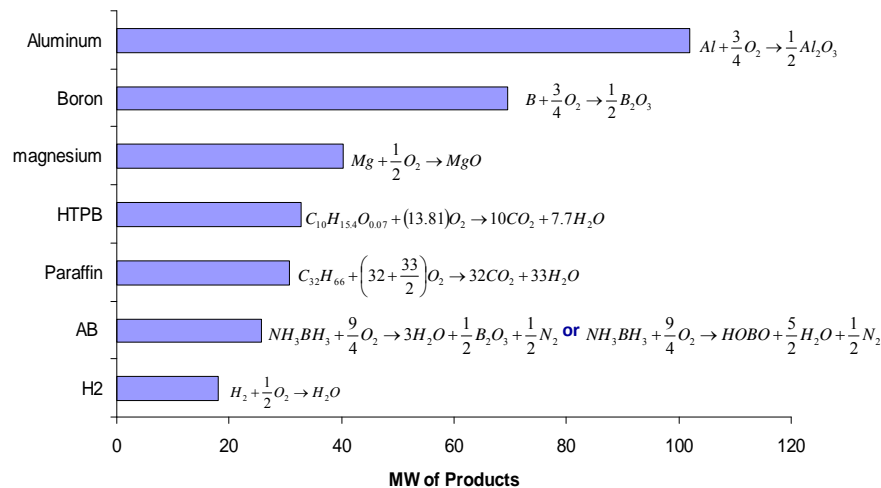
Figure 64: Mixture molecular weights for products of combustion of several fuels with pure oxygen.

82

One objective of this research is to test AB as a solid fuel in a hybrid rocket engine. Figure 65 shows (a.) the chamber temperature (T_C) and (b.) the characteristic velocity (C*) plotted versus the oxidizer to fuel ratio for several fuels: hydroxyl-terminated polybutadiene (HTPB) ($C_{10.0}H_{15.4}O_{0.07}$, h_f= -12.4 kcal mol^{-1} [91]), pure paraffin wax ($C_{32}H_{66}$, h_f= -166.5 kcal mol^{-1} [91]), and paraffin wax with different mass additions of AB (NBH$_6$, h_f= -13.5 kcal mol^{-1} [92]). The oxidizer is gaseous O$_2$, and a chamber pressure (P_c) of 200 psi was used in each case. A relatively low chamber pressure was targeted in this study, since combustion in a hybrid rocket motor is diffusion limited and nearly independent of pressure. Performance improves only slightly at higher pressures, so a low pressure is used to maximize the safety of the system. All calculations were made with the NASA CEA code [93]. Although pure AB theoretically offers the best performance, it is available only in powder form, so the use of a binder makes the fabrication of solid fuel grains easier. The paraffin wax fuel exhibits a decreased T_C and C* when compared with the standard HTPB fuel. However, the addition of AB raises the TC in addition to adding more H$_2$ into the reactants, which drives down the molecular weight of the products (MW$_{prod}$). These factors result in a greatly increased C* for the paraffin/AB fuels.

(a.)   (b.)
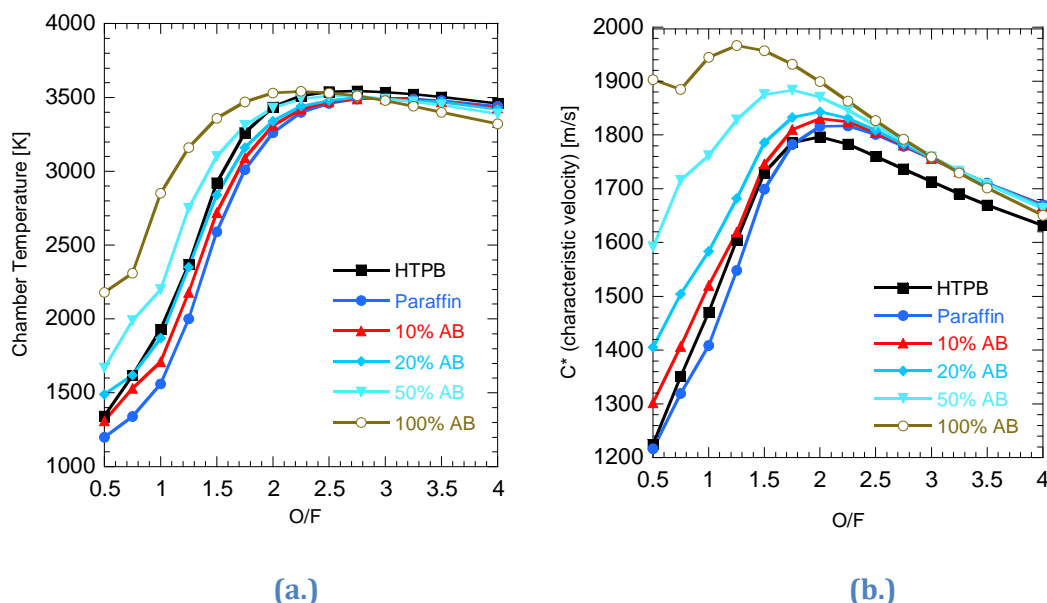
Figure 65: a.) Chamber Temperature (Tc) and b.) characteristic velocity (C*) versus O/F for various fuels paired with Gox. P$_c$=200 PSIG.

Reactive Force Field Molecular Dynamics Simulations

To aid in evaluating AB as a potential fuel for chemical rocket propulsion applications, we first approached the reaction at molecular level. To gain an atomistic description of a molecular system at relatively long time scales (compared to pure quantum mechanics (QM) calculations), molecular dynamics (MD) simulations were undertaken with a reactive force field. A ReaxFF reactive force field that modeled the reaction of B-N-H molecules and boron oxidation was developed in collaboration with Prof. Adri van Duin to simulate the processes of AB decomposition and oxidation [94].

ReaxFF force fields nearly retain the accuracy of QM but significantly reduce the computational cost. ReaxFF force field parameters are derived predominantly from QM, so it may be directly applied to novel systems that may not have been extensively studied experimentally. This makes it a very attractive tool for exploring AB oxidation kinetics. For details on the development of this force field to describe AB, please refer to [94].

In order to demonstrate the validity of the force field for MD, constant-atom/volume/temperature (NVT) simulations of AB pyrolysis and oxidation were performed. It was shown that, at the high temperatures used in these simulations (1000-3000 K), uni-molecular H_2 elimination is fast compared to the other reactions in the system, and the dominant mode by which AB decomposes. Figure 66 shows snapshots of a single molecule simulation at 2000 K, in which AB undergoes a uni-molecular hydrogen elimination. The plot of the reaction rate coefficient versus inverse temperature, which is also shown in Figure 66, contains data for several different starting configurations and temperatures. An Arrehnius fit was made to the data, and the activation energy (26.36 kcal/mol) is in good agreement with experimental results for the first hydrogen release from AB.

$$ k = A \cdot \exp\left(\frac{-E_A}{RT} \right) $$

A=4.895*10^{15} [sec^{-1}]
E$_a$=26.36 [kcal/mol]
or 110.3 [kJ/mol]
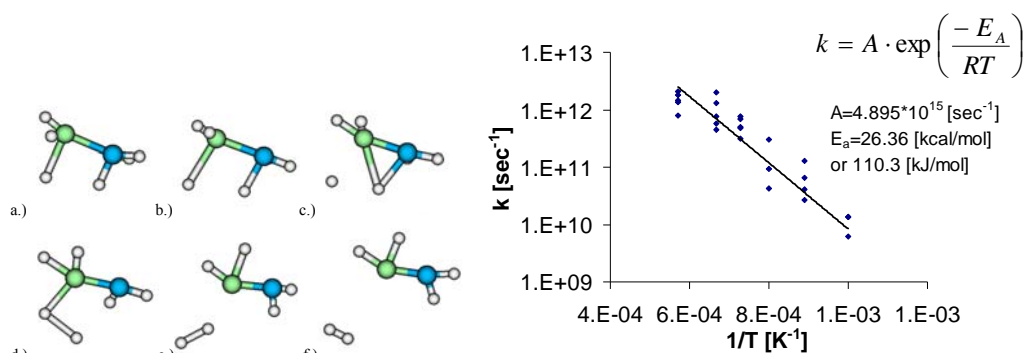
Figure 66: Sequence of images showing the release of H$_2$ from AB. (Green=Boron, Blue=Nitrogen, White=Hydrogen) and Reaction rate constant (k) versus inverse temperature with Arrhenius fit for single AB molecule, constant temperature simulations.

A poly-molecular AB system was studied using a temperature ramp (from 300-5000 K) simulation. The rate of hydrogen release per increase in temperature is shown in Figure 67. For AB, the rate was shown to peak at approximately 1250 K. An identical simulation was performed with the monomeric aminoborane (H_2NBH_2) molecule, in order to investigate the second equivalent hydrogen release. The rate of hydrogen release peaked around 2150 K for H_2NBH_2. In the case of AB, we observe the release of the first and second equivalent hydrogen, which is why the release starts at lower temperatures and remains substantial over a longer range of temperatures. In the H_2NBH_2 simulation, we are able to observe where the release of the second hydrogen molecule occurs. The release of a third equivalent hydrogen requires the formation of a B-N structured polymer, since the four-body member needed to eliminate an H_2 from the HNBH molecule would be an extremely high-energy transition state. Although some polymerization is realized in the simulations, the time scales required for this process are much longer than for the uni-molecular reactions.
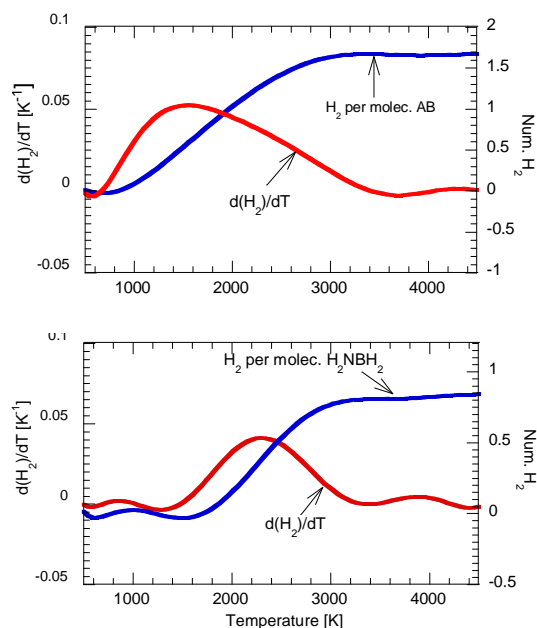
Figure 67: Rate of hydrogen release per change in temperature for 50 AB and 50 H₂NBH₂ temperature ramp simulations.

Additionally, the temperature ramp simulations showed that at low temperatures, AB forms significant quantities of NH_3 and BH_3, through B-N bond cleavage. However, these molecules recombined as the temperature eclipsed 1200 K. Nguyen et al [95] use transition state theory to argue that BH_3 acts as a catalyst in H_2 elimination from AB. However, in the MD simulations presented here, the BH_3 molecules tend to recombine with NH_3 instead of interacting with the AB molecules. At higher temperatures, the uni-molecular H_2 elimination is fast, and there is not sufficient time for the bi-molecular BH_3 catalysis reaction to take place. The catalytic BH_3 reaction may become dominant if the simulations are held at lower temperatures, and the NH_3 molecules are allowed to escape from the system.

B-N polymers were observed to form from dehydrogenated AB molecules. This polymerization takes place over much longer time scales than the uni-molecular hydrogen release. This polymerization is similar to that observed by Wolf et al. [96] in experiments. The polymerization peaks around 2500 K in the simulation, since at the higher temperatures the polymers tend to break apart.
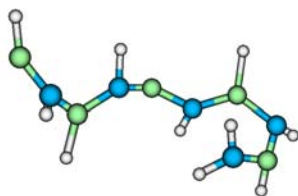
Figure 68: Example of B-N polymer formed during MD simulations (Green=Boron, Blue=Nitrogen, White=hydrogen). B-N chains form as the AB molecules become dehydrogenated. At higher temperatures, these polymers tend to break apart.

85

Since boron oxidation is an important step in the oxidation of AB, MD simulations have also been performed to demonstrate the ability of the ReaxFF force field to model this process. The temperature ramping (300-4300 K) MD simulations of boron and oxygen start with B atoms and O_2 molecules randomly distributed in a periodic box. At low temperatures, the simulations show the B atoms agglomerate into a cluster. As the temperature is elevated, O_2 molecules increasingly attack the outside of the cluster, as shown in Figure 69 a.), and eventually forms a condensed phase B_2O_3 structure, as shown in Figure 69 b.).

a.)   **b.)**
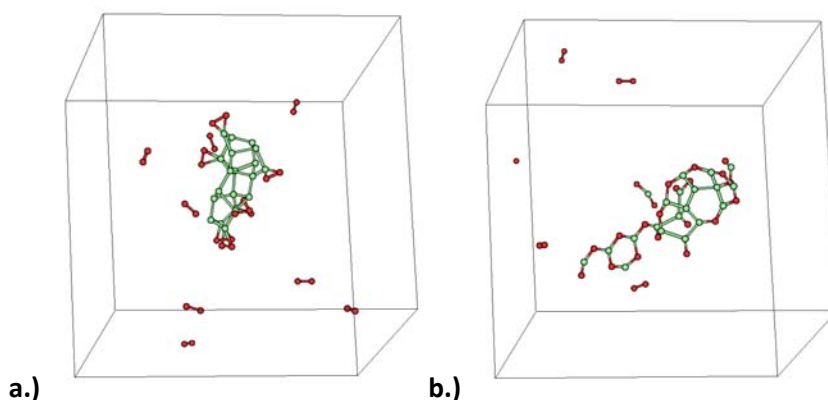
Figure 69: Snapshots from 20 B and 15 O_2 temperature ramp simulation (green=boron, red=oxygen) at a.) 1600 K and b.) 3600 K.

These results provide the confidence needed to employ ReaxFF to investigate the rapid oxidation of AB at an atomistic level. Figure 70 shows a plot of the major species observed versus temperature for a temperature ramping NVT MD simulation starting with 20 AB and 45 O_2 molecules, with an imposed heating rate of 0.00522 K/fs. Similar to the MD simulations without oxygen, some of the AB is converted to NH_3 and BH_3 through B-N bond cleavage in the low temperature range. The NH_3 and BH_3 do not oxidize, and the B-N bonds begin to reform as the temperature increases beyond 1500 K. Around 1000 K, H_2 begins to be generated through the uni-molecular hydrogen elimination from AB. The H_2 molecules are oxidized to form H_2O, while the B-N containing molecules undergo a complicated reaction sequence, which ultimately ends up producing N_2 and HOBO. Further QM and ReaxFF studies are being conducted to investigate these reaction pathways, with the goal of postulating a continuum kinetic model to be used in describing combustion experiments with AB.
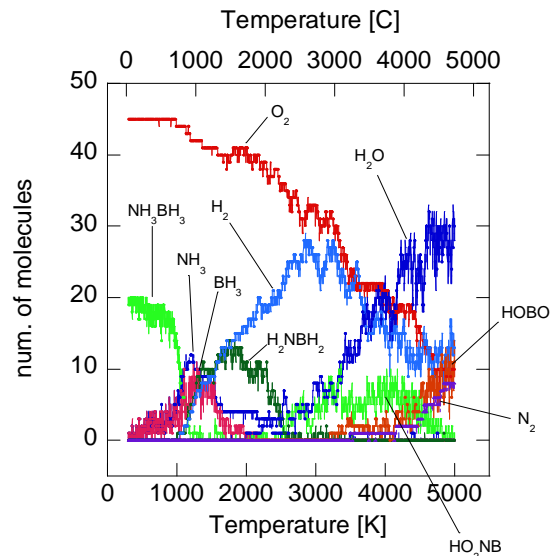
Figure 70: Temperature ramping MD simulation of AB and oxygen molecules.

Thermal Decomposition Experiments

The thermal decomposition of ammonia borane was first studied by Hu *et al.* [97] using thermogravimetric analysis (TGA), where the sample was heated to 200ºC at 5 K/min. A rapid mass loss of approximately 32% occurred between 120ºC and 133ºC, and an additional 3% was lost gradually from 133-200ºC. Recently, renewed interest in AB as a means of hydrogen storage has led to additional studies on its decomposition. A series of publications emanating from a group at Friedberg University of Mining and Technology [96,97,98] studied the decomposition of AB using a combination of TGA, differential scanning calorimetry (DSC), Fourier transform infrared absorption spectroscopy (FTIR), and mass spectrometry (MS). The first of these studies shows that for sufficiently slow heating rates (0.05 K/min), or isotherms above 70ºC for sufficient time (~30 hours), AB fully completes the first decomposition step below its melting temperature (104ºC) [96]. After lengthy isotherms at temperatures ranging from 70-90ºC, the resulting condensed phase product was determined to be polymeric aminoborane [(NH$_2$BH$_2$)$_x$] [96]. Furthermore, this study of Wolf *et al.* [96] demonstrates that at the low limit of heating rate, AB can fully undergo its first exothermic decomposition step without changing phase, while at increased heating rates (>1 K/min), the compound will melt prior to the bulk of the decomposition. In the latter scenario, the gas released during decomposition results is a vigorous foaming of the melted AB.

For energetic materials, the kinetic decomposition pathways may be highly dependent on the heating rate [100]. Previous works [96-99] have only examined decomposition at low heating rates (≤10 K/min). To study the effect of heating rates on the decomposition of AB, we have used coupled thermo-gravimetric analysis and differential scanning calorimetry (TGA/DSC) to vary the heating rate form 2-50 K/min while measuring the mass loss and heat flow from the sample. The ammonia borane used in this study was purchased from Boroscience International. The material was found to be 98% pure, as specified by the supplier, using proton and [11]B nuclear magnetic resonance (NMR) spectroscopy. Its physical appearance is that of a white powder.

87

Thermal analysis was conducted using a simultaneous TGA/DSC apparatus (Netzch STA-449 Jupiter), which has a silicon carbide furnace with a maximum temperature of 1550ºC and a maximum heating rate of 50 K/min. The samples were placed in alumina crucibles that were covered with thin alumina lids that had a small hole to release the evolved gases. Samples masses were approximately 2.5 mg for each test.

The sample chamber is vacuum tight, and is evacuated and backfilled with a defined atmosphere prior to the start of each measurement. A top loading, low-drift balance with a resolution of 1 µg measures the change in sample mass. Two S-type thermocouples are attached to a platinum sample carrier, which holds both a reference and sample crucible, to measure heat flow from the sample. The onset melt temperatures of pure metal samples of Indium, Tin, Zinc, Aluminum and Gold were used to calibrate the temperature measurements. Prior to each experiment, a baseline measurement is made to compensate for buoyancy and specific heat effects in the TGA and DSC measurements, respectively.

Figure 71 shows data typical of a TGA/DSC experiment with ammonia borane. The left vertical axis shows percent mass loss/gain, and the right vertical axis shows heat flow in units of µV/mg, which is analogous to J/sec. The case plotted in Figure 1 is from a test performed in an inert argon atmosphere with a heating rate of 20 K/min. Two distinct mass losses appear in Figure 71. The first, with an onset temperature of approximately 113ºC, corresponds to a mass loss of 9.4 percent of the initial mass. The second mass loss corresponds to 19.0 percent of the initial mass, and has an onset temperature of roughly 152ºC. AB samples were heated up to 1400ºC, however nothing noteworthy appears in either the TGA or DSC signal above 250ºC.
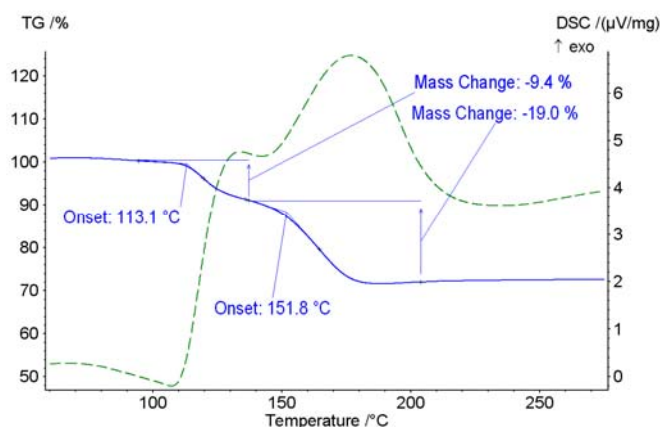
Figure 71: Thermo-gravimetric and differential scanning calorimetry data for AB heated at a rate of 20 K/min in an Argon atmosphere.

Figure 72 shows TGA data for AB decomposition at a range of heating rates, from 2-50 K/min. As the heating rate is increased over this range, the percent mass loss of the samples increases roughly two and a half fold. Figure 73 is a scatter plot of the percent mass loss as a function of heating rate with data from this study and Baitalow *et al.* [98]. Figure 73 shows that mass loss is a nearly logarithmic function of heating rate over the range of 2-50 K/min.
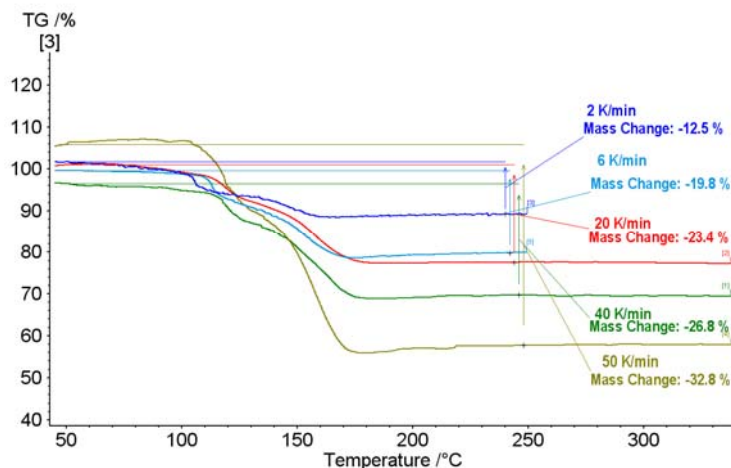
Figure 72: Thermogravimetric analysis (TGA) experiments with percent weight loss versus temperature for a range of heating rates. Labels and TGA traces have corresponding colors.
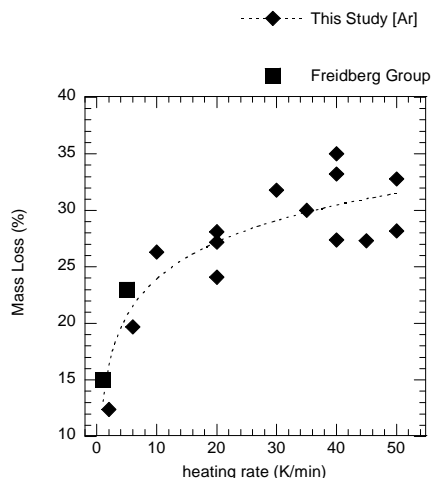
Figure 73: Percent mass loss versus heating rate for TGA experiments with AB.

To understand the decomposition behavior of propellant ingredients, it is widely recognized that high heating rates must be achieved. Therefore, ongoing work will examine the decomposition of AB using a confined rapid thermolysis (CRT) experiment, described in detail by Kim *et al* [101], with heating rates of approximately 2000 K/sec; approaching the rates found in propellant combustion.

Ammonia Borane/Methanol Droplet Study

Ammonia borane has good solubility in several liquids, including water (H_2O), diethyl ether [$(C_2H_5)_2O$], and methanol [$(CH_3)OH$]. To test the effect of AB as an additive to liquid fuels, AB was dissolved in methanol and burned as a droplet.

A droplet combustion chamber (50 mm x 50 mm x 50 mm) under stagnant ambient conditions was used to determine the burning rates of suspended AB/Methanol fuel droplets. The

chamber provides optical access from three sides. The fuel droplet was suspended on a quartz filament mounted at the center of the chamber. The suspending tip of the filament was rounded into a spherical bead (dia=0.8 mm) and bent at an angle of about 80° to minimize the contact length of filament with the high temperature region of the flame. The droplet was deposited on the bead using a syringe and ignited using a small torch. A backlight was used to create a shadow of the burning droplet, while being imaged using an Intensified CCD camera (Princeton Instrument Model PIMAX 2) mounted with a long-distance microscope lens (Infinity Model K2/S). The camera gate was fixed at 1 ms and images were taken at a rate of five frames per second with a pixel resolution of 3.19 μm/pixel. The change of droplet dimension was analyzed using a threshold method. Typical initial horizontal (D_h) and vertical (D_v) dimensions of the suspended droplets ranged from 1.5 to 1.8 mm. In order to see the effect of AB on the burning rate of droplet, 9.1%, 13.0% and 16.7% (by weight) of AB were dissolved in methanol. For each mixture case, ten individual runs were made from which the average burning rates were determined.

Figure 74 a.) and b.) show a series of shadowgraph images of the burning droplets of 100% methanol and 87% methanol/ 13% AB mixture (by weight), respectively. In both cases, the shape of suspended droplet is oblong (due to gravity) before ignition and becomes more spherical as it burns. For pure methanol cases, the droplet continued burning until the droplet size became only slightly bigger than that of quartz fiber bead and heat loss leads to the quenching of reaction. For the droplets containing AB, formation of gas bubbles was observed a short time after the droplets were ignited, as shown in Figure 74 b.). As the droplet gets smaller, gas appeared to evolve from its interior region. Bubbles observed inside droplet may be hydrogen generated via thermal decomposition of AB. Free falling droplet experiments are necessary to confirm the droplet fragmentation process from AB decomposition without the presence of any surfaces within the liquid droplet.

Since the burning droplets were not completely spherical, the droplets' burning rates are reported based on several dimensions: the vertical (D_v), horizontal (D_h) and equivalent (D_{eq}) droplet diameter. The latter was defined to correspond to a sphere with a volume that was equal to a volume of an ellipse rotated about its vertical axis. The equivalent diameter is defined by Eq. 20.

$$D_{eq} = (D_h^{\,2} D_v)^{1/3}$$ (20)

The burning rate is reported in Figure 75 terms of the burning rate constant (k), based on the classical D^2 law [102], as shown in Eq. 21.

$$D^2(t) = D^2(t=0) - kt$$ (21)

The error bars represent one standard deviation. The burning rate for pure methanol, based on the equivalent diameter, was 0.80 mm²/s. The burning rate was found to increase, at a nearly linear rate, with the addition of AB. The burning rate at the highest mass percentage of AB (13% by mass) was 0.95 mm²/s, roughly a 19% increase over the pure methanol droplet. The increase burning rate can likely be attributed to several factors associated with the release of hydrogen from the AB,

including the higher diffusivity of hydrogen and higher flame temperature associated with the hydrogen-oxygen reaction.
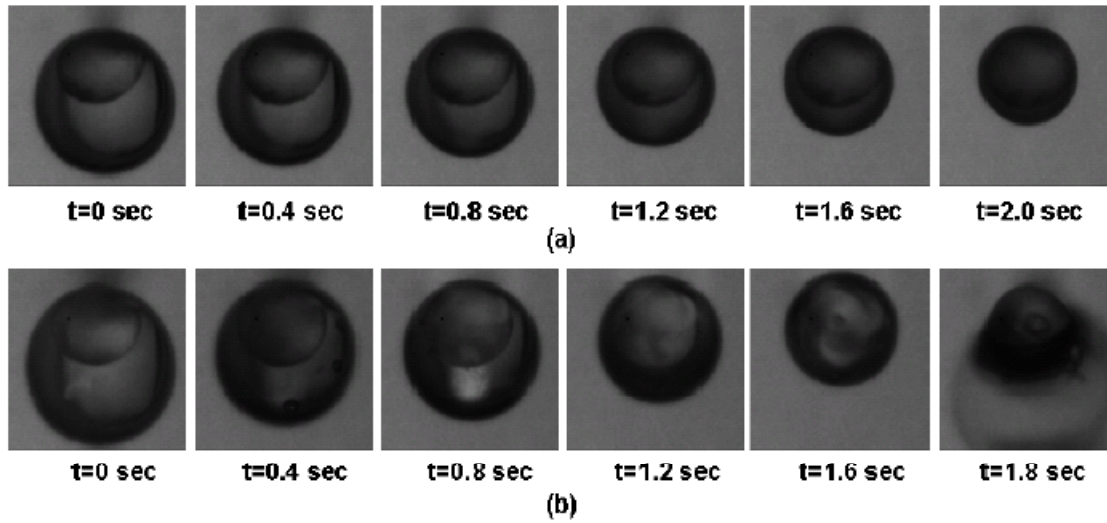
Figure 74: Shadowgraph images for burning droplets of a.) 100% methanol and b.) 87% methanol/13% AB. Experiments were performed at 1atm.
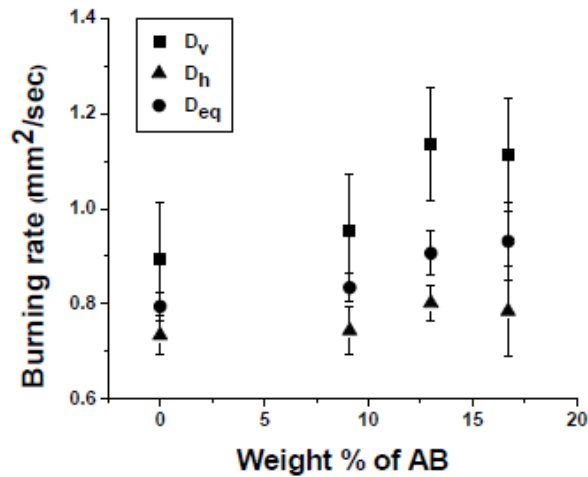
Figure 75: Droplet burning rate versus weight percentage of AB.

Ammonia Borane/Paraffin in Opposed Flow Burner

To investigate the effect on regression rate of adding AB to paraffin wax, experiments were conducted where a solid fuel grain was burned in a stagnation flow of pure oxygen. The distance between the exit of the oxygen flow and the solid fuel surface was held constant as 5 mm. The strain rate of the flame was varied by a change in the flow rate of the oxygen. Oxygen flow rates ranged from 0.9 to 3 l/min. Experiments were conducted at one atmosphere and room temperature. A wire was used to keep the burning surface stationary, and an Omega LD500-2.5 linear voltage displacement transducer (LVDT)

91

was used to measure the linear regression rate. A diagram and photograph of the stagnation flow region are shown in Figure 76.
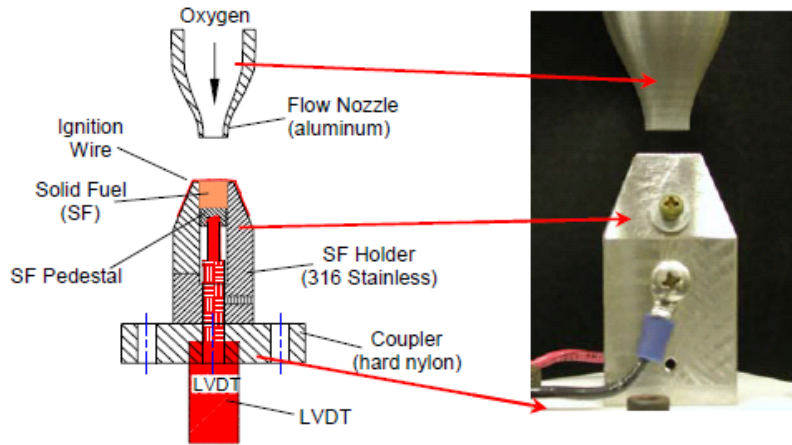
Figure 76: Diagram and photograph of stagnation flow burner.

Figure 77 shows a.) a plot of linear burning rate for 20% AB as a function of flow rate and b.) a plot of the linear burning rate of the AB/Paraffin composites versus the mass fraction of AB for two different oxygen flow rates (1.5 and 2.0 l/min). The data suggests that the burning rate is either increased or unaffected with increasing mass percentage of AB up until the point of 30% AB by mass. However, the burning rate was decreased at 40% AB addition. With increasing amounts of AB, it was observed that there was a more significant layer of condensed phase products that accumulates of the surface of the solid fuel. In the solid fuels with 40% AB, it is likely that this solid phase layer begins to inhibit the regression rate of the fuel.

(a.)

(b.)
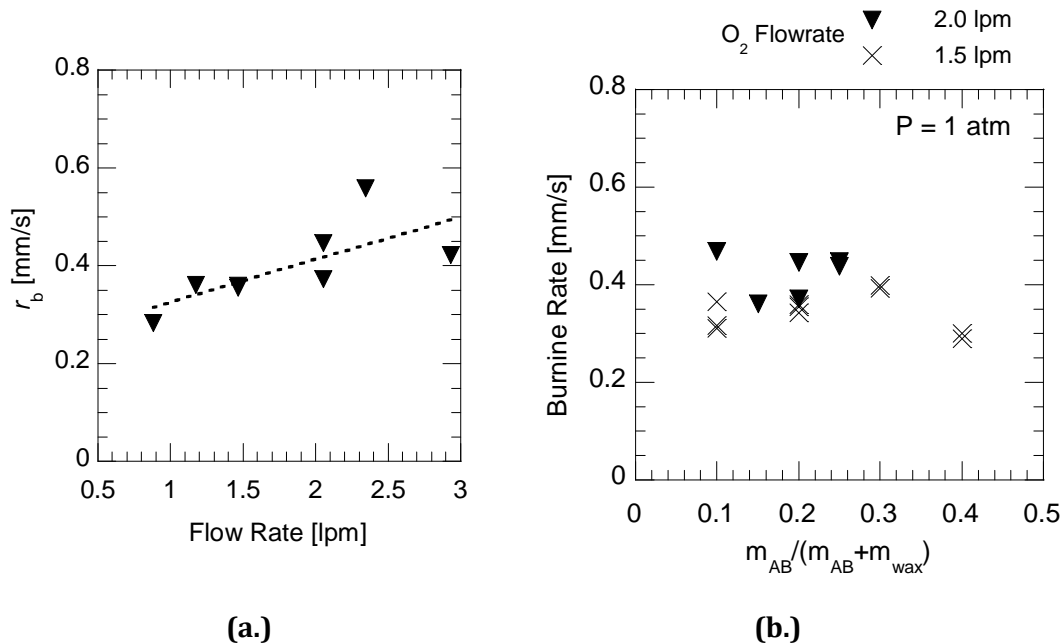
Figure 77: (a.) Burning rate of 20% AB/80% Paraffin versus flow rate and (b.) Burning rate versus mass percent of AB for 1.5 and 2.0 l/min.

Ammonia Borane Flame Spread

Figure 78 is an image from a flame-spread experiment conducted in a small (3"x3" cross section) wind tunnel with a pressed 1"x1/2"x1/16" sheet of AB. A flow of 90% Ar and 10% O_2 passed over this sheet, after going through a flow straightener, at a speed of 10 cm/s. The AB is ignited at the top end using a resistively heated nichrome wire, and the reaction propagates down the sheet (in the opposite direction of the flow) at an average rate of 3.6 mm/s. A bright green flame is visible from the reaction, due to the presence of BO_2^* emission in the area of 550 nm. After the reaction is extinguished, there remains a considerable amount of solid product. The products are of low density and constitute about 40% of the original mass.
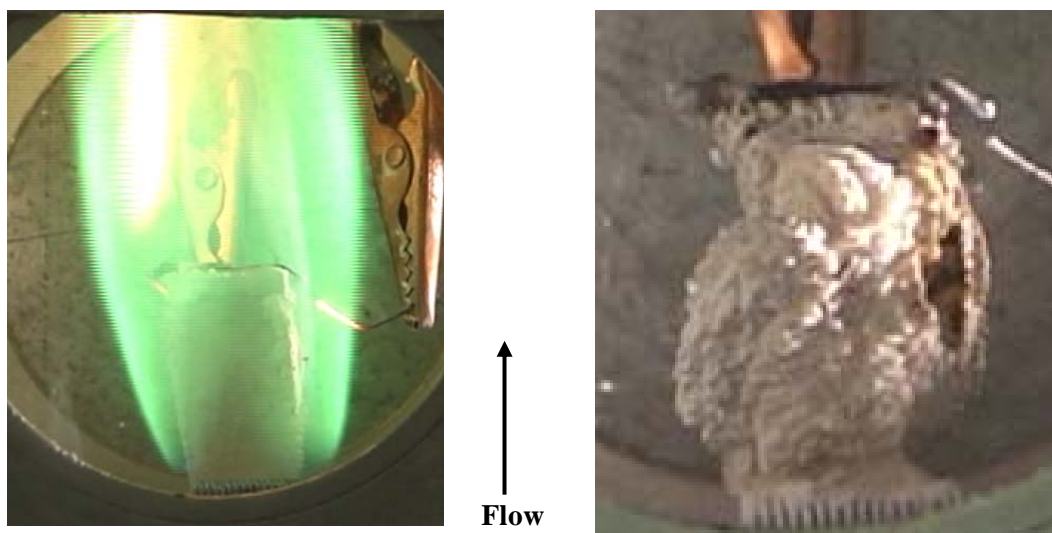
Flow

Figure 78: Flame spread experiment with AB sheet ignited in a flow of 90% Ar and 10% O2, with a velocity of 10 cm/s. Green flame is due to BO2* emission. The condensed phase products represent 40% of the original AB mass.

Characterization of AB Enhancement to a Hybrid Rocket Engine

To examine the ability of AB to increase performance in a chemical propulsion system, AB was studied as an additive to a solid fuel for a hybrid rocket system using gaseous oxygen as the oxidizer. For this study, AB was added to a paraffin wax binder. In addition to exhibiting higher regression rates, paraffin wax has the advantage of being a thermoplastic polymer. Attempts to mix AB with thermoset polymers such as HTPB and PBAN showed that AB interferes with the cross-linking process, making the manufacturing of grains difficult. Use of a thermoplastic binder removes the need for curing.

Performance of the AB and paraffin fuel was investigated using a laboratory scale hybrid rocket motor, previously detailed in [20]. Baseline Paraffin and HTPB solid fuels were tested first to check for consistency with previously reported data and to provide a point of comparison for the AB propellant. Initial and final fuel grain weights and port area measurements are used to calculate the solid fuel regression rate (r_b) and mass-burning rate of the fuel ($\dot{m}_{fuel}$). Measurements of

pressure and thrust were used to calculate the characteristic velocity (C^*) and specific impulse (I_{sp}), which were compared with theoretical values calculated using NASA CEA code [93].

The HTPB solid fuel was formulated from R-45M homopolymer resin and Isonate 143L methylene diphenyl isocyanate (MDI curing agent) with a ratio of MDI to R-45M of 13% by mass. The R-45M and MDI were stirred for approximately 10 minutes, and then place under a vacuum to remove any air entrapped during mixing. The mixture was then poured into paper phenolic tubes and allowed to cure for a minimum of 48 hours. The fuel port was then drilled out to the predetermined size (0.375 in). The fuel port entrance was left blunted in order to promote turbulent flow of the injected oxidizer.

Being a thermoplastic, paraffin wax does not require curing. However, the large difference in density between the liquefied paraffin and its solid form requires a centrifugal casting procedure [104]. When no force is applied to the grain as it cools, the large density change associated with solidification causes gaps to form between the paper phenolic casing and the fuel. However, if the grain is spun as it cools, the liquid paraffin is pressed outward against the phenolic casing, and a nearly circular port is formed in the center of the grain. For this study, paraffin was liquefied by heating to approximately 70°C, which is just above the melting temperature. A small amount (2% by mass) of carbon black (Cabot Monarch 580) was added to the liquid paraffin to increase the opacity of the fuel and prevent radiation from the combustion zone from penetrating deep into the fuel grain. The liquefied paraffin and carbon black were mixed for several minutes to disperse the particles. Subsequently, the liquid paraffin is poured into a paper phenolic cartridge and spun on a lathe until cooled.

The AB used in this study was purchased from BoroScience International, and the supplier's stated purity was 99%. When significant amounts of AB particles are added to the liquid paraffin wax, the mixture is no longer pourable. For the grains of paraffin-AB mixture, the AB powder, along with 2% carbon black, was added to the liquid paraffin and mixed for several minutes. The 'wet' mixture was then hand-packed into the phenolic cartridge around a mandrel machined to the required center port dimension using a plunger. The grain was allowed to cool, and then the mandrel was resistively heated so that it could be removed. No spinning was required to prevent gaps in these grains.

Figure 79 shows a diagram of the laboratory scale hybrid rocket (LSHR) engine. The design of the LSHR is described in detail in a previous paper [103]. The system uses expendable fuel cartridges, as well as sacrificial pre- and post-combustion chambers fabricated from medium grade low-density graphite. The pre-combustion chamber length can be varied to allow for different fuel grain lengths. For this study, some 3 in grains were used, but the majority of the experiments were conducted using 5.5 in grains. The ability to change the grain length allows for the study of scaling effects as well as greater ability to tailor the oxidizer-to-fuel (O/F) ratio. The chamber is sealed at both the injection and nozzle exit ends via piston seals with high temperature Viton o-rings. The nozzles were machined from isomolded high-density graphite with a 30° half-angle on the converging section and a 15° half angle on the diverging section. The nozzle throat diameter (d_{th}) was determined for each experiment using a semi-empirical model [103] so that P_c was approximately constant for each experiment. The area expansion ratio (A_e/A_{th}) was approximately

10 for each nozzle. Setra 206 pressure transducers were used to measure pressure in the pre- and post-combustion chambers of the rocket motor. The chamber assembly is sled mounted on precision linear guide bearings to facilitate instantaneous thrust measurement, via a 110 N (25 lb$_f$) Omega load cell positioned at the injection head end of the combustion chamber, with minimal friction losses. Combustion is initiated using an electric match positioned in the solid fuel port.
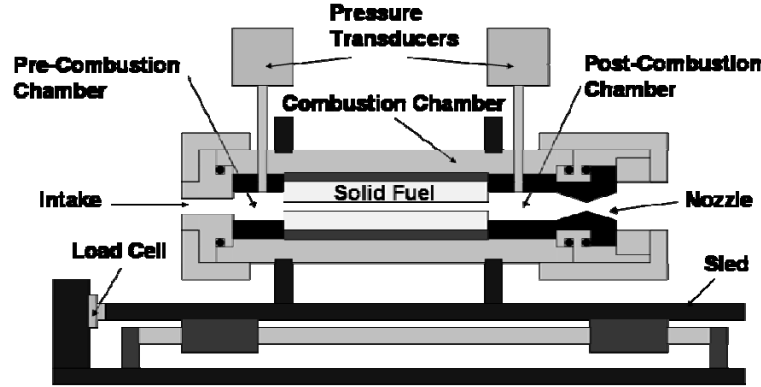
Figure 79: LSHR motor diagram.

A schematic of the gaseous oxidizer (GOX) flow system and other components of the LSHR experiment are shown in Figure 80. The GOX flow system consists of a bank of regulated oxygen tanks and stainless steel flow lines that lead to a double-acting pneumatic ball valve that is controlled remotely using a relay board and an auto-sequencing computer program. The oxidizer flow rate is metered using a choked critical orifice. The orifice diameter is known (d_{orf}=0.98765 mm), and the orifice was flow calibrated to determine a discharge coefficient (C_D) of 0.82. The mass flow rate under choked flow conditions can be calculated using Eq. 22,

$$\dot{m}_{ox} = \frac{C_D \cdot \Gamma(\gamma) \cdot P_{up,orf} \cdot A_{th}}{\sqrt{R \cdot T_{up,orf}}} \qquad (22)$$

where,

$$\Gamma(\gamma) \equiv \sqrt{\gamma}\left[\frac{2}{\gamma+1}\right]^{(\gamma+1)/2(\gamma-1)} \qquad (23)$$

95
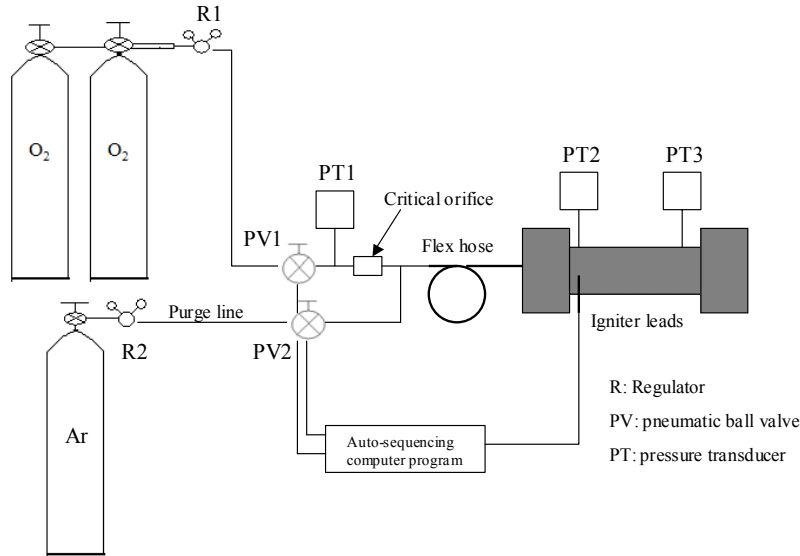
Figure 80: Schematic of LSHR experimental set-up.

The static pressure upstream of the critical orifice ($P_{up,orf}$) is also measured using a Setra 206 pressure transducer. Since the Mach number is low, the measured static pressures are assumed to be approximately equal to the stagnation pressures. A flex hose leads from the critical orifice to the injector head in the LSHR motor. Another pneumatic ball valve is used to control the flow of purging gas from a regulated argon bottle cluster. The argon is used to quench combustion and purge the system following each firing. A custom LabVIEW program was used for sequencing the experiment and recording data. The target fuel burning time for each experiment was determined using the semi-empirical model [103], and was input into the auto-sequencing program. The oxygen regulator (R1) was manually adjusted according to the target mass flow rate for each experiment. The auto-sequencing program first opens the oxidizer valve (PV1) and allows oxygen to flow for 3 seconds to ensure a steady state steady flow condition is reached. Next, the sequencing program sends voltage to the electric match, which explodes in the center port of the solid fuel grain, resulting in ignition of the fuel. After the input burn time has elapsed, PV1 is closed and the argon flow valve (PV2) is opened. The incoming voltage signals from the three pressure transducers and the load cell were sampled and recorded at 1000 Hz.

The results of a typical pressure and thrust trace for an LSHR experiment are shown in Figure 81. This particular data was from an experiment with a 5.5" grain of pure paraffin solid fuel. The P_{up} curve refers to the oxygen pressure upstream of the choked critical orifice, which is proportional to the mass flow rate of oxygen. P_c is the pressure inside of the post-combustion chamber. At t=0, the oxygen valve (PV1) is opened, and oxygen is allowed to flow for three seconds prior to ignition. After the initial spike, P_{up} is approximately constant during the experiment, so the oxidizer mass flow rate is considered fixed throughout the experiment. When the igniter is triggered at approximately 3 seconds, ignition is achieved and P_c and thrust (τ) rise up to a maximum value. P_c and τ decrease slightly throughout the course of the firing due to increasing chamber volume (resulting from increasing solid fuel port diameter). After the targeted burn time, which is pre-determined by the predicted regression rate, the oxygen valve (PV1) is closed and P_{up}

drops to zero. P_c begins to fall until the argon valve (PV2) is opened to purge the system. The actual burn time (t_b) is defined by the difference in time from when P_c reaches 50% of $P_{c,max}$ after ignition and when P_c again reaches 50% of $P_{c,max}$ after the oxygen is switched off. The thrust profile corresponds closely with the profile for P_c. Video footage was taken for each test, and Figure 82 shows a typical plume.
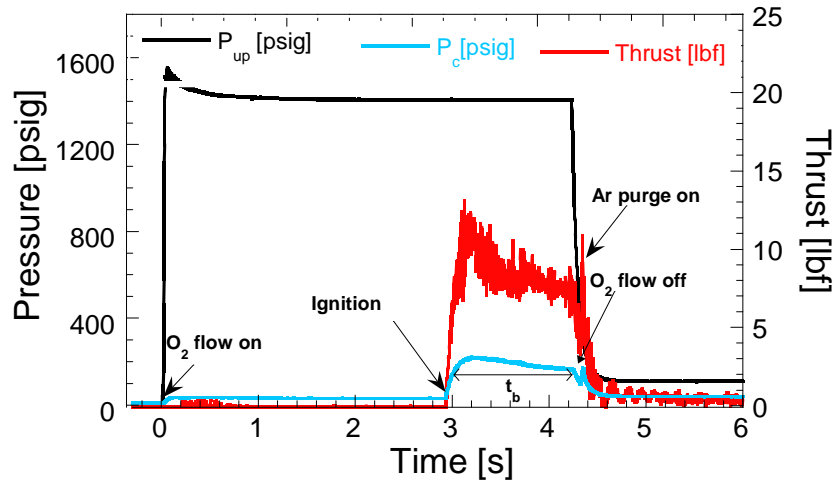
Figure 81: Pressure upstream of the critical orifice, chamber pressure, and thrust versus time for a hybrid rocket experiment using solid paraffin fuel and gaseous oxygen.

Figure 82: Typical exit plume for a static motor test with solid paraffin fuel and gaseous oxygen as the oxidizer.

To study the burning characteristics of the various fuels used in this study, the average linear regression rate was measured. The equation for the linear regression rate is given by Eq. 24,

97

$$r_b = \frac{dr}{dt} = \frac{r_i - r_f}{\Delta t} = \frac{D_{p,i} - D_{p,f}}{2t_b} \qquad (24)$$

where $D_{p,i}$ and $D_{p,f}$ the average initial and final port diameter. Since the solid fuel does not always regress evenly, a minimum of 10 measurements at the exit and inlet of the solid fuel grain were recorded and averaged. The regression rate for solid fuel in a hybrid rocket motor is nearly independent of pressure and strongly dependent on the oxidizer mass flux (G_{ox}) [22], according to Eq. 25

$$r_b = BG_{ox}{}^n \qquad (25)$$

Figure 83 a.) shows the average linear regression rate for the HTPB solid fuel used in this study compared with values found in the literature [103,105]. The burning rate data is plotted against the average oxidizer mass flux, as given by Eq. 26.

$$G_{ox,ave} = \frac{\dot{m}_{OX}}{0.5\left(A_{P,initial} + A_{P,final}\right)} \qquad (26)$$

HTPB, which is the standard fuel for hybrid rockets, was used as the baseline fuel because of its lengthy database. All data points for the HTPB experiments were for 5.5 in fuel grains. The similarity between the data in the present study and that found in the literature shows the current static-fire setup produces results consistent with previous work.

Figure 83 b.) shows paraffin and AB/paraffin solid fuel grain regression rates versus the average oxidizer mass flux ($G_{ox,avg}$). Pure paraffin (with carbon black) was run in both 3 in and 5.5 in grains. When compared with data from Evans *et al.* [104], the burning rates for pure paraffin at both grain sizes show good agreement. After 10% (by mass) AB is added to the grain, the regression rate (r_b) is increased compared to pure paraffin, for both of the flow rates tested. At the highest oxidizer mass flux value, 20% AB addition corresponded to and increased r_b compared to pure paraffin at a similar Gox, but a decreased r_b compared to the 10% AB addition case. At the lower G_{ox} value, r_b was noticeably decreased compared to both the pure paraffin and 10% AB addition case. Finally, the 50% AB addition case showed significantly lower r_b than the other compositions. Only one case was run with the 50% AB composition, due to the expense of the AB material.

r_b [mm/s] = 0.100*$G_{ox}^{0.519}$

Risha, 2003
Connell *et al.* 2009
Present Study
Fit

(a.)

paraffin [mm/s] (3" grains)
paraffin [mm/s] (5.5" grains)
10% AB (5.5" grains)
20% AB (5.5" grains)
50%AB (5.5" grains)
paraffin [mm/s] (B.Evans et al. 2004)
Paraffin fit

r_b=0.015$Gox^{1.17}$

r_b=0.09$Gox^{0.81}$

r_b=0.20$Gox^{0.57}$

(b.)
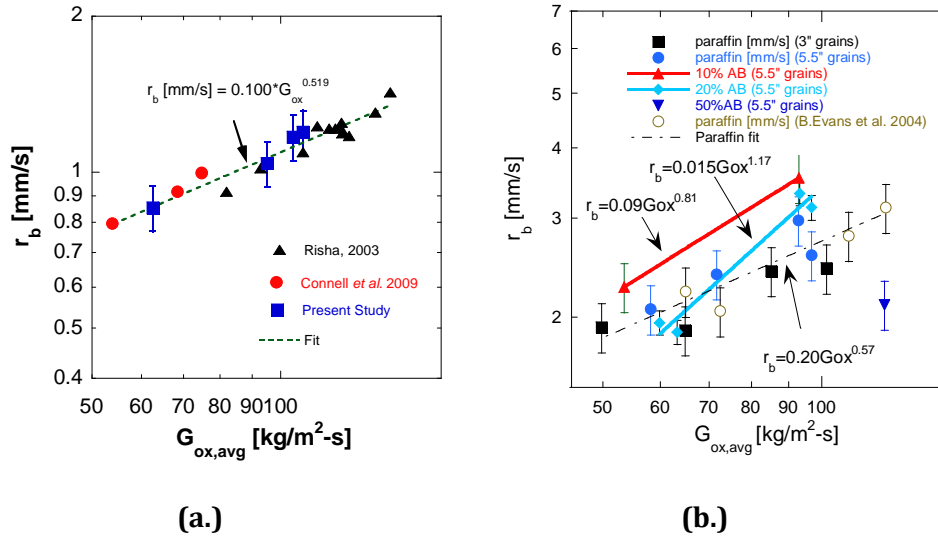
Figure 83: Solid Fuel linear regression rate versus average oxidizer mass flux for (a.) HTPB solid fuel and (b.) paraffin and AB solid fuels.

Figure 84 further illustrates the effect of AB addition on r_b. The linear regression rate of the fuel is plotted against the mass percentage of AB for oxidizer flow rates of approximately 14 g/s. The regression rate trends upward with small amounts of AB addition, but appears to be reduced when addition is greater than 20%. An increased regression rate was expected with AB addition, since AB increases the flame temperature. Additionally, the increase in H_2 concentration corresponding to AB addition should increase the rate of diffusion of fuel into the flame zone. However, the trend in this data appears to agree with results reported using an opposed flow stagnation burner, where it was reported that at the higher AB addition quantities, a condensed phase "ash" was built up on the surface during reaction. This condensed phase product likely inhibits the diffusion of reactants into the flame and the heat feedback to the un-reacted fuel, thus reducing the regression rate. The starvation of fuel to the flame may explain the very large G_{ox} exponent (n) in the curve fit. If a condensed phase product forms on the fuel surface in the case of AB addition, a higher cross-flow velocity may be able to remove more of this product from the surface, whereas when the cross-flow velocity is lower, more of the product may remain and inhibit diffusion into the reaction zone.
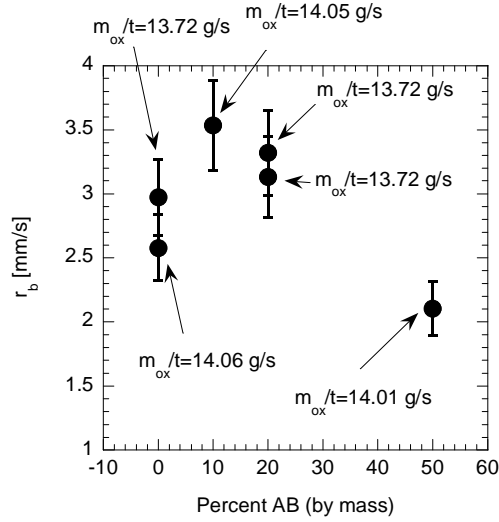
Figure 84: Solid fuel regression rate versus percent AB by mass for LSHR motor experiments with oxidizer flowrates of approximately 14 g/s.

The characteristic velocity (C*) for the AB/paraffin solid fuels is plotted versus O/F in Figure 85 a). Equations for C* and the O/F ratio are given by Eq. 27 and Eq. 28, respectively.

$$C^* = \frac{P_c A_{th}}{\left(\dot{m}_{fuel} + \dot{m}_{ox}\right)} \tag{27}$$

$$O\!\!\Big/\!\!F = \frac{\dot{m}_{ox}}{\dot{m}_{fuel}} \tag{28}$$

Figure 85 b shows the characteristic velocity efficiency, as given by Eq. 29,

$$\eta_{C^*} = \frac{C^*_{actual}}{C^*_{theor}} \tag{29}$$

100

where C^*_{actual} comes from empirical results and C^*_{theor} comes from the NASA CEA code [93]. C^* is an indicator of the propellants performance independent of the nozzle performance. Characteristic velocity is a measure of the propellants ability to generate pressure and can be directly related to the chamber temperature (T_c) and inversely related to the molecular weight of the products of combustion (MW_{prod}). C^* is a function of the O/F ratio and is typically optimized at a composition slightly fuel-rich of a stoichiometric. As predicted by the equilibrium calculations in Figure 1, the addition of AB to paraffin has the effect of increasing C^* for a given O/F ratio. This can be attributed to an increase in T_c and an increase in the amount of H_2 in the products, corresponding to a decrease in MW_{prod}. The C^* efficiency, as shown in Figure 85b, was very close to unity for all the experiments performed with the AB/paraffin solid fuel, showing that the combustion efficiency of the system is very high.

(a.)   **(b.)**
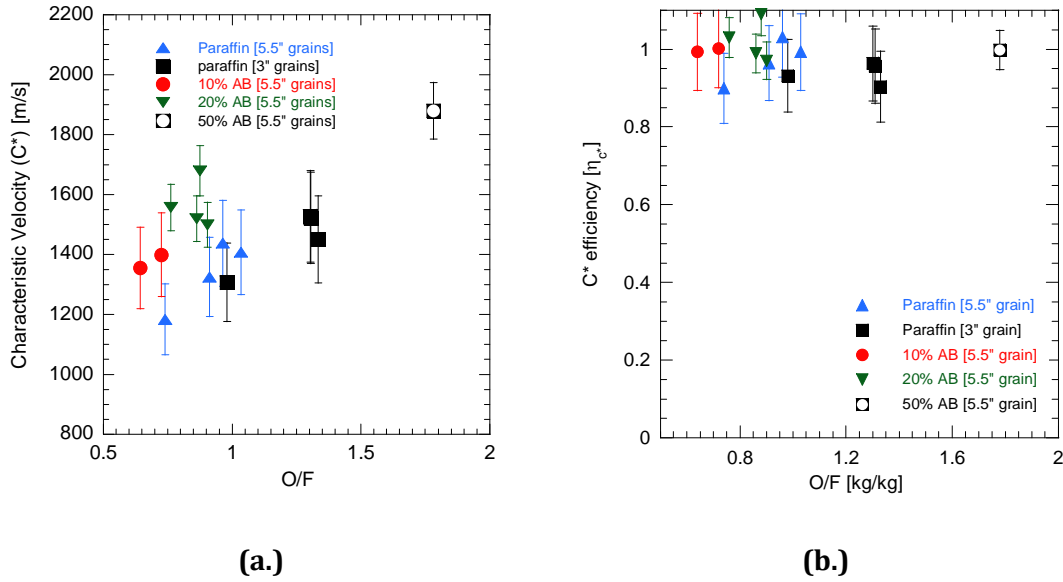
Figure 85: Characteristic velocity versus oxygen to fuel ratio for paraffin and AB solid fuel burned with gaseous oxygen.

The specific impulse (I_{sp}) and specific impulse efficiency (η_{Isp}) are plotted versus O/F for the AB and paraffin compositions are plotted in Figure 86 a.) and b.), respectively. Specific impulse, which is defined by Eq. 30, is the total impulse divided by the weight of fuel and oxidizer reacted. To calculate I_{sp}, the thrust measured using the load cell was numerically integrated over the burning time to calculate total impulse, which was subsequently divided by the summation of the weight loss of the solid fuel and the calculated m_{ox} from the gaseous oxygen flow.

$$I_{sp} = \frac{\int_{t_0}^{t_b} \tau \cdot dt}{\left(m_{fuel} + m_{os}\right)g} = \frac{\tau}{\left(\dot{m}_{fuel} + \dot{m}_{ox}\right)g}$$

$$(30)$$

101

The specific impulse efficiency is defined by Eq. 31 and was again calculated using the NASA CEA code [93].

$$\eta_{Isp} = \frac{I_{sp\,actual}}{I_{sp\,theor}}$$ (31)

The I_{sp} for the 20% AB addition is increased by approximately 10% compared to the experiments with pure paraffin at similar O/F ratios. However, the performance does not appear to be significantly increased in the case of the 10% AB addition. The highest I_{sp} recorded was for the 50% AB case, which was 173 sec. Since this grain burned much slower than the others, and also had a lower fuel density, the O/F ratio is significantly higher than for the other experiments, making comparison difficult. The I_{sp} efficiencies reported in Figure 86 b.) range from 0.55 to 0.65, and are relatively independent of the grain length and AB mass addition. Since the characteristic velocity efficiencies were very high for these experiments, it is likely that the relatively low I_{sp} efficiencies are due to either flow losses or heat losses in the nozzle.

(a.) **(b.)**
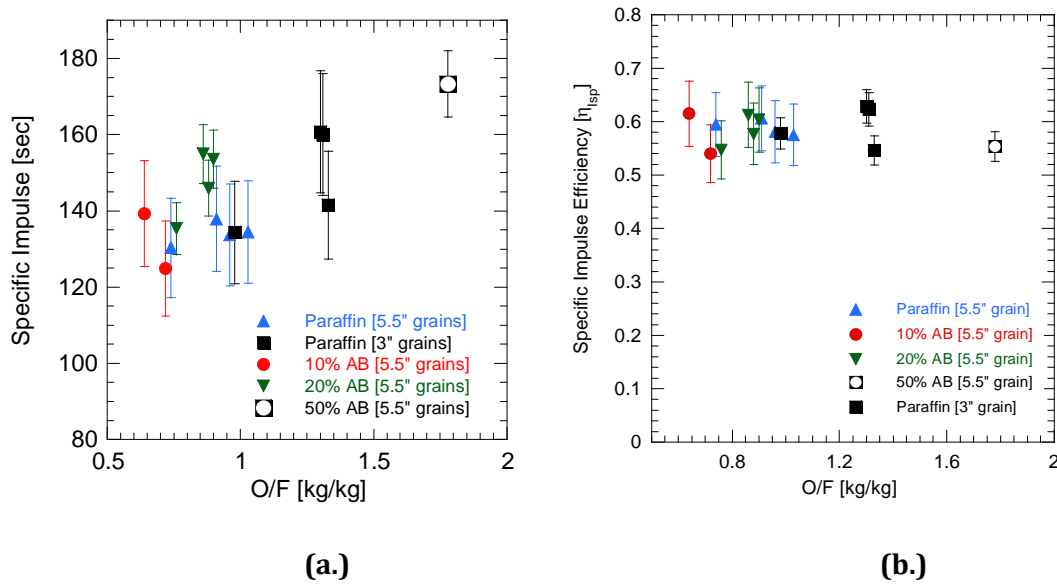
Figure 86: (a.) Specific impulse and (b.) specific impulse efficiency versus O/F ratio for AB/paraffin solid fuel and gaseous oxygen.

In summary, the LSHR study provides further evidence that a substantial addition of AB into the propellant may reduce regression rates and thrust, but the data shows an increase in the characteristic velocity (C*) and specific impulse (I_{sp}) with higher quantities of AB. This is likely due to a rise in chamber temperature with the addition of AB, along with a reduction in the molecular weight of the products from increased quantities of hydrogen in the products of combustion. This data suggests that AB may be good additive for space propulsion, where I_{sp} is much more important than thrust.

Conclusions

ALICE propellants were successfully manufactured and tested in the strand burner and motor configurations. Propellant grains were burned in end-burner and center-perforated grain configurations. Because of the difficulty of ignition and the slow burning rates at low pressures of ALICE mixtures, elevated pressures are preferred for improved combustion. The short burn times of the current center-perforated motors lead to only a short duration of high pressure combustion. Consequently, efficiencies are compromised. Better combustion may be attainable by running at higher equivalence ratios than the current value of 0.71, by operating at high pressures, or by introducing other more energetic additives such hydrogen peroxide.

A bimodal Al particle distribution consisting of nanometer and micron particles was studied in the reaction of aluminum with ice. Addition of micron aluminum to a nanometer based propellant indicated a slight increase in burning rate and then a decrease in burning rate as the fraction of micron aluminum in the particle mixture was increased. Motor performance was not hindered by the present of the micron aluminum. Mixtures with equivalence ratios closer to stoichiometric than fuel lean indicated substantial improvements in the C* and Isp efficiencies. The higher temperatures of the near stoichiometric mixtures enable the formation of molten alumina thus improving the reactivity of the nanometer and micron aluminum.

The combustion of Al/alane/ice reactive mixtures was characterized over a range of pressures and compositions. Thermo-chemical results showed that small quantities of alane added to the baseline formulation can increase the specific impulse by ∼ 10%, while reducing flame temperatures by ∼ 5%. Furthermore, the presence of alane produces more hydrogen in the products, reducing the alumina mole fraction. The linear burning rate and chemical efficiency were relatively unaffected by the substitution of 20-µm Al particles under constant pressure conditions. The burning rate decreased with increasing alane addition, due to reduced adiabatic reaction temperature, although the chemical efficiency remains nearly constant. The linear burning rates for all formulations considered increased with increasing pressure, and were correlated well using a power law. The pressure exponents for the baseline and 80-nm Al/ alane cases were shown to be similar (ranging from 0.405 to 0.477), while the pre-exponential factor decreases from 0.992 to 0.429 with increasing additive weight percentage. The chemical efficiency increased with increasing pressure from approximately 32%, reaching a plateau around 80%. Compositions with 80-nm and 20-µm Al particles had similar pre-exponential values which were slightly lower than the value of the baseline case (decreasing from 0.992 to 0.82), and pressure exponents increased from 0.405 to 0.504. The chemical efficiency increased with increasing pressure from 72% to approximately 80%, and followed the same trend as the baseline composition.

A multi-zone theoretical framework was established to predict the linear burning rates and flame thickness of mono-dispersed and bimodal Alane/Al-water/ice mixtures. The framework was applied to study the combustion of nAl-liquid water mixtures and to investigate the effect of replacing a portion of nAl particles with micron-sized alane and Al particles in nAl-ice mixtures. The major conclusions from the model were:

- At a pressure of 3.65 MPa and for a particle size of 38 nm, the flame speed of nAl-liquid water mixture increased by a factor of 6, as the equivalence ratio increases from 0.5 to 1. The calculated flame speeds exceeded the flame speeds of several energetic propellants such as ADN, HMX, etc.

- The calculated pressure exponent of 0.7 was in reasonably good agreement with the experimentally measured value of ~ 0.5. The combustion of nAl particles in liquid water was controlled by the collisions of water molecules on the particle surface.

- The burning rates of nAl-liquid water mixtures approximately followed a $d^{-1.0}$ – law in the size range of 38-80 nm. The burning rates decreased substantially with increase in the particle size.

- The flame temperatures of Alane-Al-ice mixtures were close to 2300K, which was lower than those of Al-ice mixtures. The lower flame temperatures were attributed to the endothermic dehydrogenation reaction of alane particles prior to their ignition. The flame temperatures increased when a portion of nAl was replaced with µAl particles. This is due to the decrease in the mass fraction of the oxide in the particle.

- Flame thickness on the order of 0.1 mm was predicted for all the mixtures. The flame thickness decreased with an increase in pressure. The dominant combustion mechanism was the collision of water molecules on the nAl particle surface. The flame thickness of µAl reaction zone was not significantly affected by pressure.

- The linear burning rates of Alane-Al-ice mixtures were the lower than those of other mixtures. This was due to the lower flame temperatures and longer burning times of micron-sized alane particles.

- The longer burning times of µAl particles were responsible for the lower burning rates of bimodal Al-ice mixtures, when compared with mono-dispersed Al-ice mixtures. Since, the flame temperatures of bimodal Al-ice mixtures were higher than those of Alane-Al-ice mixtures, higher burning rates were predicted.

The ALICE propellant has shown promise as a rocket propellant in static test firings and with the demonstration flight of a sounding rocket to 1,300 ft. However, much work remains to make it a viable propellant. The success of the test firings and of the launch relied in part in the accurate accounting of the ALICE grain internal ballistic using a versatile lumped-parameter model. With the simplest version of the model, basic propellant properties, grain geometries, and mass conservation equations lead to pressure and thrust predictions. The second version of the model includes the performance of the igniter in order to predict igniter burn out time and give a more accurate burning history. Additionally, both *c** and *Isp* efficiencies can be applied to this model providing a means to match experimental data.

Thermal property measurements of aluminum and ice mixtures indicate thermal conductivity values that are an order of magnitude lower than estimated via a weighted average calculation. Further study is warranted and will benefit the modeling of burning behavior of ALICE and the ignition process.

Mixing of 60 wt. % metal hydride slurries was performed and the resulting mixtures were subjected to a series of reactivity tests. Experience from mixing suggests that additional means of dispersion will be necessary to alleviate slurry settling. Possible solutions to this include use of

higher density carrier fluids, decreasing particle size, and further investigating surfactant-aided dispersion. Additionally, reactivity tests show all RP-1 based slurries can be ignited with hydrogen peroxide and that all slurries bubble when mixed with hot water. Both slurries containing $NaBH_4$ appeared far more reactive in either water or hydrogen peroxide than the others tested.

References

1. Sutton, G. P. and Biblarz, O., "Rocket Propulsion Elements", A Wiley-Interscience Pub., NY, 2001.
2. Palaszewski, B., Ianovski, L. S., and Carrick, P., "Propellant Technologies: Far-Reaching Benefits for Aeronautical and Space-Vehicle Propulsion", J. of Propulsion and Power, Vol.14, No. 5, 1998, pp 641, 648.
3. Reed, B. D., "On-board Chemical Propulsion Technology," in In-Space Propulsion, The 10th International Workshop on Combustion and Propulsion, Italy, Sept. 2003.
4. Greiner, L., Selection of High Performing Propellants for torpedoes. American Rocket Society Journal, 1960. 30: p. 1161-1163.
5. Greiner, L., Under Water Missile Propulsion. 1962: Compas Publications Inc.
6. Ivanov, V., et al., Specific features of the reaction between ultrafine aluminum and water in a combustion regime. Combustion, Explosion, and Shock Waves, 2000. 36(2): p. 213.
7. Foote, J.P., et al., Investigation of Aluminum Particle Combustion for Underwater Applications. AIAA Paper No. 1996-2086, 1996.
8. Ingenito, A. and C. Bruno, Using Aluminum for Space Propulsion. 2004.
9. Risha, G.A., et al., Combustion of Aluminum Particles with Steam and Liquid Water. AIAA, Paper No. 2006-1154, 2006.
10. Risha, G.A., et al., Combustion of nano-aluminum and liquid water. Proceedings of the Combustion Institute, 2007. 31: p. 2029-2036.
11. Miller, T.F. and J.D. Herr, Green Rocket Propulsion by Reaction of Al and Mg Powders and Water, in 40th AIAA Joint Propulsion Conference. 2004, AIAA/ASME/SAE/ASEE: Ft. Lauderdale, FL.
12. Sabourin, J.L., et al., Combustion characteristics of nanoaluminum, liquid water, and hydrogen peroxide mixtures. Combustion and Flame, 2008. 154(3): p. 587-600.
13. Risha, G.A., et al., Aluminum-ICE (ALICE) Propellants for Hydrogen Generation and Propulsion, in 45th AIAA/ASME/SAE/ASEE Joint Propulsion Conference. 2009: Denver, CO.
14. Adirim, H., et al., Advanced ELV Propulsion Solutions: Cryogenic Solid Propellants. 39th AIAA/ASME/SAE/ASEE Joint Propulsion Conference and Exhibit, Huntsville, AL, AIAA Paper No. 2003-5209, 2003.
15. Lo, R.E., H. Adirim, and S. Poller, Cryogenic Solid Propulsion Technology Development Status. 40th AIAA/ASME/SAE/ASEE Joint Propulsion Conference and Exhibit, Fort Lauderdale, FL, AIAA Paper No. 2004-3477, 2004.
16. Adirim, H., et al., Cryogenic Solid Propulsion Technology Development Status. 41st AIAA/ASME/SAE/ASEE Joint Propulsion Conference and Exhibit, Tuscon, AZ, AIAA Paper No. 2005-4093, 2005.
17. Adirim, H., et al., State-of-the-Art in Solid Propellant Research. 42nd AIAA/ASME/SAE/ASEE Joint Propulsion Conference and Exhibit, Sacramento, CA, AIAA Paper No. 2006-4420, 2006.
18. Ivanov, V., et al., Combustion of Electroexploded Aluminum in Liquid Medium. JANNAF Propulsion Meeting, Tampa, Fl., 1995.
19. Lee, W.M., Aluminum Powder-Water Reaction Ignited by Electrical Pulsed Power, N.S.W. Center, Editor. 1993.
20. Kravchenko, K.N., et al., Journal of Alloys and Compounds, 2005. 397: p. 58-62.

21. Lee, J.G., et al., Ammonia Borane Based-Propellants. 44th AIAA/ASME/SAE/ASEE Joint Propulsion Conference and Exhibit, Paper No. 2008-5037, 2008.

22. Franson, C., et al. New high energetic composite propellants for space applications: Refrigerated Solid Propellant (RSP). in 2nd European Conference for Aerospace Sciences (EUCASS), Brussels, Belgium. 2007.

23. Franson, C., et al., Al/H2O and Al/H2O/H2O2 Frozen Mixtures as Examples of New Composite Propellants for Space Applications. 7th International Symposium on Launcher Technologies, Barcelona, Spain, 2007.

24. Yetter, R.A., G.A. Risha, and S.F. Son, Metal particle combustion and nanotechnology. Proceedings of the Combustion Institute, 2009. 32: p. 1819-1838.

25. Wood, T.D., Feasibility Study and Demonstration of an Aluminum and Ice Solid Propellant, in Mechanical Engineering. 2010, Purdue University: West Lafayette, IN.

26. Sundaram, D.S., et al., Flame Propagation of Nanoaluminum-Water Mixtures, in 47th AIAA Aerospace Sciences Meeting. 2009: Orlando, FL.

27. Risha, G.A., et al., Combustion and Conversion Efficiency of Nanoaluminum-Water Mixtures. Combustion Science and Technology, 2008. 180(12): p. 2127-2142.

28. Malchi, J.Y. 2007, The Pennsylvania State University.

29. Sippel, T.R., Characterization of Nanoscale Aluminum and Ice Solid Propellants, in School of Mechanical Engineering. 2009, Purdue University: West Lafayette, IN. p. 173.

30. Sutton, G.P., Biblarz, O., Rocket Propulsion Elements. 8th ed. 2010: John Wiley and Sons Inc. 768.

31. Mcbride, B.J. and S. Gordon, Computer Program for Calculation of Complex Chemical Equilibrium Compositions and Applications. 1996, NASA.

32. Diwan, M., D. Hanna, and A. Varma, Method to release hydrogen from ammonia borane for portable fuel cell applications. International Journal of Hydrogen Energy, 2010. 35(2): p. 577-584.

33. Graetz, J. and J.J. Reilly, Journal of Physical Chemistry, 2005. 109(47): p. 22181-22185.

34. Graetz, J. and J.J. Reilly, Journal of Alloys and Compounds, 2006. 424(1-2): p. 262-265.

35. Graetz, J., et al., Kinetics and thermodynamics of the aluminum hydride polymorphs. Journal of Alloys and Compounds, 2007. 446-447: p. 271.

36. Sandrock, G., et al., Applied Physics a-Materials Science & Processing, 2005. 80(4): p. 687-690.

37. Ojwang, J.G.O., et al., Journal of Chemical Physics, 2009. 131: p. 044501 (1-13).

38. Weiser, V., et al., On the Oxidation and Combustion of AlH_3 a Potential Fuel for Rocket Propellants and Gas Generators. Propellants, Explosives, Pyrotechnics, 2007. 32(3): p. 213.

39. DeLuca, L.T., et al., Physical and ballistic characterization of AlH_3-based space propellants. Aerospace Science and Technology, 2007. 11(1): p. 18.

40. Young, G., et al., International Journal of Energetic Materials and Chemical Propulsion, 2010.

41. Brower, F.M., et al., Journal of American Chemical Society, 1976. 98(9): p. 2450-2453.

42. Petrie, M.A., et al., Preparation of Aluminum Hydride Polymorphs, Particularly Stabilized α-AlH3. 2001: USA.

43. Young, G., et al., Ignition Behavior of AlH_3. Combustion Science and Technology. 182(9): p. 1341 - 1359.

44. Bazyn, T., et al., Combustion Characteristics of Aluminum Hydride at Elevated Pressure and Temperature. Journal of Propulsion and Power, 2004. 20(3): p. 427-431.

45. Connell, T.L., et al. Combustion of Bimodal Al and Ice Mixtures. in 8th International Symposium on Special Topics in Chemical Propulsion. 2009. Cape Town, South Africa.

46. Bruno, C., Ingenito, A., Cuoco, F., "Using Powdered Aluminum for Space Propulsion," *Proceedings of the 18th International Workshop on Rocket Propulsion: Present and Future*, Pozzuoli, 16-20 June 2002.

47. Foote, J.P., Thompson, B.R., Lineberry, J.T., *Advances in Chemical Propulsion*, CRC Press, Florida, 2002.

48. Miller, T.F., Herr, J.D., "Green Rocket Propulsion by Reaction of Al and Mg Powders and Water," *40th AIAA/ASME/SAE/ASEE Joint Propulsion Conference and Exhibit*, Fort Lauderdale, Florida, 2004.

49. Shafirovich, E., Diakov, V., Varma, A., "Combustion of Novel Mixtures for Hydrogen Generation," *Combust. Flame*, Vol. 144, 2006, pp. 415-418.

50. Pickett, F., Booth, D., JANNAF Propulsion and Joint Subcommittees Meeting, Tampa, Florida, 1995.

51. Parr, T., Johnson, C., Hanson-Parr, D., Higa, K., Wilson, K., "Evaluation of Advanced Fuels for Underwater Propulsion," 39th JANNAF Combustion Subcommittee, Colorado Springs, Colorado, USA, 2003.

52. Risha, G.A., Son, S.F., Yetter, R.A., Yang, V., Tappan, B.C., "Combustion of Nano-Aluminum and Liquid Water," *Proc. Combust. Inst.,* Vol. 31, 2007, pp. 2029-2036.

53. Sippel, T.R., Son, S.F., Risha, G.A., Yetter, R.A., "Combustion and Characterization of Nanoscale Aluminum and Ice Propellants," *44th IAA/ASME/SAE /ASEE Joint Propulsion Conference and Exhibit*, Hartford, Connecticut, 2008.

54. Sabourin, J.L., Risha, G.A., Yetter, R.A., Son, S.F., Tappan, B.C., "Combustion Characteristics of Nanoaluminum, Liquid Water, and Hydrogen Peroxide Mixtures," *Combust. Flame*, Vol. 154, No. 3, 2008, pp. 587-600.

55. Risha, G.A., Connell, T.L., Yetter, R.A., Yang, V., Wood, T.D., Pfeil, M.A., Pourpoint, T.L., Son, S.F., "Aluminum-Ice Propellants for Hydrogen Generation and Propulsion," 45th *AIAA/ASME/SAE/ASEE Joint Propulsion Conference and Exhibit*, Denver, CO, 2009.

56. Graetz, J., Reilly, J.J., "Decomposition Kinetics of the AlH_3 Polymoprhs," *J. Phys. Chem. B*, Vol. 109, No.47, 2005, pp. 22181-22185.

57. Bazyn, T., Eyer, R., Krier, H., Glumac, N., "Combustion Characteristics of Aluminum Hydride at Elevated Pressure and Temperature," *J. Prop. Power*, Vol. 20, No. 3, 2004, pp. 427-431.

58. Connell, T.L., Risha, G.A., Yetter, R.A., Yang, V., Son, S.F., *International Journal of Energetic Materials and Chemical Propulsion*, Submitted.

59. Huang, Y., Risha, G.A., Yang, V., Yetter, R.A., "Effect of Particle Size on Combustion of Aluminum Particle Dust in Air," *Combust. Flame*, Vol. 156, 2009, pp.5-13.

60. Bazyn, T., Krier, H., Glumac, N., Shankar N., Wang X., Jackson, T.L., "Decomposition of Aluminum Hydride Under Solid Rocket Motor Conditions," *J. Prop. Power*, Vol. 23, No. 2, 2007, pp. 457-464.

61. Sinke, G. C., Walker, L. C., Oetting, F. L., Stull, D. R., "Thermodynamic Properties of Aluminum Hydride," *J. Chem. Phys.*, Vol. 47, No. 8, 1967, pp. 2759–2761

62. Press, W.H., Teukolsky, S.A., Vetterling, W.T., Flannery, B.P., Numerical Recipes in Fortan 77: The Art of Scientific Computing, Cambridge University Press, 1992.

63. Huang, Y., Risha, G.A., Yang, V., Yetter, R.A., "Combustion of Bimodal Nano/Micro-Sized Aluminum Particle Dust in Air," *Proc. Combust. Inst.*, Vol. 31, 2007, pp.2001-2009.

64. Bazyn, T., Krier, H., Glumac, N., "Combustion of Nanoaluminum Elevated Pressure and Temperature Behind Reflected Shock Waves," *Combust. Flame*, Vol. 145, No. 4, 2006, pp. 703-713.

65. Beckstead, M.W., "A Summary of Aluminum Combustion," RTO/VKI Special Course on Internal Aerodynamics in Solid Rocket Propulsion, Belgium, 2002, pp.1-45.

66. Ingenito, A. and Bruno, C., "Using aluminum for space propulsion," *Journal of Propulsion and Power* Vol. 20, No. 6, 2004, pp. 1056-1063.

67. Shafirovich, E., Bocanegra, P. E., Chauveau, C., Gokalp, I., "Nanoaluminum – Water Slurry: A Novel "Green" Propellant for Space Applications," *Proceedings of the 2nd International Conference on Green Propellants for Space Propulsion*, Vol. 2, 2004.

68. Miller, T. F., Herr, J. D., "Green Rocket Propulsion by Reaction of Al and Mg Powders and Water," *40th Annual AIAA JPC Conference*, Vol. 40, 2004.

69. Sippel, T. R., Son, S. F., Risha, G. A., Yetter, R. A., "Combustion and Characterization of Nanoscael Aluminum and Ice Propellants," *44th Annual AIAA JPC Conference*, Vol. 44, 2008.

70. Showstack, R., "Water on the Moon Confirmed," *Eos Transactions*, AGU, 90 (47), 2009.

71. Linne, D. L., Meyer, M. L.,"A compilation of lunar and Mars exploration strategies utilizing indigenous propellants," NASA TM 105262, 1992.

72. Humble, R. W., Henry, G. N., Larson, W. J., Space Propulsion Analysis and Design, 1st ed., McGraw-Hill, New York, 1995, Chaps. 6.

73. Gordon, S., and McBride, B. J., "Computer Program for Calculation of Complex Chemical Equilibrium Compositions and Applications, Part II. Users Manual and Program Description," NASA Ref. Pub. 1311, June 1996.

74. Yetter, R. A., Risha, G.A., Connell, T, Yang, V., Son, S. F., Sippel, T. S., Pourpoint, T. L., "Novel Energetic Materials for Space Propulsion," Presentation, AFOSR/NASA Office of Chief Engineer Joint Contractors / strategic Planning Meeting in Chemical Propulsion, Vienna VA, 2008.

75. Wood, T. D., "Feasibility Study And Demonstration Of An Aluminum And Ice Solid Propellant," Master's Thesis, Purdue University, 2010.

76. ThrustCurve Hobby Rocket Motor Data, http://www.thrustcurve.org/, Online – February 2011

77. Hot Disk, http://www.hotdisk.se/, Online – February 2011

78. Flueckiger, S., Voskuilen, T., Pourpoint, T., Fisher, T., Zheng, Y., "In Situ Characterization of Metal Hydride Thermal Transport Properties," Int. J. of Hydrogen Energy, Vol. 35, no. 2, pp. 614-621, 2010.

79. Bazyn, T., Eyer, R., Krier, H., Glumac, N., "Dehydrogenation and Burning of Aluminum Hydride at Elevated Pressures," 42nd AIAA Aerospace Sciences Meeting, Reno, NV, 2004, AIAA-2004-789.

80. Bazyn, T., Eyer, R., Krier, H., Glumac, N., "Combustion Characteristics of Aluminum Hydride at Elevated Pressure and Temperature," Journal of Propulsion and Power, Vol. 20, no. 3, pp. 427-431, 2004.

81. Bazyn, T., Eyer, R., Krier, H., Glumac, N., Shankar, N., Wang, X., Jackson, T. L., "Decomposition of Aluminum Hydride under Solid Rocket Motor Conditions," Journal of Propulsion and Power, Vol. 23, no. 2, pp. 457-464, 2007.

82. Glumac, N., Krier, H., Bazyn, T., Eyer, R., "The Combustion Characteristics of Aluminum Hydride under Solid Rocket Motor Conditions," Proceedings of the 9-IWCP, Grafiche GSS, Bergamo, Italy, 2004.

83. McClaine, A. W., "Chemical Hydride Slurry for Hydrogen Production and Storage," Report No. DE-FC36-04GO14011, U.S. Department of Energy, 2008.

84. A. Zuttel, Naturwissenschaften 91 (2004) 157-172.

85. A. Ulas; K. K. Kuo; C. Gotzmer, Combust. Flame 127 (1-2) (2001) 1935-1957.

86. C. F. Lane, "Ammonia Borane and Related N-B-H Compounds and Materials: Safety Aspects, Properties, and Applications, A survey completed as part of a project for the DOE Chemical Hydrogen Storage Center of Excellence," Contract #DEFC36-05GO15060. (2006).

87. S. G. Shore; R. W. Parry, Journal of the American Chemical Society 80 (1) (1958) 8-12.

88. S. G. Shore; R. W. Parry, Journal of the American Chemical Society 77 (22) (1955) 6084-6085.

89. L. E. Fried; K. R. Glaesemann; W. M. Howard; P. C. Souers; P. A. Vitello, in: 4.0 ed.; Lawrence Livermore National Laboratory: Livermore, C.A., 2004.

90. M. L. Hobbs; M. R. Baer; B. C. McGee, Propellants, Explosives, and Pyrotechnics 25 (5) (1999) 269-279.

91. ICP Database, 2001.

92. D. A. Dixon; M. Gutowski, J. Phys. Chem. A 109 (23) (2005) 5129-5135.

93. S. Gordon; B. J. McBride, NASA reference publication 1311 (1994).

94. M. R. Weismiller; A. C. T. van Duin; J. Lee; R. A. Yetter, J. Phys. Chem. A 114 (2010) 5485-5492.

95. M. T. Nguyen; V. S. Nguyen; M. H. Matus; G. Gopakumar; D. A. Dixon, Journal of Physical Chemistry A 111 (4) (2007) 679-690.

96. G. Wolf; J. Baumann; F. Baitalow; F. P. Hoffmann, Thermochimica Acta 343 (1-2) (2000) 19-25.

97. M. G. Hu; R. A. Geanangel; W. W. Wendlandt, Thermochimica Acta 23 (2) (1978) 249-255.

98. F. Baitalow; J. Baumann; G. Wolf; K. Jaenicke-RoÌÎ²ler; G. Leitner, Thermochimica Acta 391 (2002) 159.

99. J. Baumann; E. Baitalow; G. Wolf, Thermochimica Acta 430 (1-2) (2005) 9-14 10.1016/j.tca.2004.12.002.

100. Y. Oyumi; T. B. Brill, Combust. Flame 62 (3) (1985) 213.

101. E. S. Kim; H. S. Lee; C. F. Mallery; S. T. Thynell, Combust. Flame 110 (1-2) (1997) 239.

102. C. K. Law, Progress in Energy and Combustion Science 8 (3) (1982) 171.

103. T. L. Connell; S. A. Santi; G. A. Risha; B. A. Muller; T. D. Batzel, 45th AIAA/ASME/SAE/ASEE Joint Propulsion Conference & Exhibit (2009) AIAA 2009-5086.

104. B. Evans; N. Favorito; E. Boyer; G. A. Risha; R. B. Wehrman; K. K. Kuo, AIAA Paper 3821 (2004) 40.

105. G. A. Risha. Enhancement of Hybrid Rocket Combustion Performance Using Nano-sized Energetic Particles. PhD Dissertaion, Pennsylvania State University, University Park, PA, 2003.